THE UNIVERSITY OF CHICAGO

SINGLE-SHOT READOUT OF THE NEUTRAL DIVACANCY IN SILICON CARBIDE FOR QUANTUM NETWORKS

A DISSERTATION SUBMITTED TO

THE FACULTY OF THE PRITZKER SCHOOL OF MOLECULAR ENGINEERING

IN CANDIDACY FOR THE DEGREE OF

DOCTOR OF PHILOSOPHY

BY

ELENA OKUSHI GLEN

CHICAGO, ILLINOIS

DECEMBER 2022

For my parents.

Table of Contents

List of Figures

List of Tables

This thesis represents the motivations, results, and conclusions from the following works:

[1] *Five-second coherence of a single spin with single-shot readout in silicon carbide.* Christopher P. Anderson*, **Elena O. Glen***, Cyrus Zeledon, Alexandre Bourassa, Yu Jin, Yizhi Zhu, Christian Vorwerk, Alexander L. Crook, Hiroshi Abe, Jawad Ul-Hassan, Takeshi Ohshima, Nguyen T. Son, Giulia Galli, David D. Awschalom, *Science Advances* **8**, 5 (2021)

* These authors contributed equally.

Acknowledgments

There are many people who make a PhD happen.

First and foremost, I would like to thank my advisor, Prof. David Awschalom. David's forward thinking has led to many local and national quantum science initiatives that push the field forward not only from a research perspective, but that put commercialization, infrastructure and policy at the forefront of discussions around quantum information. I believe these conversations are critical, even when some may argue that we don't have fully functional quantum devices yet. In addition to David's optimism and forward thinking, David has a unique ability to bring together people who are not only great scientists, but great people. I am convinced that David's "no jerks" policy towards hiring has been the basis of our research group's many successes. David is also wildly supportive and has helped me to advocate for myself in numerous personal and professional settings, all while maintaining humor, grace, and warmth. I feel incredibly lucky that David gave me a research position on blind faith, back when I was a very clueless undergrad who knocked on his door to inquire about what quantum science even was. I want to embody these great qualities as I move forward in my own career.

Next, I would like to thank my committee members, Prof. Giulia Galli and Prof. Hannes Bernien. Giulia is a world leader in the field of density functional theory, and is a strong yet warm figure who I look up to. Hannes's work with the NV center in diamond was often the inspiration for many of the divacancy experiments that I helped with, and it has been a pleasure to interact with him through the years. I feel that I am in the presence of greatness

at the PME!

In terms of my personal growth in the lab, there is nobody I can thank more than Dr. Chris Anderson. Chris was the first person to take me under his wing when I joined the Awschalom group as an undergraduate researcher in 2016. At first I thought Chris was a professor due to his charisma, confidence, and ease with which he navigated the lab. Even then, as a third year graduate student, people really looked up to him. It seems I never really left his side because we ended up publishing a paper which ultimately became the work that composes this thesis. Chris is a true evangelist for the silicon carbide platform, and has trained me well. I will never forget developing jank align with the Raith, late nights in LL223 singing the same songs by Empire of the Sun while building Ditto, and all those lunch trips to the Med during summer 2020 (fresh mozz and lonch iced caff forever). Thanks for all the rides home, too. There were many times that I thought I would never make it out of graduate school, but I attribute much of my success to Chris's kindness and faith in me. Chris, we did it!

I am grateful for the companionship and support of numerous other students in the lab. Dr. Alex Crook's sense of humor is unparalleled and I still quote Crook-isms to this day. Crook's self-deprecating jokes stand in stark contrast to his extreme diligence, tenacity, and wild competence. I will never forget the day Crook finally achieved photo-electro-chemical etching of silicon carbide, because he looked so happy and victorious. I will also never forget sitting on the floor of the Raith room in our cleanroom suits, cracking jokes and hoping nobody would walk in and find us slacking off. I wish him the best!

Dr. Alex Bourassa is another older student whose great impression has only grown since he graduated. Alex is a gifted programmer, pragmatist, and one of the nicest people ever. Alex laid a lot of the extremely important ground work to establish the silicon carbide platform in our group. Alex, sorry for making you cool down the Montana because I was an upset second year who just wanted to get her hands dirty in the lab. But also, thank you for all your python tutorials, even after you graduated and started working at a "real job."

I hope to see you in Santa Barbara so we can go bouldering together sometime soon!

Peter Mintun served as a great inspiration to me because of his curiosity and drive to explore areas that are unconventional for one on the path of a physics degree. Peter's mentorship both at the PME and at ARCH Venture Partners has been a true gift and has opened my eyes to just what one can do with a scientific background outside of the lab. Thank you Peter for all those late nights in LL227 blasting rap music, talking pro cycling, and for showing me that there's more than one way to go about your PhD. Your kindness and advice have been career defining.

There are several other older students who have helped me to navigate my graduate career. Dr. Kevin Miao is a diligent, organized, and extremely knowledgeable scientist who I worked with extensively for several months. While our hard work did not yield publishable fruit, the experiments we set out to perform shaped me as a scientist and gave me a sense of competency in the cleanroom that I still wield with great pride. Dr. Berk Kovos is a great presence in the lab with his stories and fun facts, and is one of the most approachable scientists I have ever met. Dr. Paul Jerger was a pleasant presence in the labs, and while I did not work with him much, I appreciate his pragmatic approach to problem-solving, his can-do attitude, and his incredible softball skills.

There are many members of the Awschalom group who I would consider not just fellow researchers but also great friends. Jonathan Karsch, Grant Smith, and Pratiti Deb joined the PME with me in 2017, back when it used to be called the Institute for Molecular Engineering. Through the years, they have all seen me struggle through experiments on some days, and skip down the LL2 hallways on others. I am extremely grateful that they were there struggling and laughing alongside me. Pratiti is not only a passionate scientist, but her love of art, history, politics, and people are all characteristics that I admire greatly. Thanks for making great conversation and having my back. Jonathan's genuine love of physics is impressive, and it gives me faith that there are scientists like him out there. Jonathan is kind and understanding, and I love our shared enthusiasm for the great city of

Chicago. Grant's vast knowledge of physics is somewhat mind-boggling, and his sense of humor and ability to tell great stories has been a great boon to many a lunchtime discussion. I've enjoyed countless belly laughs with him. Thank you all for being wonderful friends.

Cyrus Zeledon's enthusiasm for research is a characteristic I found inspiring, especially during periods when I witnessed my own enthusiasm waning during the depths of my degree. I am grateful for Cyrus's unwavering dedication to silicon carbide projects, and his general optimism. Cyrus is a great researcher who was instrumental in getting single-shot readout to work in silicon carbide. I have great faith in him and I am excited to see what he accomplishes next!

Dr. Leah Weiss has become a great friend, swimming buddy, TV-watching accomplice, and housemate. Dr. Yeghishe Tsaturyan (aka "Qualishe Factorian") is a meticulous scientist, kind soul, and has been a joy to work alongside in LL213, especially because he makes me turn up the volume on my music to an embarrassing level. I want to thank Leah and Yeghishe for their support, especially when things got tough. I feel lucky that I got to know them as individuals outside of a scientific setting. Ben Soloway is a fun and hardworking scientist, and I will miss his great laugh! Jacob Feder has helped me immensely to develop my programming skills, and has been a great companion when it comes to having adventures in Chicago. Dr. Erzsi Vincent is a great speaker, meticulous scientist, and is one of the most tenacious and admirable people I know. Joseph Blanton is an incredibly diligent and kind person and it was a pleasure to share the lab with him. Best wishes also to Swathi Chandrika, Jose Mendes, Marquis McMillan, and Chris Egerstrom. They are on their way to greatness!!!

I would like to thank my friends outside of the Awschalom group, who truly held my hand through the entire endeavor of grad school. I met Dr. Amy Butcher as a junior at Brown University in our Intro. Quantum class and had no idea we would end up spending many more years together in the same graduate program. When I first met Amy, I was immediately drawn to her confidence, sense of humor, love of fun, and ability to listen. At the PME, Amy became renowned as a strong, independent, and realistic scientist. These

are all qualities that I look up to immensely and that I try to embody. Amy, thank you for being there for me even when things got really hard. I will always be so incredible grateful for your friendship. I am proud of us!

Dr. Peter Bennington is another great friend who has always been a joy to chat with, and has a great sense of humor. I appreciate that Peter always had time to listen to whatever was on my mind at the time, and that he always advocated for me. I always felt so empowered!

Outside of the Awschalom group and my parents, Chris Conner has perhaps been the most instrumental individual in the completion of my PhD. From very difficult late nights contemplating whether I should quit the program, to days where I ran around the house jumping up and down and dancing because my experiments started working, Chris has truly seen it all. Despite my highs and lows, Chris has always remained an accepting presence. I am infinitely grateful that, just by chance, I sat across from him at the IME visit weekend many years ago. Thanks for believing in me!

Sophia Weaver is one of the happiest accidents to come into my life. Sophia and I agreed to live together during my first year at the PME, despite knowing nothing about each other, and she has since become one of my best friends and confidants. Thank you for being such a loyal and empathetic individual.

Dr. Marguerite Morton was and still remains a force in my life. I miss her every day.

Finally, I want to thank my parents, Dr. Yoshiko Okushi and Dr. Jack Glen, for their truly infinite support. They have endured countless phone calls home and calmly talked through whatever challenges came my way. I respect them both greatly. My mother is a strong, capable, and artistic individual whose motto "let's have fun!" has become my motto too. My father is a hardworking, curious, and adventurous individual who has always been extremely passionate about my own endeavors and encourages me to try new things. They have passed on to me so many of their values and have given me opportunities and experiences that I feel extremely fortunate to have received. I see the sacrifices they have made for me and have them to thank for everything.

Abstract

Spin-defects in crystal lattices are promising candidates for quantum communication and sensing due to their optical addressability and long spin coherence times. Defect spins in silicon carbide (SiC) boast these properties, with the added advantage of being hosted in a scalable and fabrication-amenable semiconducting platform. Despite these advantages, an outstanding hurdle for SiC-based quantum systems is single-shot readout, a deterministic measurement of the quantum state. In this thesis, I will discuss how we ultimately achieved single-shot readout of single neutral divacancies in SiC via spin-to-charge conversion, whereby the defect's spin state is mapped onto a long-lived charge state. Using this technique, we report over 80% readout fidelity without pre- or post-selection, resulting in a high signal-to-noise ratio that enables us to measure long spin coherence times. Combined with pulsed dynamical decoupling sequences in an isotopically purified host material, we measure a single-spin coherence time greater than 5 seconds, over two orders of magnitude greater than previously reported in this system. The mapping of these coherent spin states onto single charges unlocks both single-shot readout for scalable quantum nodes and opportunities for electrical readout via integration with semiconductor devices.

Chapter 1

Quantum Mechanics

1.1 Quantum bits

1.1.1 Qubits and kets

The most fundamental unit of quantum information is a quantum bit, or qubit. Just as classical bits are represented by either a 0 or a 1, qubits also can be represented by either a $|0\rangle$ or a $|1\rangle$. In quantum information, a line "|" and an angle bracket ">" are placed around any symbol (0, 1, a, b, α, β, etc) to form "kets" that denote the qubit state. The use of bra-ket notation, or Dirac notation, is used pretty much universally in quantum mechanics to describe qubit states. Put simply, a ket ($|a\rangle$) can be thought of as a vector in an N-dimensional *Hilbert* space, which is a fancy mathematical way to define a vector space that can be described by an orthonormal basis. Perhaps the most compelling aspect of qubits is that they can take on any linear combination, or superposition, of states:

$$|\psi\rangle = \alpha\,|0\rangle + \beta\,|1\rangle$$

Here, the ket $|\psi\rangle$ represents the overall qubit state, α and β are complex numbers called "probability amplitudes," and the qubit is in a superposition of the states $|0\rangle$ and $|1\rangle$. A

fundamental aspect of quantum mechanics says that if we were to measure the qubit state $|\psi\rangle$, we would only be able to retrieve the result 0 or 1, with probability $|\alpha|^2$ or $|\beta|^2$, respectively. What we do know is that there is a 100% chance of measuring either 0 or 1, or in other words that $|\alpha|^2 + |\beta|^2 = 1$. This condition that the modulus of the probability amplitudes sum to unity is called normalization. While any state in a 2D vector space may be totally described as a linear combination of the states $|0\rangle$ and $|1\rangle$, any arbitrary ket can be denoted as the combination of states:

$$|\psi\rangle = \sum_i c_i \, |i\rangle$$

Where c_i are complex coefficients that satisfy $\sum_i |c_i|^2 = 1$, and the kets $|i\rangle$ form an orthonormal basis to describe the i-dimensional vector space.

1.1.2 Kets and vector notation

While bra-ket notation is used ubiquitously to denote qubit states, quantum mechanics is fundamentally rooted in linear algebra and an intuitive alternative is to use matrix notation to represent bras and kets. This becomes particularly useful when examining the effects that logical operations have on the qubit state. For a 2D Hilbert space spanned by the orthonormal basis $|0\rangle$ and $|1\rangle$. The state $|\psi\rangle = \alpha \, |0\rangle + \beta \, |1\rangle$ is written in vector notation as:

$$|\psi\rangle = \begin{pmatrix} \alpha \\ \beta \end{pmatrix}$$

There is no limit to the dimensionality of a Hilbert space. Thus a qubit in an N-dimensional Hilbert space, described with Dirac notation as $|\psi\rangle = \sum_{i=1}^{N} c_i \, |i\rangle$, is described using an $N \times 1$ vector:

$$|\psi\rangle = \begin{pmatrix} c_1 \\ c_2 \\ \vdots \\ c_N \end{pmatrix}$$

1.1.3 Bra space, inner products, and orthonormality

A fundamental aspect of any Hilbert space is the *inner product*. The inner product is the generalization of a dot product between two vectors, and can be thought of as the overlap of one state onto another. In Dirac notation, this overlapping is represented by the action of a "bra" on a ket, where bras are represented with a reversed angle bracket "<" and a line "|" placed around a symbol (0, 1, a, b, α, β, etc). The inner product between the ket $|a\rangle$ and the bra $\langle b|$ is written $\langle b|a\rangle$. Crucially, for any given ket $|\psi\rangle = \sum_i c_i |i\rangle$:

- The bra of $|\psi\rangle$ is written $\langle\psi| = \sum_i c_i^* \langle i|$ where c_i^* is the complex conjugate of c_i. In other words, the bra is the conjugate transpose of the ket: $\langle\psi| = |\psi\rangle^\dagger$
- The inner product of $\langle\phi|$ and $|\psi\rangle$ is such that $\langle\phi|\psi\rangle = \langle\psi|\phi\rangle^*$
- Two kets are said to be orthogonal if $\langle\phi|\psi\rangle = \langle\psi|\phi\rangle^* = 0$
- The inner product of a ket with itself is positive definite such that $\langle\psi|\psi\rangle \geq 0$

Given that any ket in N-dimensional Hilbert space can be written as a $(N \times 1)$ column vector and that the bra is the conjugate transpose of its ket, the bra of $|\psi\rangle$ is written as a $(1 \times N)$ row vector:

$$\langle\psi| = \sum_i^N c_i^* \langle i| = \begin{pmatrix} c_1^*, c_2^* \dots c_N^* \end{pmatrix}$$

Thus the inner product of two states in N-dimensional Hilbert space is found simply by multiplying their vector representations. For example, for $|\phi\rangle = \sum_i^N a_i |i\rangle$ and $|\psi\rangle = \sum_i^N c_i |i\rangle$,

the inner product is:

$$\langle\phi|\psi\rangle = \begin{pmatrix} a_1^*, a_2^* \dots a_N^* \end{pmatrix} \begin{pmatrix} c_1 \\ c_2 \\ \vdots \\ c_N \end{pmatrix} = c_1 a_1^* + c_2 a_2^* + c_3 a_3^* + ... + c_N a_N^*$$

Now that the use of matrix notation for quantum state representation has been established, the effect of multiplying two orthonormal states becomes clear. In the language of linear algebra, orthonormality means two or more states are linearly independent and normalized to be unit length. For example, the states $|0\rangle = \left(\begin{smallmatrix} 1 \\ 0 \end{smallmatrix}\right)$ and $|1\rangle = \left(\begin{smallmatrix} 0 \\ 1 \end{smallmatrix}\right)$ form an orthonormal basis, since they are orthogonal $\langle 0|1\rangle = \left(\begin{smallmatrix} 1,0 \end{smallmatrix}\right)\left(\begin{smallmatrix} 0 \\ 1 \end{smallmatrix}\right) = (1 \times 0) + (0 \times 1) = 0$ and are normalized such that $\langle 0|0\rangle = \left(\begin{smallmatrix} 1,0 \end{smallmatrix}\right)\left(\begin{smallmatrix} 1 \\ 0 \end{smallmatrix}\right) = 1$ and $\langle 1|1\rangle = \left(\begin{smallmatrix} 0,1 \end{smallmatrix}\right)\left(\begin{smallmatrix} 0 \\ 1 \end{smallmatrix}\right) = 1$.

1.1.4 Operators and outer products

We have discussed the inner product, which intuitively can be thought of as the degree of overlap between two quantum states. Now we will discuss the outer product, which is a convenient way to represent linear operators. In quantum mechanics, linear operators describe an action performed on a quantum state. *Observables* such as momentum and spin are operators. Operators act on kets from the left side:

$$X\,|\psi\rangle$$

Operators act on bras from the right side:

$$\langle\psi|\,X$$

Generally, a linear operator acting on a Hilbert space can be expressed as an outer product. The outer product of the bra $\langle\phi|$ and the ket $|\psi\rangle$ forms the operator:

$$\hat{X} = |\psi\rangle\langle\phi|$$

The action of this operator on a state $\left|\psi'\right\rangle$ is:

$$\hat{X}\left|\psi'\right\rangle = (|\psi\rangle\langle\phi|)(\left|\psi'\right\rangle) = |\psi\rangle\left\langle\phi|\psi'\right\rangle = \left\langle\phi|\psi'\right\rangle|\psi\rangle$$

Given the definition of kets as column vectors and bras as row vectors, the outer product of $|\phi\rangle = \sum_i^N a_i|i\rangle$ and $|\psi\rangle = \sum_i^N c_i|i\rangle$ can be written in matrix form:

$$\hat{X} = |\psi\rangle\langle\phi| = |\psi\rangle(|\phi\rangle^\dagger) = \begin{pmatrix} c_1 \\ c_2 \\ \vdots \\ c_N \end{pmatrix}\begin{pmatrix} a_1^*, a_2^*, \dots a_N^* \end{pmatrix} = \begin{pmatrix} a_1^*c_1 & a_2^*c_1 & \dots & a_N^*c_1 \\ a_1^*c_2 & a_2^*c_2 & \dots & a_N^*c_2 \\ \vdots & & & \vdots \\ a_1^*c_N & a_2^*c_N & \dots & a_N^*c_N \end{pmatrix}$$

Hence, any operator acting on an N-dimensional Hilber space can be represented as a $(N \times N)$ matrix. Importantly, quantum operators do not commute ($XY \neq YX$), meaning $XY|\psi\rangle \neq YX|\psi\rangle$. Following from the definition of $|\psi\rangle\langle\phi|$ as the multiplication of the column vector representation of $|\psi\rangle$ times the row vector $\langle\phi|$, the Hermitian adjoint of the operator $\hat{X}$ is:

$$\hat{X}^\dagger = (|\psi\rangle\langle\phi|)^\dagger = |\phi\rangle\langle\psi|$$

1.1.5 Hermitian operators, observables, and measurement

If the Hermitian adjoint of an operator returns the same operator, that operator is said to be Hermitian:

$$\hat{X}^\dagger = \hat{X}$$

Hermitian operators are diagonalizable, meaning that for a Hermitian matrix A, there exists an invertible matrix P such that $P^{-1}AP = D$ where D is a diagonal matrix. Hermitian operators are extremely important in quantum mechanics because they correspond to physically observable quantities such as momentum, position, and spin. In the language of linear algebra, this corresponds to the eigenvalues of a Hermitian operator having real values. The eigenstates of a Hermitian operator $\hat{A}$ satisfy the relation:

$$\hat{A}\,|\alpha\rangle = a\,|\alpha\rangle$$

where a is called an eigenvalue and $|\alpha\rangle$ is called an eigenstate or eigenket of $\hat{A}$. More generally, for any diagonalizable operator $\hat{A}$ with eigenstates $|\alpha_i\rangle$ and eigenenergies a_i [1], the operator can be fully described as a linear combination of its basis states:

$$\hat{A} = \sum_i a_i\,|\alpha_i\rangle\,\langle\alpha_i|$$

Additionally, because $\hat{A}$ is Hermitian, $(\hat{A}\,|\alpha\rangle)^\dagger = (a\,|\alpha\rangle)^\dagger = a^*\,\langle\alpha|$.

Returning to the statement that all physical observables are Hermitian, this means that the eigenvalues a_i of $\hat{A}$ are real-valued. The probabilistic expected value of a measurement is called the expectation value. For an observable $\hat{A}$, the expectation value of that operator acting on the state $|\psi\rangle$ is:

$$\langle A\rangle = \langle\psi|\,\hat{A}\,|\psi\rangle$$

If $\hat{A}$ has eigenvectors $|\alpha_i\rangle$ with eigenvalues a_i, the expectation value is:

$$\langle A\rangle = \langle\psi|\,\hat{A}\,|\psi\rangle = \sum_i a_i a_i^*\,\langle\psi|\alpha_i\rangle\,\langle\alpha_i|\psi\rangle = \sum_i |a_i|^2|\,\langle\alpha_i|\psi\rangle\,|^2$$

1. Diagonalizable matrices must have a full eigenbasis. An $n \times n$ matrix has a full eigenbasis if it has n linearly independent eigenvectors.

Expressed in this way, it becomes clearer that the expectation value is simply the average of the possible outcomes a_i of the measurement, weighted by their relative probabilities $|\langle \alpha_i|\psi\rangle|^2$.

Finally, a crucial aspect of quantum observables is that they cannot be simultaneously known. In linear algebra, this is often referred to as incompatibility or non-commutativity of observables:

$$[\hat{A}, \hat{B}] = \hat{A}\hat{B} - \hat{B}\hat{A} \neq 0$$

The physical intuition behind the non-commutation property is that the result of a measurement will depend on the order in which the observables $\hat{A}, \hat{B}$ are measured. While an unobserved quantum state is in a superposition of eigenstates $|\psi\rangle = \sum_i c_i |\psi_i\rangle$, the act of measuring that state induces an interaction between the state and the outside world. This interaction, or "observation," has the effect of reducing the system to one of its eigenstates $|\psi\rangle \rightarrow |\psi_i\rangle$. This reduction is often referred to as "collapsing the wavefunction," where the probability of measuring a particular eigenstate $|\psi_i\rangle$ of the wavefunction is $|c_i|^2$.

1.1.6 Electron spin and the Bloch sphere

Some examples of qubit systems include the energy levels of trapped atoms and ions, the photon number occupation of a superconducting resonator, or the spin state of a single electron. For a single spin 1/2 electron, the qubit basis states are comprised by the values of the possible spin quantum numbers: $m_s = +\frac{1}{2}$ and $m_s = -\frac{1}{2}$. These two spin states are commonly represented as $|\uparrow\rangle$ and $|\downarrow\rangle$ due to the interpretation of the electron spin as a magnetic dipole pointing up or down. Consider a single electron spin in the state:

$$|\psi\rangle = \frac{1}{\sqrt{2}}|\uparrow\rangle + \frac{1}{\sqrt{2}}|\downarrow\rangle$$

Here the spin qubit is in an equal superposition of $|\uparrow\rangle$ and $|\downarrow\rangle$, where the probability of being in $|\uparrow\rangle$ is $|\frac{1}{\sqrt{2}}|^2 = 0.5$ or 50% and the probability of being in $|\downarrow\rangle$ is also $|\frac{1}{\sqrt{2}}|^2 = 0.5$ or

50%.

Let's hearken back to the idea of Hilbert spaces and introduce the idea of the geometric representation of a qubit. All the states we have discussed up to this point have been pure states, meaning they represent a single quantum state. In contrast, *mixed* states cannot be represented by a superposition of kets and instead are represented using a density matrix. While density matrices are outside the scope of this thesis, a good example of a mixed state may be a set, or "ensemble," of multiple electron spins. Within that ensemble, each single electron spin is described as a pure state. Any two-level pure state can be described as a point on the surface a 3D sphere with unit radius called the Bloch sphere. The Bloch sphere is useful because it allows us to visualize pretty much all relevant aspects of a qubit, such as its coefficients and phase. Consider the state $|0\rangle = |\uparrow\rangle$. This state is often represented as a vector with termination on the North pole of the Bloch sphere (Fig. 1.1).

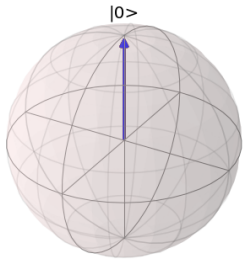

Figure 1.1: The state $|0\rangle$ on the Bloch sphere.

The state $|1\rangle = |\downarrow\rangle$ is represented as a vector with termination on the South pole (Fig. 1.2).

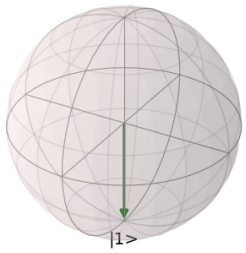

Figure 1.2: The state $|1\rangle$ on the Bloch sphere.

The true power of the Bloch sphere comes when we consider the arbitrary qubit state:

$$|\psi\rangle = cos(\frac{\theta}{2})\,|0\rangle + e^{i\phi}sin(\frac{\theta}{2})\,|1\rangle$$

Using spherical coordinates, this is a vector with termination on the surface of the Bloch

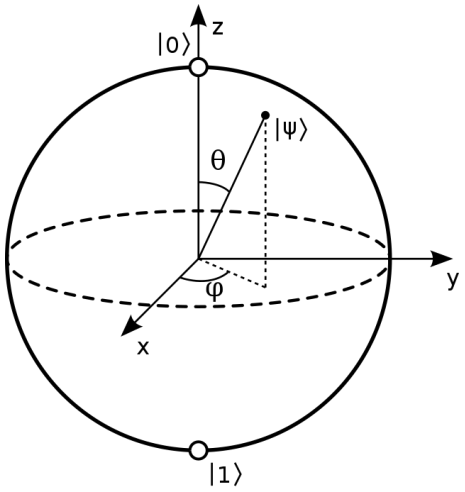

Figure 1.3: Arbitrary state $|\psi\rangle$ on Bloch sphere.

sphere, meaning it has a radial distance of 1, with azimuthal angle θ and polar angle ϕ (Fig. 1.3). Besides the obvious fact that any point on the surface of the Bloch sphere except the North and South poles is a superposition of the basis states $|0\rangle$ and $|1\rangle$, a key point of interest here is the polar angle ϕ which describes the relative phase between $|0\rangle$ and $|1\rangle$.

This is our first encounter with a truly complex coefficient $e^{i\phi} = cos(\phi)+isin(\phi) = a+ib$. The bra of the general qubit state is:

$$\langle\psi| = cos(\frac{\theta}{2})\,\langle 0| + e^{-i\phi}sin(\frac{\theta}{2})\,\langle 1|$$

Upon closer inspection of the Bloch sphere, we see that the equators are labelled with an x and y (Fig. 1.3). Commonly referenced states on the equator in the x-y plane include:

$$|+\rangle = \frac{(|0\rangle + |1\rangle)}{\sqrt{2}}$$

$$|-\rangle = \frac{(|0\rangle - |1\rangle)}{\sqrt{2}}$$

$$|+i\rangle = \frac{(|0\rangle + i\,|1\rangle)}{\sqrt{2}}$$

$$|-i\rangle = \frac{(|0\rangle - i\,|1\rangle)}{\sqrt{2}}$$

Where, for all these states on the equator, the angle $\theta = \frac{\pi}{2}$ and the angle ϕ is equal to 0, π, $\pi/2$ and $3\pi/4$ for $|+\rangle$, $|-\rangle$, $|+i\rangle$ and $|-i\rangle$, respectively (Fig. 1.4).

While this section has dealt with qubits with two basis states, such as the spin projection of a single electron, physical qubit implementations do not inherently need to be two-level systems. For example, the $m_s = 0$ and $m_s = +1$ sublevels may be used as a qubit basis within the larger basis space spanned by the $m_s = 0$, $m_s = +1$ and $m_s = -1$ sublevels of a spin-1 (S=1) system.

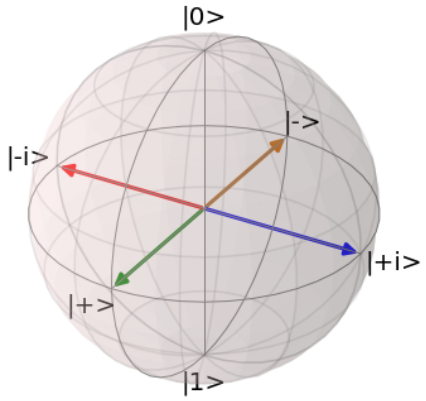

Figure 1.4: The various states on the equator of the Bloch sphere.

1.2 Qubit operations

1.2.1 Single qubit operations

Qubits are not useful or interesting unless they can be manipulated at will to perform logical operations. Single qubit gates are simply operators that rotate a state vector about the

Bloch sphere or impose a global phase on a state on the Bloch sphere. All operations that map a state on the surface of the Bloch sphere to another part of the Bloch sphere are called unitary transformations. Unitary transformations are important because they preserve inner products. All unitary operations, and therefore unitary matrices, follow the relation $U^\dagger U = UU^\dagger = \mathbb{1}$, where $\mathbb{1}$ is the identity. This unitary constraint is pretty much the only requirement or constraint for any valid quantum gate. Any single qubit gate can be described as a combination of rotation about some axis $\hat{n}$ and the accumulation of a global phase α:

$$e^{i\alpha}\hat{R}_{\hat{n}}(\theta)$$

Where the rotation of the qubit state about the axis n by angle θ is defined as:

$$\hat{R}_{\hat{n}}(\theta) = e^{-i\theta(\sigma_{\hat{n}}\cdot\hat{n})/2}$$

The Taylor expansion of an exponential function is written:

$$e^{iAx} = 1 + iAx - \frac{x^2}{2!} - i\frac{x^3}{3!}A + ...$$
$$= (1 - \frac{x^2}{2!} + \frac{x^4}{4!}...) + i(x - \frac{x^3}{3!} + \frac{x^5}{5!}...)A$$

Following from this, in the case where A is the operator $\hat{A}$:

$$e^{i\hat{A}x} = (1 - \frac{x^2}{2!} + \frac{x^4}{4!}...)\mathbb{1} + i(x - \frac{x^3}{3!} + \frac{x^5}{5!}...)\hat{A}$$

The prefactors that multiply $\mathbb{1}$ and $\hat{A}$ are the Taylor expansions of sine and cosine. Therefore the rotation matrix can be written:

$$\hat{R}_{\hat{n}}(\theta) = cos(\frac{\theta}{2})\mathbb{1} - isin(\frac{\theta}{2})(\sigma_n \cdot \hat{n})$$

More specifically:

$$\hat{R}_x(\theta) = e^{-i\theta\sigma_x/2} = cos(\frac{\theta}{2})I - isin(\frac{\theta}{2})\sigma_x = \begin{pmatrix} cos(\frac{\theta}{2}) & -isin(\frac{\theta}{2}) \\ -isin(\frac{\theta}{2}) & cos(\frac{\theta}{2}) \end{pmatrix}$$

$$\hat{R}_y(\theta) = e^{-i\theta\sigma_y/2} = cos(\frac{\theta}{2})I - isin(\frac{\theta}{2})\sigma_y = \begin{pmatrix} cos(\frac{\theta}{2}) & -sin(\frac{\theta}{2}) \\ sin(\frac{\theta}{2}) & cos(\frac{\theta}{2}) \end{pmatrix}$$

$$\hat{R}_z(\theta) = e^{-i\theta\sigma_z/2} = cos(\frac{\theta}{2})I - isin(\frac{\theta}{2})\sigma_z = \begin{pmatrix} e^{-i\theta/2} & 0 \\ 0 & e^{i\theta/2} \end{pmatrix}$$

We here introduce the Z-Y decomposition of single qubit operations:

$$\hat{U} = e^{i\alpha}R_z(\beta)R_y(\gamma)R_z(\delta)$$

Writing this decomposition out in matrix form, it is clear that

$$\hat{U} = e^{i\alpha}\begin{pmatrix} e^{-i\frac{\beta}{2}} & 0 \\ 0 & e^{i\frac{\beta}{2}} \end{pmatrix}\begin{pmatrix} cos(\frac{\gamma}{2}) & -sin(\frac{\gamma}{2}) \\ sin(\frac{\gamma}{2}) & cos(\frac{\gamma}{2}) \end{pmatrix}\begin{pmatrix} e^{-i\frac{\delta}{2}} & 0 \\ 0 & e^{i\frac{\delta}{2}} \end{pmatrix}$$

$$= \begin{pmatrix} e^{i(\alpha-\beta/2-\delta/2)}cos(\gamma/2) & -e^{i(\alpha-\beta/2+\delta/2)}sin(\gamma/2) \\ e^{i(\alpha+\beta/2-\delta/2)}sin(\gamma/2) & e^{i(\alpha+\beta/2+\delta/2)}cos(\gamma/2) \end{pmatrix}$$

The above matrix satisfies $U^\dagger U = UU^\dagger = \mathbb{1}$. Therefore, any unitary single qubit operation can be expressed as the above matrix for the appropriate choice of α, β, γ, and δ.

1.2.2 Multiple qubits

Only single qubit state representations and single qubit operations have been discussed thus far. However, the true power of quantum information is only realized through multi-qubit algorithms and entanglement. This section will discuss multi-qubit state representation and two-qubit gates.

Dirac notation is extended from the single-qubit to a multi-qubit treatment, where multiple symbols can be included within a bra or ket to represent a combined state consisting of multiple logical elements. Mathematically, this is denoted as the tensor product of two single-qubit state representations. For example, the state where two electron spins are both in $|0\rangle$ is expressed as the tensor product $|0\rangle \otimes |0\rangle = |00\rangle$. Here, $\otimes$ symbolizes the tensor product of two vectors that are bilinearly mapped onto the tensor space. In the context of quantum information, it is sufficient to think of the tensor product as the vector space composed of two single-qubit subsystems.

An important attribute of the tensor product is its distributive properties. If one qubit is in $|\psi\rangle = \alpha |a\rangle + \beta |b\rangle$ and another qubit is in $|\phi\rangle = \gamma |c\rangle + \delta |d\rangle$, they have a combined state:

$$|\Phi\rangle = |\psi\rangle \otimes |\phi\rangle = |\psi\rangle |\phi\rangle$$

$$= (\alpha |a\rangle + \beta |b\rangle) \otimes (\gamma |c\rangle + \delta |d\rangle)$$

$$= \alpha\gamma |a\rangle |c\rangle + \alpha\delta |a\rangle |d\rangle + \beta\gamma |b\rangle |c\rangle + \beta\delta |b\rangle |d\rangle$$

$$= \alpha\gamma |ac\rangle + \alpha\delta |ad\rangle + \beta\gamma |bc\rangle + \beta\delta |bd\rangle$$

Here, renormalization is required such that the sum of the squares of the absolute values of the coefficients equals one. The distributive property can be extended to an infinite number of qubits.

The tensor product effectively expands the dimensionality of the vector representation

of our state. Individually, each single electron spin can be described with a 2×1 vector. However, two electron spins are represented by a 4×1 vector. Rewriting $|\psi\rangle = \alpha |0\rangle + \beta |1\rangle$ and $|\phi\rangle = \gamma |0\rangle + \delta |1\rangle$, the tensor product is:

$$|\Phi\rangle = |\phi\rangle \otimes |\psi\rangle = \begin{pmatrix} \alpha\gamma \\ \alpha\delta \\ \beta\gamma \\ \alpha\delta \end{pmatrix}$$

Where the first row represents the probability amplitude of the $|00\rangle$ state, the second row represents the probability amplitude of the $|01\rangle$ state, and so on. Extending this example to a system with m qubits, each with N possible states, the number of complex amplitudes for the combined multi-qubit logical state will be N^m.

1.2.3 Two-qubit gates

While any logical operation can be expressed as a matrix acting on a quantum state, a more careful mathematical treatment of these matrix operators is necessary when expanding the computation space to more than one qubit. Specifically, when two qubits undergo different logical operations in parallel, the combined effect of those parallel gates is the tensor product of their matrix representations. For a two-qubit system, if an operator $\hat{A}$ acts on the first qubit $|\psi_1\rangle$ while an operator $\hat{B}$ acts on the second qubit $|\psi_2\rangle$, the combined effect of $\hat{A}$ and $\hat{B}$ acting in parallel is written:

$$\hat{C} = \hat{A} \otimes \hat{B}$$

This has the effect:

$$\hat{C} |\psi\rangle = \hat{C}(|\psi_1\rangle \otimes |\psi_2\rangle) = (\hat{A} |\psi_1\rangle) \otimes (\hat{B} |\psi_2\rangle)$$

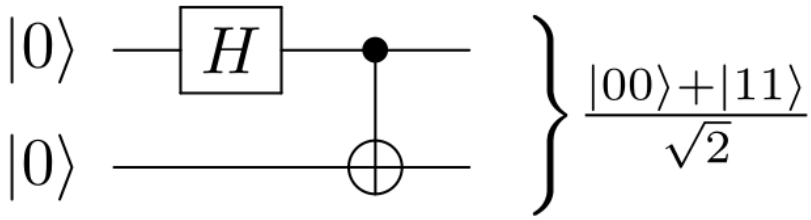

Figure 1.5: Bell state generation. All four of the maximally entangled Bell states can be generated by applying a Hadamard gate to the control qubit, followed by a CNOT gate. For the input state $|00\rangle$, applying these operations generates the entangled state $\frac{|00\rangle+|11\rangle}{\sqrt{2}}$

1.2.4 Entanglement

Arguably the most powerful aspect of quantum information is the use of computational algorithms and communication protocols requiring entangled states. Multi-qubit entangled states cannot be described independently of the state of another qubit. Mathematically, this means entangled states cannot be described as a tensor product of two constituent states. Take, for example, the two qubit state:

$$\left|\Phi^{+}\right\rangle = \frac{|00\rangle + |11\rangle}{\sqrt{2}}$$

This state is an entangled state because there are no decompositions wherein it is possible to express $|\psi\rangle$ as the tensor product $|\psi_1\rangle \otimes |\psi_2\rangle$. The above state is a special type of entangled state called a Bell state, which is the simplest maximally entangled two-qubit state. The other two qubit entangled Bell states are:

$$\left|\Phi^{-}\right\rangle = \frac{|00\rangle - |11\rangle}{\sqrt{2}}$$

$$\left|\Psi^{+}\right\rangle = \frac{|01\rangle + |10\rangle}{\sqrt{2}}$$

$$\left|\Psi^{-}\right\rangle = \frac{|01\rangle - |10\rangle}{\sqrt{2}}$$

Two-qubit Bell state generation is performed through an entangling gate $\hat{E}$ involving

application of a Hadamard gate to the first qubit followed by a CNOT gate where the first qubit acts as the control (Fig. 1.5):

$$\hat{E} = \text{CNOT}(\hat{H} \otimes I)$$
$$= \frac{1}{\sqrt{2}} \begin{pmatrix} 1 & 0 & 0 & 0 \\ 0 & 1 & 0 & 0 \\ 0 & 0 & 0 & 1 \\ 0 & 0 & 1 & 0 \end{pmatrix} \begin{pmatrix} 1 & 0 & 1 & 0 \\ 0 & 1 & 0 & 1 \\ 1 & 0 & -1 & 0 \\ 0 & 1 & 0 & -1 \end{pmatrix}$$

In the case where both qubits are prepared to $|0\rangle$, this has the effect:

$$\hat{E}\,|00\rangle = \frac{1}{\sqrt{2}} \begin{pmatrix} 1 & 0 & 1 & 0 \\ 0 & 1 & 0 & 1 \\ 0 & 1 & 0 & -1 \\ 1 & 0 & -1 & 0 \end{pmatrix} \begin{pmatrix} 1 \\ 0 \\ 0 \\ 0 \end{pmatrix} = \frac{1}{\sqrt{2}} \begin{pmatrix} 1 \\ 0 \\ 0 \\ 1 \end{pmatrix} = \frac{|00\rangle + |11\rangle}{\sqrt{2}}$$

Which is one of the maximally entangled Bell states. The other Bell states can be formed by applying the operator $\hat{E}$ to the input states $|01\rangle, |10\rangle$, and $|11\rangle$.

1.3 Time evolution

Unlike Hermitian observables such as position and momentum that have real eigenvalues, time is not a measurable quantity of a quantum system. To understand the dynamics of a quantum state that undergoes evolution in time, we turn to the Schrödinger equation:

$$i\hbar \frac{d}{dt} |\psi(t)\rangle = \hat{H} |\psi(t)\rangle$$

The solution to this equation undergoes time evolution $\hat{U}(t)$ such that :

$$|\psi(t)\rangle = \hat{U}(t, t_0)\,|\psi(0)\rangle$$

Plugging this into the Schrödinger equation:

$$[i\hbar\frac{d}{dt} - \hat{H}]\hat{U}(t, t_0)\,|\psi(0)\rangle = 0$$

Disregarding the meaningless solution where $|\psi(0)\rangle = 0$:

$$i\hbar\frac{d}{dt}\hat{U}(t, t_0) = \hat{H}\hat{U}(t, t_0)$$

To solve this equation, we first find the Taylor expansion of $\hat{U}(t + \delta t, t)$ evaluated about t:

$$\hat{U}(t + \delta t, t_0) = \hat{U}(t, t_0) + \frac{\partial U(t, t_0)}{\partial t}\delta t + \mathcal{O}(\delta t^2)$$

In the case where $\delta t \to 0$, the higher order terms $\mathcal{O}(\delta t^2)$ are dropped:

$$\hat{U}(t + \delta t, t_0) = \hat{U}(t, t_0) + \frac{\partial U(t, t_0)}{\partial t}\delta t$$

Substituting in the expression from the Schrödinger equation:

$$U(t + \delta t, t_0) = U(t, t_0) - \frac{i}{\hbar}H(t)U(t, t_0) + \mathcal{O}(\delta t^2)$$

We set $t_0 = t$ and use the fact that $\hat{U}(t, t)$ does not incur any time evolution, meaning it has the same effect as the identity operator $\hat{U}(t_0, t_0) = \mathbb{1}$:

$$U(t + \delta t, t) = \mathbb{1} - \frac{i}{\hbar}H(t)\delta t\mathbb{1} + \mathcal{O}(\delta t^2)$$

The first two terms on the right hand side of the equation are the leading terms of the Taylor expansion for an exponential, and the equation is rewritten:

$$U(t+\delta t,t) = e^{-\frac{i}{\hbar}H\delta t} + \mathcal{O}(\delta t^2)$$

Ignoring the higher order terms, the resulting form of the time evolution operator is:

$$\hat{U}(t) = e^{-\frac{i}{\hbar}\hat{H}t}$$

As we will see, the time evolution operator is critical when considering the effects of quantum noise and other couplings, especially in the context of qubit dephasing and relaxation.

1.4 Coherence and relaxation

Quantum coherence is the idea that a unique phase relationship exists between states in a superposition. For example, in the state $|+\rangle = \frac{(|0\rangle+|1\rangle)}{\sqrt{2}}$, there is a phase of 0 between $|0\rangle$ and $|1\rangle$ while $|-i\rangle = \frac{(|0\rangle-i|1\rangle)}{\sqrt{2}}$ has phase $3\pi/2$ between $|0\rangle$ and $|1\rangle$. More generally, given the general expression of some arbitrary state $|\psi\rangle = cos(\frac{\theta}{2})\,|0\rangle + e^{i\phi}sin(\frac{\theta}{2})\,|1\rangle$, the phase relation between $|0\rangle$ and $|1\rangle$ is ϕ. Preservation of the phase is called maintaining the coherence of the state, and the characteristic timescale over which that preservation lasts is called the coherence time. The lack of preservation of ϕ is called decoherence and can be thought of as the precession of a state vector about the z-axis of the Bloch sphere.

What causes decoherence? While we have treated quantum states thus far as isolated systems, in reality quantum systems interact with their environments, resulting in the loss of information. The sources of decoherence for a qubit depend on the qubit system in question, but examples include magnetic noise from nearby nuclear spins, electric noise from nearby charges, cross-talk between qubits, and radiation.

Relaxation is a process where a state reaches an energy equilibrium. Relaxation is an

entirely different process from decoherence. Whereas a state that has totally decohered may still be represented by a vector with termination on the surface of the Bloch sphere, during relaxation a state vector will shrink or "shorten" such that it no longer terminates on the surface. An example of a relaxation process is the net magnetization of nuclear spins along an applied magnetic field in an NMR experiment.

Chapter 2

Defects in Semiconductors

In this section, we will begin discussion of the qubit system I worked with throughout the course of my PhD: the neutral divacancy (VV^0) in silicon carbide (SiC). For the purposes of quantum information, defects with energy levels that are "deep" within the bandgap of a semiconductors are often preferred because they are well-isolated from thermal fluctuations that cause unwanted electron population of the defect levels. Indeed, the energy levels of VV^0 are found deep within the wide bandgap of SiC (E_g=3.26 eV). To better understand semiconductors and their properties, we must first understand energy bands.

2.0.1 Fermi levels, energy bands, and dopants

All crystalline solids have an electronic band structure that describes the energy states that electrons in the solid may occupy. From the Pauli exclusion rule, no two electrons can occupy the same state. From this rule follows the discrete orbital levels occupied by electrons in a multi-electron atom. For a single atom, these orbitals remain well separated. However, when multiple identical atoms come into proximity with one another, as is the case in solids, those atomic orbitals overlap and *hybridize*–a fancy term that means they mix in a way that allows the atoms to form stronger bonds, thus minimizing energy. When the number of atoms is large, the number of hybridized orbitals is also large while their energy spacings

are small. This results in a continuum, or band, of allowed energy states for the electrons in that solid. The bandgap of a solid is the range of disallowed energies for electrons in the material. Actual derivation of band structures is outside the scope of this thesis, but readers seeking an excellent resource should look to Prof. Farhan Rana's online, open-source lecture notes for the course *ECE407: Physics of Semiconductors and Nanostructures*.

Of the many energy bands that may exist for a particular material, two bands called the conduction and valence bands are of special importance. The valence band consists of the highest energy electrons while the conduction band is the lowest range of unfilled electron energy states. Somewhere in between these bands lies the Fermi level–the highest energy level of occupied electron states when the material is at absolute zero. The relationship of these bands relative to the Fermi level determine the conductivity of a material and whether it classified as a metal, insulator, or semiconductor.

Conduction happens when electrons are excited from the valence band to the conduction band, leaving behind a hole that also contributes to the current. Metals are excellent conductors because their electronic charges flow easily. From an energy band perspective, this manifests as the overlap of the valence and conduction bands about the Fermi level of a metallic material, meaning they have no bandgap. In contrast, insulators have a large bandgap with the Fermi level lying solidly in the middle, meaning a large amount of energy is needed to excite electrons into the conduction band, making conduction difficult. Finally, semiconductors lie somewhere in between metals and insulators. Semiconductors possess a small bandgap typically on the order 0 eV $< E_g \leq$ 6 eV. The Fermi level of a pure, intrinsic semiconductor usually lies in the middle of the bandgap, but its proximity to the conduction or valence bands can be altered via a process called doping. So-called *extrinsic* semiconductors have been doped to alter the concentrations of electrons (or holes, depending on what the desired majority current carrier is) in the material by introducing impurity atoms during the growth process. Introducing donor dopants in a semiconductor increases the electron concentration and makes the semiconductor more negatively charged, or *n-type*.

Commonly introduced donors in silicon carbide include nitrogen and phosphorus. These donors have five valence electrons compared to silicon and carbon's four valence electrons, so that the extra electron is readily donated for conduction. Anti-electrons, or *holes*, can also be charge carriers, and in fact the direction of current flow in a material is typically defined by the direction of hole flow. Introducing acceptor dopants during growth "sucks up" spare negative charges to make the material more *p-type*, making holes the dominant current carrier. Common acceptors in silicon carbide include aluminum and boron, which both only have three valence electrons.

The incorporation of dopants in semiconductors adds states within the bandgap that are closer to the energy bands. These additional states, or *dopant levels*, are readily occupied by the electrons or holes contributed by the dopants so that the gap between the highest (lowest) lying electrons (holes) in the material and the conduction (valence) band shrinks. In essence, dopant levels in the band shifts the Fermi level to make the material a better conductor of either electrons or holes.

To better understand the effect of dopants in semiconductors, let's revisit some semiconductor physics. The Fermi-Dirac distribution describes the probability $f(E)$ of finding an electron in a particular energy E near the band edge is:

$$f(E) = \frac{1}{e^{(E-E_f)/kT} + 1} \approx \frac{1}{e^{(E-E_f)/kT}}$$

Where k is Boltzmann's constant, E_f is the Fermi level, and T is the temperature. The Fermi-Dirac distribution tells us that the probability of an electron having energy less than the Fermi level is high, whilst the probability of an electron having an energy greater than the Fermi level is low. The probability of an electrong having energy equal to the Fermi level is exactly 50%, no matter the temperature. The density of states $g(E)$ per unit volume for

carriers is:

$$g(E) = \begin{cases} D_v\sqrt{E_v - E} & \text{for } E < E_v \\ D_c\sqrt{E - E_c} & \text{for } E_c < E \\ 0 & \text{for } E_v < E < E_c \end{cases}$$

Where $D_{v(c)} = \frac{(2m^*_{h(e)})^{3/2}}{2\pi^2\hbar^3}$ and $E_{v(c)}$ is the valence (conduction) band energy. If $g(E)dE$ is the density of energy states per cubic centimeter per increment of energy, then $f(E)g(E)dE$ is the occupational probability times that density. The integral of this quantity gives us the number of electrons per unit volume n:

$$n = \int_{E_c}^{\infty} f(E)g(E)dE$$

$$= \frac{\sqrt{\pi}D_c(kT)^{3/2}}{2}e^{(E_f - E_c)/kT}$$

$$= N_c e^{-(E_c - E_f)/kT}$$

An electron that *does not* occupy some energy state is equivalent to a hole that *does* occupy that energy state. Thus, the probability of a hole occupying some energy state is $1 - f(E)$ and the number of holes per unit volume is p:

$$p = \int_{-\infty}^{E_v}(1 - f(E))g(E)dE = N_v e^{-(E_f - E_v)/kT}$$

$$= \frac{\sqrt{\pi}D_v(kT)^{3/2}}{2}e^{(E_v - E_f)/kT}$$

$$= N_v e^{-(E_f - E_v)/kT}$$

What was the point of doing this derivation? In real life, we tend to know what the carrier concentrations, n and p, are based on growth parameters. (Experimental determination of carrier concentrations can be done with a Hall measurement). For intrinsic silicon, the

electron and hole concentrations are the same: $n_i = n = p = 1 * 10^{10}$ cm^{-3}. Thus, if we know the carrier concentration of a material, we know how far the Fermi level is from the top of the valence band $E_f - E_v$, or from the bottom of the conduction band $E_c - E_f$. For an intrinsic semiconductor ($n = p$) we see that at $T = 0$ the Fermi level is exactly in the middle of the valence and conduction edge:

$$\frac{\sqrt{\pi} D_v (kT)^{3/2}}{2} e^{\frac{E_v - E_f}{kT}} = \frac{\sqrt{\pi} D_c (kT)^{3/2}}{2} e^{\frac{E_f - E_c}{kT}}$$

$$E_f = \frac{E_v + E_c}{2} + \frac{kT}{2} ln(\frac{D_v}{D_c})$$

What about the introduction of dopants and how that manifests in the equations we just explored? If we multiply the expressions for n and p together:

$$np = N_v N_c e^{-(E_c - E_v)/kT} = N_v N_c e^{-E_g/kT}$$

We see that no matter the dopant concentration, the np product is a constant that depends on the bandgap E_g and the temperature. This relationship is called the semiconductor equilibrium relation and is written:

$$np = n_i^2$$

$$n_i = \sqrt{N_c N_v} e^{\frac{-E_g}{2kT}}$$

If impurities are introduced with donor concentration N_d or acceptor concentration N_p, charge neutrality dictates that $n + N_a = p + N_d$. Using the fact that $np = n_i^2$, we can solve for n and p:

$$n = \frac{N_d - N_a}{2} \Big[(\frac{N_d - N_a)^2 + n_i^2}{2}) \Big]^{1/2}$$

$$p = \frac{N_a - N_d}{2} \Big[(\frac{N_a - N_d)^2 + n_i^2}{2}) \Big]^{1/2}$$

Two simplifications can be made:

- If the material is n-type, then $N_d - N_a >> n_i$ such that:

$$n = N_d - N_a$$

$$p = \frac{n_i^2}{n}$$

- If the material is p-type, then $N_a - N_d >> n_i$ such that:

$$p = N_a - N_d$$

$$n = \frac{n_i^2}{p}$$

The whole point of this song and dance of deriving dopant concentration relations is to demonstrate that if we know the impurity concentrations and temperature, we can figure out the relationship of the band edges relative to the Fermi level of the semiconductor. From the Fermi-Dirac distribution we see that as things get warmer, the distribution of electron states becomes smeared such that some electrons reside above the Fermi level. This means the semiconductor conducts more readily, as less excitation is needed to promote the highest energy electrons to the conduction band. The inverse argument is made for p-type materials, where holes are the dominant carriers with distribution $1-f(E)$. For a p-type material, as the temperature increases, hole occupation below the Fermi level increases and similarly makes the material more conductive as the energy gap to the valence band decreases. However, in the context of this thesis, perhaps the most important thing to note is that the Fermi level of a semiconductor will determine the dominant charge state of a particular defect at equilibrium. This is discussed in more detail in Section 2.0.10.

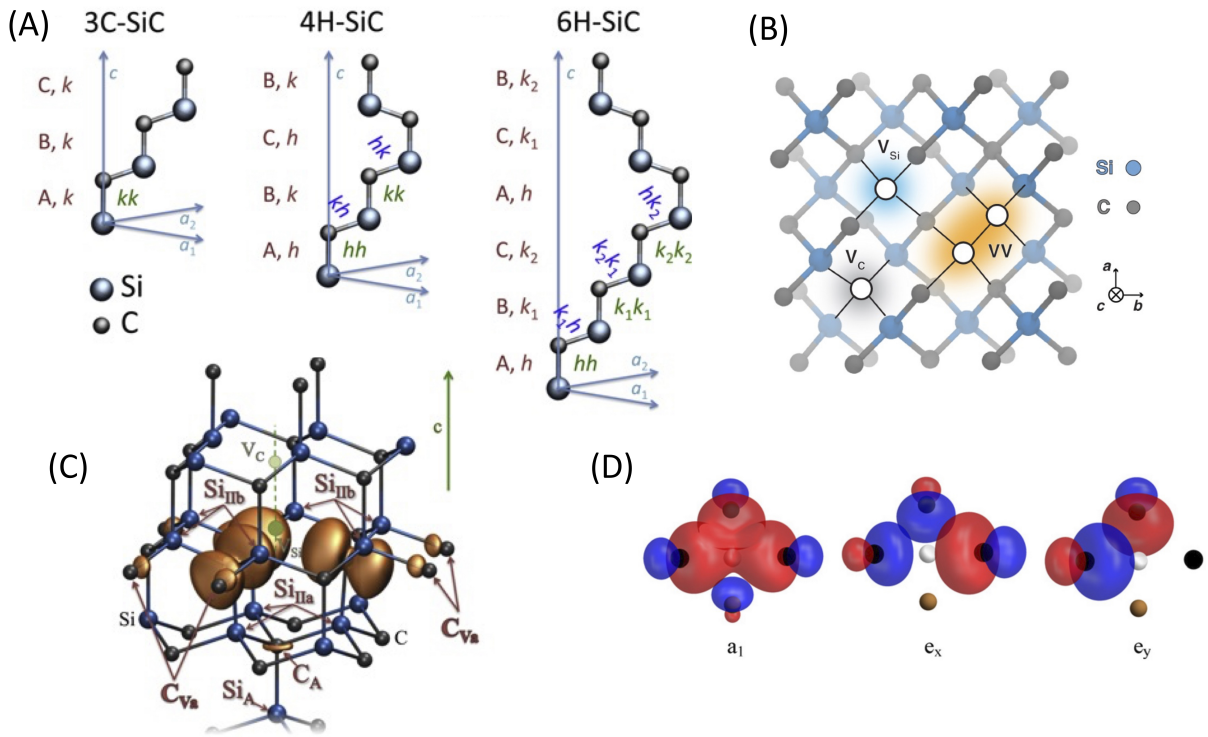

Figure 2.1: Polytypes and defects in silicon carbide. **(A)** 3C, 4H, and 6H polytypes of SiC. Crystal growth occurs along the c-axis (blue arrow). Atoms (or vacancies) occupy quasi-cubic (k) or hexagonal (h) sites. **(B)** carbon vacancy, silicon vacancy, and divacancy complexes, here shown in 3C-SiC. **(C)** Electronic orbital structure of hh divacancy in 4H-SiC. The yellow lobes indicate the spatial distribution of the electrons, which are localized around the carbon atoms. **(D)** a_1, e_x, e_y molecular orbital configuration of the dangling bonds in the divacancy. Red (blue) components indicate the positive (negative) parts of the orbital wavefunction. Figures taken from [2], [3], and [4].

2.0.2 Defects in silicon carbide

Silicon carbide (SiC) is a crystalline semiconductor composed of silicon (Si) and carbon (C) atoms arranged in a periodic lattice. The stacking order of these two atoms can take on hundreds of variations, called polytypes. The most common polytypes of SiC are 4H, 6H, and 3C. In this notation, called Ramsdell notation, the first digit represents the number of layers in a unit cell of the crystal, and the letter represents the type of Bravais lattice. For example, 4H-SiC has a hexagonal lattice with 4 layers in each unit cell, while 3C-SiC has a cubic lattice with 3 layers in each unit cell (Fig. 2.1A).

SiC has many desirable properties as a semiconductor outside of its use as a quantum

platform in our research. It is an extemely durable material with a hardness rating of 9-9.5 on the Mohs scale, which is very close to the Mohs rating of 10 for diamond. It can also withstand extreme electric fields. SiC has an incredibly high breakdown field of the order 10^6 V/cm – over 10 times higher than the breakdown of silicon, meaning it can be operated at extremely high voltages before electrons in the material are ripped away from their atoms and the material loses its semiconducting properties. For a SiC electronic device with order 1 μm thickness, this translates to normal device operation under thousands of volts of bias, making SiC is a popular choice for durable, high power MOSFETs. SiC diodes are also used for UV detection since the SiC bandgap is $E_g = 3.26$ eV (380 nm). This, combined with the excellent temperature durability of SiC, have lead some to use SiC for fire detection. The ruggedness of SiC is also exploited in conjuction with its piezoresistiveness to fabricate micro-electro-mechanical structures (MEMS) for high temperature engine turbine temperature sensing. The ready availability of SiC electronic device is made possible because of well-established SiC growth, doping, and fabrication techniques. This is perhaps the most attractive qualitiy of SiC from a quantum research perspective. Even the meager graduate student can order a fairly cheap cassette of 4H-SiC wafers, take it into the cleanroom, and perform fabrication processes nearly identical to those used for silicon to make the device of their dreams. This flexibility and wafer scalability of the SiC material platform is one of its main selling points when placed in the context of quantum information.

Until now we have only discussed *extrinsic* impurities in semiconductors, such as donors and acceptor species. In reality, any defect or impurity, such as a missing atom in the lattice, will introduce electronic states to the bandstructure or within the bandgap of a semiconductor. If those states are close to the band edge, they are called *shallow* defects. If they are energetically isolated from the bands, they are called *deep* defects. The most common defects in 4H-silicon carbide are the carbon vacancy (V_C), the silicon vacancy (V_{Si}) (Fig. 2.1B). V_C and V_{Si} are both deep defects with energy levels within the SiC bandgap. These defects and their energy levels are discussed in further detail in Section 2.0.10. When

V_C and V_{Si} directly neighbor each other, they form a divacancy complex (V_C-V_{Si}) (Fig. 2.1B). This divacancy complex, and in particular its neutral charge state VV^0 in the 4H polytype of SiC, is the subject of the rest of this thesis.

2.0.3 The neutral divacancy VV^0 in silicon carbide

While some divacancies (V_C-V_{Si}) may naturally exist in off-the-shelf SiC, high density populations can be formed using electron irradiation followed by high temperature annealing. During irradiation, SiC samples are placed in an accelerator, where relativistic electrons bombard and knock out atoms in the crystal lattice to create V_C and V_{Si}. Irradiated samples are then subsequently annealed between $800° - 1200°$C in argon gas for approximately 5-30 minutes. This allows the V_C and V_{Si} to migrate through the SiC lattice and form the energetically favorable V_C-V_{Si} complex. While the temperature range for this annealing process is flexible, there is an upper limit of 1200°C, above which divacancies may actually migrate entirely to the surface and out of the sample.

In 4H-SiC, the divacancy complex can take on one of four inequivalent orientations within the lattice: two along the c-axis, or growth axis, labelled *kk* and *hh*, and two along the basal plane labelled *kh* and *hk* (Fig. 2.1A). The different divacancy orientations are also commonly referred to by their optical fingerprints, as they have different orbital structures and photoluminesce at different frequencies. The *hh*, *kk*, *kh*, and *hk* are known as PL1, PL2, PL3, and PL4, respectively.

2.0.4 The divacancy ground state orbital structure

The c-axis divacancy complex consists of six dangling bonds, three from the neighboring silicon site and three from the neighboring carbon site. These dangling bonds hybridize to form electronic orbital levels that, when filled by the six electrons involved in the divacancy, form a spin-1 ground state that we use as our qubit system. These bonds have C_{3v} symmetry, where C_{3v} is a type of point group with a three-fold axis and three vertical planes of symmetry

(a fancy way of saying that if you rotate it about its axis, it looks the same for three different rotation angles). The c-axis divacancy electronic structure is shown in Fig. 2.1C. Derivation of the orbital structure requires finding the eigenstates that satisfy certain matrix operations performed on the defect. As a note to the reader, this section of the thesis was re-derived from [5], with the help of Alex Bourassa himself (thank you Alex!).

We first start with the six dangling bonds of the divacancy. The set $\{c_1, c_2, c_3\}$ represents the dangling carbon bonds and the set $\{s_1, s_2, s_3\}$ represent the dangling silicon bonds. This composes a 6x6 subspace, where the single particle electron orbitals of the divacancy will be composed of some linear combination of the dangling bonds. The C_{3v} symmetry of the divacancy means that it is invariant under the following transformations (with their shorthand notation in parentheses):

- Identity, or no change (e)
- Clockwise rotation about the c-axis by $2\pi/3$ (C_3^+)
- Counterclockwise rotation about the c-axis by $2\pi/3$ (C_3^-)
- Reflection through one of three planes defined along the c-axis and through one of the dangling bonds ($\sigma_v, \sigma_{v'}, \sigma_{v''}$)

These transformations can be written as 6x6 matrices.

$$e = \begin{pmatrix} 1 & 0 & 0 & 0 & 0 & 0 \\ 0 & 1 & 0 & 0 & 0 & 0 \\ 0 & 0 & 1 & 0 & 0 & 0 \\ 0 & 0 & 0 & 1 & 0 & 0 \\ 0 & 0 & 0 & 0 & 1 & 0 \\ 0 & 0 & 0 & 0 & 0 & 1 \end{pmatrix} \quad C_3^- = \begin{pmatrix} 0 & 0 & 1 & 0 & 0 & 0 \\ 1 & 0 & 0 & 0 & 0 & 0 \\ 0 & 1 & 0 & 0 & 0 & 0 \\ 0 & 0 & 0 & 0 & 0 & 1 \\ 0 & 0 & 0 & 1 & 0 & 0 \\ 0 & 0 & 0 & 0 & 1 & 0 \end{pmatrix} \quad C_3^+ = \begin{pmatrix} 0 & 1 & 0 & 0 & 0 & 0 \\ 0 & 0 & 1 & 0 & 0 & 0 \\ 1 & 0 & 0 & 0 & 0 & 0 \\ 0 & 0 & 0 & 0 & 1 & 0 \\ 0 & 0 & 0 & 0 & 0 & 1 \\ 0 & 0 & 0 & 1 & 0 & 0 \end{pmatrix}$$

$$\sigma_v = \begin{pmatrix} 1 & 0 & 0 & 0 & 0 & 0 \\ 0 & 0 & 1 & 0 & 0 & 0 \\ 0 & 1 & 0 & 0 & 0 & 0 \\ 0 & 0 & 0 & 1 & 0 & 0 \\ 0 & 0 & 0 & 0 & 0 & 1 \\ 0 & 0 & 0 & 0 & 1 & 0 \end{pmatrix} \quad \sigma_{v'} = \begin{pmatrix} 0 & 1 & 0 & 0 & 0 & 0 \\ 1 & 0 & 0 & 0 & 0 & 0 \\ 0 & 0 & 1 & 0 & 0 & 0 \\ 0 & 0 & 0 & 0 & 1 & 0 \\ 0 & 0 & 0 & 1 & 0 & 0 \\ 0 & 0 & 0 & 0 & 0 & 1 \end{pmatrix} \quad \sigma_{v''} = \begin{pmatrix} 0 & 0 & 1 & 0 & 0 & 0 \\ 0 & 1 & 0 & 0 & 0 & 0 \\ 1 & 0 & 0 & 0 & 0 & 0 \\ 0 & 0 & 0 & 0 & 0 & 1 \\ 0 & 0 & 0 & 0 & 1 & 0 \\ 0 & 0 & 0 & 1 & 0 & 0 \end{pmatrix}$$

States composed of linear combinations of the dangling bonds that do not transform into each other via any combination of these operations will have distinct energies and are therefore non-degenerate. For example, no combination of the six operations will "switch" the silicon bonds with the carbon bonds. This lack of coupling between $\{c_1, c_2, c_3\}$ and $\{s_1, s_2, s_3\}$ means that while the transformation matrices are 6x6, the 3x3 matrices in the upper right and lower left quadrants of the larger transformation matrices only contain zeros. This allows us to represent the transformation matrices as carbon or silicon-specific 3x3 matrices:

$$e = \begin{pmatrix} 0 & 0 & 0 \\ 0 & 1 & 0 \\ 0 & 0 & 1 \end{pmatrix} \quad C_3^- = \begin{pmatrix} 0 & 0 & 1 \\ 1 & 0 & 0 \\ 0 & 1 & 0 \end{pmatrix} \quad C_3^+ = \begin{pmatrix} 0 & 1 & 0 \\ 0 & 0 & 1 \\ 1 & 0 & 0 \end{pmatrix}$$

$$\sigma_v = \begin{pmatrix} 1 & 0 & 0 \\ 0 & 0 & 1 \\ 0 & 1 & 0 \end{pmatrix} \quad \sigma_{v'} = \begin{pmatrix} 0 & 1 & 0 \\ 1 & 0 & 0 \\ 0 & 0 & 1 \end{pmatrix} \quad \sigma_{v''} = \begin{pmatrix} 0 & 0 & 1 \\ 0 & 1 & 0 \\ 1 & 0 & 0 \end{pmatrix}$$

The divacancy's orbital configurations will be eigestates of all these transformations. Therefore, we must simultaneously diagonalize all of the 3x3 transformation matrices. This entails finding the change of basis matrix P such that $P^{-1}AP = D$, where A is the transformation

matrix, D is a diagonal matrix, and the columns of P are composed of the eigenstates of A. However, in this case true simultaneous diagonalization is not possible and therefore it is not possible to find true eigenstates of the system. Instead, we perform an operation called block diagonalization using the following basis states found from literature :

$$a_{(1)} = \frac{1}{\sqrt{3}}(c_1 + c_2 + c_3)$$

$$e_{(1),x} = \frac{1}{\sqrt{6}}(2c_1 - c_2 - c_3)$$

$$e_{(1),y} = \frac{1}{\sqrt{2}}(c_2 - c_3)$$

Following from the argument that the silicon and carbon subspaces do not couple and exist in their own separate subspace, these basis states are similarly written for the silicon subspace:

$$a_{(2)} = \frac{1}{\sqrt{3}}(s_1 + s_2 + s_3)$$

$$e_{(2),x} = \frac{1}{\sqrt{6}}(2s_1 - s_2 - s_3)$$

$$e_{(2),y} = \frac{1}{\sqrt{2}}(s_2 - s_3)$$

The transformation matrix $P = \{a_{(i)}, e_{(i),x}, e_{(i),y}\}$ is written:

$$P = \begin{pmatrix} \frac{1}{\sqrt{3}} & \frac{2}{\sqrt{6}} & 0 \\ \frac{1}{\sqrt{3}} & -\frac{1}{\sqrt{6}} & \frac{1}{\sqrt{2}} \\ \frac{1}{\sqrt{3}} & -\frac{1}{\sqrt{6}} & -\frac{1}{\sqrt{2}} \end{pmatrix}$$

Performing the change of basis $P^{-1}AP$, each transformation matrix A is rewritten in terms

of $a_{(i)}, e_{(i),x}$, and $e_{(i),y}$:

$$e = \begin{pmatrix} 1 & 0 & 0 \\ 0 & 1 & 0 \\ 0 & 0 & 1 \end{pmatrix} \quad C_3^- = \begin{pmatrix} 1 & 0 & 0 \\ 0 & \frac{-1}{2} & \frac{-\sqrt{3}}{2} \\ 0 & \frac{\sqrt{3}}{2} & \frac{-1}{2} \end{pmatrix} \quad C_3^+ = \begin{pmatrix} 1 & 0 & 0 \\ 0 & \frac{-1}{2} & \frac{\sqrt{3}}{2} \\ 0 & \frac{-\sqrt{3}}{2} & \frac{-1}{2} \end{pmatrix}$$

$$\sigma_v = \begin{pmatrix} 1 & 0 & 0 \\ 0 & 1 & 0 \\ 0 & 0 & -1 \end{pmatrix} \quad \sigma_{v'} = \begin{pmatrix} 1 & 0 & 0 \\ 0 & \frac{-1}{2} & \frac{\sqrt{3}}{2} \\ 0 & \frac{\sqrt{3}}{2} & \frac{1}{2} \end{pmatrix} \quad \sigma_{v''} = \begin{pmatrix} 1 & 0 & 0 \\ 0 & \frac{-1}{2} & \frac{-\sqrt{3}}{2} \\ 0 & \frac{-\sqrt{3}}{2} & \frac{1}{2} \end{pmatrix}$$

Block diagonalization divides the operations into a 1D subspace (top left element) and a 2D subspace (2x2 matrix in bottom right quadrant). This means that the $a_{(1)}$ state is a true eigenstate of the matrix operations. On the other hand, $e_{(i)x}$ and $e_{(i),y}$ are not true eigenstates since there are off diagonal coupling terms in the 2x2 matrix, meaning some combination of the six matrix operations could transform one state into the other. This lack of invariance means $e_{(i)x}$ and $e_{(i)y}$ are degenerate.

The takeaway here is that there are six possible orbitals $a_{(1)}, a_{(2)}, e_{(1),x}, e_{(2),x}, e_{(1),y}, e_{(2),y}$ for the electrons in the divacancy to occupy (Fig. 2.1D). Where those orbitals lie in energy space relative to the conduction and valence bands, and relative to each other, is calculated using DFT and is beyond the scope of this thesis. From literature, we know that $a_{(1)}$ lies deep within the SiC valence band, $a_{(2)}$ lies near the valence band edge, and the lowest lying of the e levels is associated with carbon. Both $e_{(1)x,y}$ and $e_{(2)x,y}$ lie within the bandgap, with the lower energy of the two associated with carbon (Fig. 2.2).

The orbital levels that we just derived will be filled up with electrons obeying the Pauli exclusion principle. The six electrons involved in the divacancy occupy the $a_{(1)}$ and $a_{(2)}$ orbitals fully, while the lower degenerate $e_{(1)x}$ and $e_{(1)y}$ are each partially filled by a single electron according to Hund's rule. Electrons are fermions and therefore must be antisymmetric under exchange, satisfying the relation $\psi(x_1, x_2) = -\psi(x_2, x_1)$. Thus, the outer product

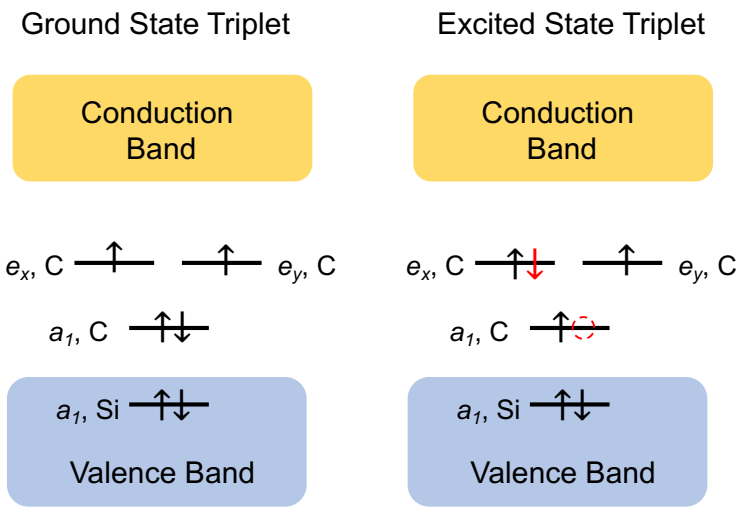

Figure 2.2: Neutral divacancy ground and excited state orbital configuration. In the excited state, an electron leaves the a_1 orbital associated with carbon (red dashed circle) and is promoted to one of the higher lying orbitals (red arrow) associated with carbon. In the triplet excited state configuration, the two unpaired electrons obey fermionic antisymmetry rules and may be in a superposition of the states $|\uparrow\uparrow\rangle$ and $|\downarrow\downarrow\rangle$, corresponding to the $m_s = \pm 1$ character excited states, or in the state $|\uparrow\downarrow + \downarrow\uparrow\rangle$ corresponding to the $m_s = 0$ character excited states (see Table 2.2).

of a given orbital configuration with the spin configuration must be antisymmetric. For example, the symmetric orbital configuration $|e_x e_x + e_y e_y\rangle$ can only have the antisymmetric spin singlet (S=0) configuration $|\uparrow\downarrow - \downarrow\uparrow\rangle$, forming $|e_x e_x + e_y e_y\rangle \otimes |\uparrow\downarrow - \downarrow\uparrow\rangle$. Alternately, the antisymmetric orbital configuration $|e_x e_y - e_y e_x\rangle$ can have any one of the three antisymmetric spin triplet (S=1) configurations $|\uparrow\uparrow\rangle$, $|\downarrow\downarrow\rangle$, $|\uparrow\downarrow + \downarrow\uparrow\rangle$ (Table 2.1).

2.0.5 The divacancy excited state orbital structure

So far, discussion has been limited to the configuration of the ground state manifold. Excitation of the divacancy promotes a single electron from the $a_{(2)}$ level to one of the higher lying $e_{(1)x}$ and $e_{(1)y}$ levels. Using the same particle exchange rules for electrons, one can derive the excited state manifold orbital structure. The orbital and spin configurations of the eigenstates of the divacancy are shown in Table 2.2, as adapted from [6]. From Table 2.2, we see that out of the six triplet states (A_1, A_2, E_1, E_2, E_x, E_y), only E_x and E_y have spin

Table 2.1: Ground state configurations of the neutral divacancy in SiC. Table adapted from Ref. [6]. Overall states are always antisymmetric. ${}^1E_1$,${}^1E_2$,${}^1A_1$ are singlet (S=0) states.

Orbital	**Spin**	**State Name**
$\lvert e_x e_y - e_y e_x \rangle$	$\lvert\downarrow\downarrow\rangle$ $m_s = -1$	${}^3A_2$
	$\lvert\uparrow\uparrow\rangle$ $m_s = +1$	
	$\lvert\uparrow\downarrow + \downarrow\uparrow\rangle$ $m_s = 0$	
$\lvert e_x e_x - e_y e_y \rangle$	$\lvert\uparrow\downarrow - \downarrow\uparrow\rangle$	${}^1E_1$
$\lvert e_x e_y + e_y e_x \rangle$	$\lvert\uparrow\downarrow - \downarrow\uparrow\rangle$	${}^1E_2$
$\lvert e_x e_x + e_y e_y \rangle$	$\lvert\uparrow\downarrow - \downarrow\uparrow\rangle$	${}^1A_1$

Table 2.2: Excited state configurations of the neutral divacancy. Table adapted from Ref. [6]. Overall states are always antisymmetric. ${}^1E_x$,${}^1E_y$,${}^1A_1$ are singlets (S=0).
$E_\pm = |a_2 e_\pm - e_\pm a_2\rangle$, $e_\pm = \mp(e_x \pm i e_y)$, $|X\rangle = (|E_-\rangle - |E_+\rangle)/2$, $|Y\rangle = i(|E_-\rangle + |E_+\rangle)/2$

Configuration (Orbital $\otimes$ Spin)	**State Name**
$\lvert E_-\rangle \otimes \lvert\uparrow\uparrow\rangle - \lvert E_+\rangle \otimes \lvert\downarrow\downarrow\rangle$	A_1
$\lvert E_-\rangle \otimes \lvert\uparrow\uparrow\rangle + \lvert E_+\rangle \otimes \lvert\downarrow\downarrow\rangle$	A_2
$\lvert E_-\rangle \otimes \lvert\downarrow\downarrow\rangle - \lvert E_+\rangle \otimes \lvert\uparrow\uparrow\rangle$	E_1
$\lvert E_-\rangle \otimes \lvert\downarrow\downarrow\rangle + \lvert E_+\rangle \otimes \lvert\uparrow\uparrow\rangle$	E_2
$\lvert Y\rangle \otimes \lvert\uparrow\downarrow + \downarrow\uparrow\rangle$	E_y
$\lvert X\rangle \otimes \lvert\uparrow\downarrow + \downarrow\uparrow\rangle$	E_x
$\lvert a_2 e_x + e_x a_2\rangle \otimes \lvert\uparrow\downarrow - \downarrow\uparrow\rangle$	${}^1E_x$
$\lvert a_2 e_y + e_y a_2\rangle \otimes \lvert\uparrow\downarrow - \downarrow\uparrow\rangle$	${}^1E_y$
$\lvert a_2 a_2\rangle \otimes \lvert\uparrow\downarrow - \downarrow\uparrow\rangle$	${}^1A_1$

configuration $|\uparrow\downarrow + \downarrow\uparrow\rangle$ corresponding to the $m_s = 0$ spin sublevel. A_1, A_2, E_1, and E_2 are in a superposition of $|\uparrow\uparrow\rangle$ and $|\downarrow\downarrow\rangle$, corresponding to $m_s = +1$ and $m_s = -1$, respectively. Thus, the E_x or E_y states are referred to as being "$m_s = 0$ character," and the A_1, A_2, E_1, and E_2 levels are referred to as being "$m_s = \pm 1$ character." The singlet excited state configurations are also listed in Table 2.2.

The spin and orbital configurations do not give any intuition behind the energy ordering of these states that we see in experiment (Fig. 2.3A). Here, we introduce two interactions—the spin-orbit interaction and the spin-spin interaction—which act to lift the degeneracy of A_1, A_2, E_1, E_2, E_x and E_y. Spin-orbit interactions arise from relativistic effects between an electron and a central nucleus. This interaction consists of axial (z) and non-axial components (x, y), where the axial part of the interaction lifts the degeneracy of states with

non-zero angular momentum (triplet excited state orbitals). While direct derivation of the effects of spin-orbit coupling is not important and should be left to theorists, one can express the effects of spin-orbit coupling in the excited state triplet manifold [6] as:

$$H_{SO} = \lambda_z(|A_1\rangle\langle A_1| + |A_2\rangle\langle A_2| - |E_1\rangle\langle E_1| - |E_2\rangle\langle E_2|)$$

Where λ_z is the strength of the axial part of the interaction. From the Hamiltonian it becomes obvious that the A_1 and A_2 states are higher in energy than the E_x and E_y states by λ_z, while the E_1 and E_2 states are higher in energy than the E_x and E_y states by λ_z (Fig. 2.3B). There are also non-axial components of the spin-orbit interaction, with strength $\lambda_{x,y}$ ($\lambda_\perp$). These components act to non-radiatively link the non-zero spin projection triplet states ($m_s = \pm 1$) with spin-singlets (S=0) (Fig. 2.3C). This directly contributes to the overall phenomena of a non-radiative, non-spin conserving intersystem crossing (ISC) [7] whereby the defect decays via the singlet $^1A_1$ and $^1E_1$ states. While the exact rates of coupling in and out of these states are not well-characterized for the divacancy in 4H-SiC, we do know that $m_s = \pm 1$ excited states couple preferentially to $m_s = 0$ ground states via the singlet ISC [8]. This preferential coupling provides us with a mechanism to perform divacancy spin initialization with over 99% fidelity. Because the spin-orbit interaction links the qubit spin state to orbital degress of freedom, such as charge and phonons, defects with weak spin-orbit coupling are typically desirable so that qubit coherence is not affected by these environmental factors. Additionally, defect systems associated with lighter nuclei are more desirable from a coherence perspective because the spin-orbit coupling strength scales proportionally with the atomic number Z [9], although this is not a hard and fast rule.

Spin-spin interactions further lift degeneracies while inducing mixing between states with un-like spin projections [6]:

$$\begin{aligned} H_{ss} =& \Delta\left(|A_1\rangle\langle A_1| + |A_2\rangle\langle A_2| + |E_1\rangle\langle E_1| + |E_2\rangle\langle E_2|\right) - 2\Delta\left(|E_x\rangle\langle E_x| + |E_y\rangle\langle E_y|\right) \\ &+ 2\Delta'\left(|A_2\rangle\langle A_2| - |A_1\rangle\langle A_1|\right) + \Delta''\left(|E_1\rangle\langle E_y| + |E_y\rangle\langle E_1| - \mathrm{i}|E_2\rangle\langle E_x| + \mathrm{i}|E_x\rangle\langle E_2|\right) \end{aligned}$$

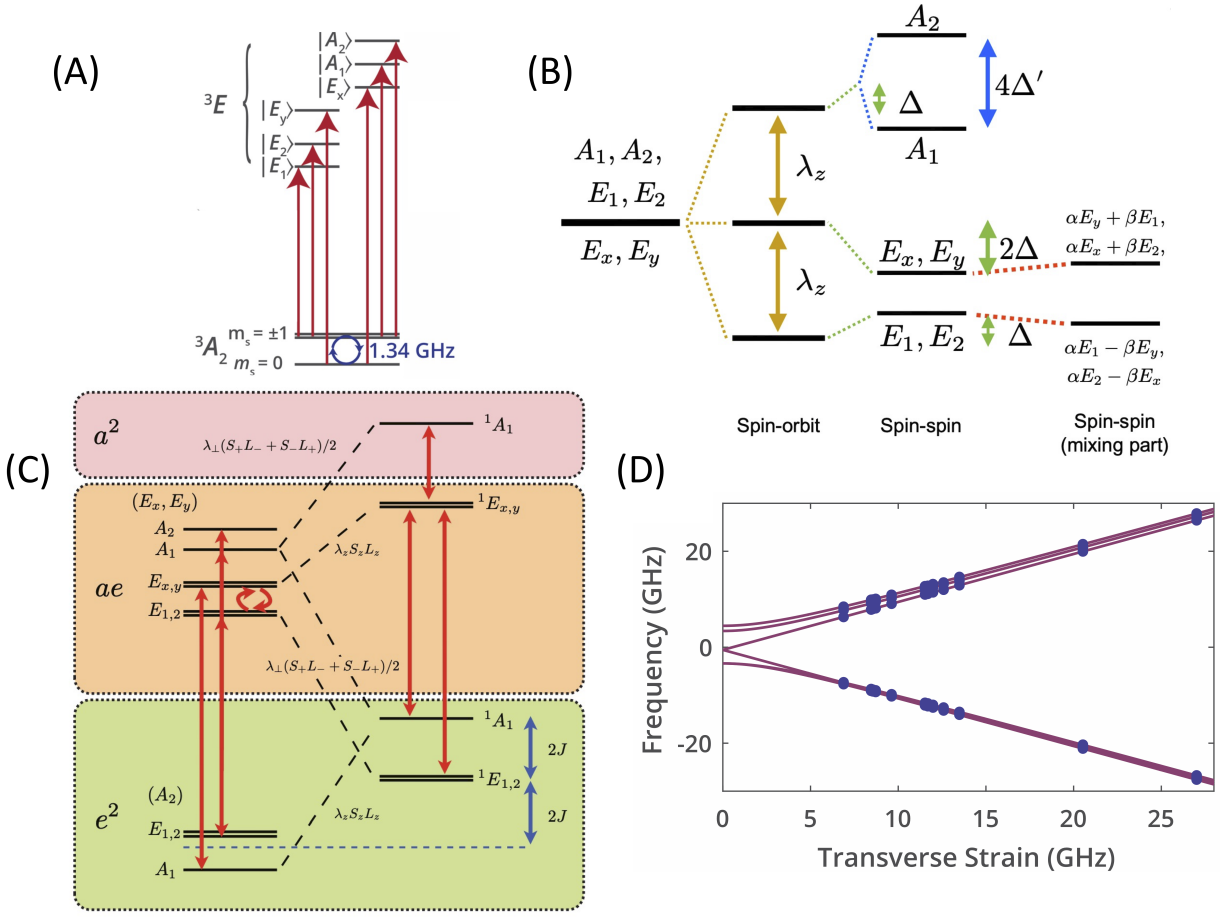

Figure 2.3: **(A)** Divacancy triplet ground to excited state optical transitions. One-photon, resonant excitation is spin conserving. **(B)** The effects of spin-orbit and spin-spin interactions act to lift degeneracies of the orbitals and to mix the orbitals. **(C)** Couplings between the spin triplet (left) and spin singlet (right) orbitals due to axial (λ_z) and transverse ($\lambda_\perp$) spin-orbit coupling. This figure is taken from [6] and portrays the $^1A_1$ and $^1E_{1,2}$ levels that compose the intersystem crossing (ISC) for the NV$^-$ in diamond. For the divacancy, the intersystem crossing mechanism is not extremely well understood, but is likely similar to that of the NV$^-$. Characterization of the branching ratios into the ISC can be found in [10] **(D)** Effect of transverse strain on divacancy orbital energies. Increasing the transverse strain applied to c-axis defects mixes the orbital energies such that spin-selectivity during resonant excitation may suffer. Figures taken from [6] and [10].

Where here the degeneracy between A_1 and A_2 is lifted by $2\Delta'$, the and there is mixing between E_1 and E_y, and E_2 and E_x, respectively (Fig. 2.3B).

The most pronounced effect that varies widely from defect to defect is the transverse strain coupling. Transverse strain further splits and mixes the triplet excited states into groupings consisting of a lower branch (E_1, E_2, E_y) and upper branch (E_x, A_1, A_2), where the transverse strain is equal to approximately half of the energy splitting between E_x and E_y [8]. When a defect is subject to high strain, the orbitals within each branch overlap in energy, reducing the spin-selectivity of optical excitation (Fig. 2.3D). Thus, during typical divacancy experiments, defects with a transverse strain splitting of around 5-20 GHz are usually selected due to the higher *cyclicity* (see Section 2.0.6) and therefore higher readout fidelity. A full treatment of the spin-orbit, spin-spin, and strain couplings are found in Ref. [6], and experimental characterization of these interactions in the divacancy can be found in Ref. [10]. However, from the perpsective of the experimentalist working with the divacancy, it is generally sufficient to realize that (1) not all the divacancy optical transitions have purely $m_s = 0$ or $m_s = \pm 1$ spin character, and (2) spin-mixing in the excited state destroys the fidelity of optical readout, and one way to mitigate these effects is to work with low strain defects.

2.0.6 Spin flips in the spin-photon interface

Resonant (direct) optical excitation from the ground state triplet into any of the six spin triplet excited states is spin-selective, meaning the transition is only allowed if it is spin conserving ($\Delta m_s = 0$). For example, a divacancy in the $m_s = 0$ ground state sublevel can only be excited to E_x or E_y which are both $m_s = 0$ character (Fig. 2.3A). Relaxation back to the ground state is typically accompanied by emission of a photon (photoluminescence), which is collected and read out with a photodetector. The spin-selectivity of the optical transitions provides the basis for spin contrast during readout. For example, if a laser is tuned to the E_x transition energy, a divacancy will only undergo excitation and photoluminesce

if it is in $m_s = 0$. Alternately, if the same laser addresses a defect prepared to $m_s = +1$, the defect will not undergo excitation and remains "dark." If the divacancy is in an equal superposition of $m_s = 0$ and $m_s = +1$, it will photoluminesce with 50% probability.

The triplet ground to excited state optical transitions of the divacancy are often referred to as having "highly cyclitiy" because they can be excited and relax many times while still conserving their initial spin state ($\Delta m_s = 0$). Readout is typically performed by exciting the $m_s = 0$ character transitions because they have higher cyclicity than the $m_s = \pm 1$ ($A_1,\ A_2,\ E_1,\ E_2$) transitions due to smaller spin-orbit couplings to the singlet state inter-system crossing (ISC) that preferentially decay to $m_s = 0$, meaning more photoluminescence can be extracted per readout. Despite the high cyclicity of the $m_s = 0$ character optical transitions, there are still non-zero couplings due to mixing with $m_s = \pm 1$ through the spin-spin interaction and transverse strain [10] (Section 2.0.5). This mixing results in non-spin conserving decay, or "spin flips," out of the excited state, impairing the cyclicity of the divacancy optical transitions, and thus reducing the number of times a defect prepared to some initial spin state can undergo $\Delta m_s = 0$ relaxation from the optical excited state. This concept of cyclicity, or lack thereof, is a ridiculously critical part of spin-defect readout and will be incredibly important when we arrive at the discussion of achieving high-fidelity, single-shot readout of single divacancies.

Because there are a finite number of spin-conserving ground to excited state transitions a divacancy can undergo before it spin flips and information is lost, optical readout cannot last indefinitely. After some amount of optical excitation, the photoluminescence that the defect emits does not accurately represent the state the defect was initially in (e.g. a defect prepared to the $m_s = 0$ state undergoes a spin flip and registers as $m_s = \pm 1$ due to lack to photoluminescence when subject to E_x resonant light). Registering of the defect in a state that it isn't supposed to be in is called *infidelity* and is a huge issue for spin defect based systems in general. The probability p of a spin-flip for the divacancy is approximately 0.1%, meaning that there is one spin-flip per thousand trips to the triplet excited state. However,

instead of talking in terms of percentages, a quantity called the "spin-flip time" (τ_{sf}) is often quoted to characterize defects in a laboratory context. This spin-flip time is measured by preparing the defect to $m_s = 0$, and tracking the PL as a function of time as it is continuously excited with either E_x or E_y resonant light. The characteristic timescale of the exponential PL decay is τ_{sf}. Assuming most time is spent occupying the excited state, rather than entering or exiting it, the spin flip rate ($1/\tau_{sf}$) is given by $p * \Gamma$, where Γ is the excited state lifetime and p is the probability of a spin flip, as discussed earlier. Since the optical transition rate is power-dependent, the excited state lifetime Γ is also very much a power-dependent quantity. During spin-flip lifetime measurements, defects are typically driven "at saturation," meaning the its optical transition cannot be excited any faster, and the defect spends 50% of the time in the excited state. At saturation, Γ is about 10 ns, corresponding to a spin-flip time of several microseconds. The spin-flip time will become longer as the readout laser power is decreased, but the spin-flip time at saturation is typically quoted because it generally eliminates the power-variability of the spin-flip timescales, although at high laser powers other effects such as stimulated emission and ionization will begin to dominate. Spin-flips are the main source of infidelity in any measurement involving the spin-photon interface and, as we shall see, they are the main hindrance to achieving single-shot readout of the spin-state.

2.0.7 The zero-phonon line and phonon sideband

The unfortunate reality is that only a small percentage of excited to ground state transitions are spin-conserving. While the divacancy may undergo a spin-flip due to decay via the intersystem crossing or spin-mixing in the excited state, the defect may also undergo spin flips due to phonon-assisted transition. When this happens, decay is mediated through the emission of a quanta of vibration called a phonon, plus a lower energy photon [11]. The spectrum of wavelengths that spin defects emit can thus be divided into a zero-phonon line (ZPL), indicating direct excited to ground state decay, and a broader phonon sideband

(PSB) (Fig. 2.4). The probability of phonon-assisted photon emission is given by the overlap integral of the wavefunctions of the ground and excited vibronic states [11], where it is assumed that the harmonic oscillator-like vibronic modes are identical regardless of whether the defect is in its ground or excited state. The intensity of these phonon-assisted transitions is dictated by the Franck-Condon principle, which says that transitions with the greatest wavefunction overlap occur at the highest rate. Thus, a transition may involve a high degree of overlap of the vibronic modes while only inducing emission of a photon with energy E that is less than the difference in the ground and excited state levels (E_{ge}). The remainder of the energy ($E_{ge} - E$) is effectively "made up" by a vibration.

Only ZPL photons can be used in spin-photon entanglement schemes [12], since phonon-assisted transitions do not necessarily obey spin conservation. Unfortunately, for defects such as VV^0 in SiC and the NV^- in diamond, the rate of emission into the ZPL, or the Debye-Waller Factor (DWF), is usually only a couple of percent [10, 13]. The low DWF poses a huge hindrance to the rate of spin-photon entanglement generation. Thus, it is common to use photonic resonator structures to enhance the rate of emission into the ZPL [14, 15]. Despite these efforts, spin-flips ultimately hinder the overall readout fidelity of spin defect systems, and limit the duration of time the defect can be optically read out (and therefore also limit the amount of signal that can be collected). Addressing these issues of low signal and infidelity that stem from spin-non conserving transitions (spin-flips) is what ultimately led to the experimental work covered in the last two sections of this thesis.

Additionally, in order for remote entanglement between two defects to occur, they must produce indistinguishable ZPL photons. This means that the defects must emit at the exact same frequency. This is challenging because multiple factors such as the charge and strain environment will cause variations in the orbital splittings from defect to defect. However, recent demonstrations have shown the ability to shift the frequency of divacancy emission in doped SiC diode structures using electric fields [17], opening up the possibility of tuning the ZPLs of two remote divacancies into resonance with each other.

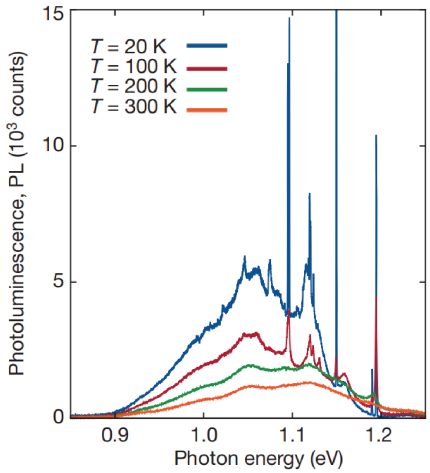

Figure 2.4: Divacancy photoluminescence spectra reveals the broad phonon sideband below 1.09 eV and six sharp zero phonon lines, corresponding to six defect PL lines (PL1-PL6). As the divacancy is cooled down to cryogenic temperatures, the zero phonon lines become more pronounced, corresponding to a higher Debye Waller Factor. Figure taken from [16].

As a final note, since resonant laser excitation is the same frequency as ZPL photons emitted from a defect, and therefore the two cannot be discerned, collection of photoluminescence is commonly performed "on the sideband." This means that in confocal setups the laser excitation frequency is filtered out an only photons in the PSB are routed to the photodetector. The logistics of this filtering is discussed in Section 4.1.8.

2.0.8 Ground state Hamiltonian of the divacancy

Zero-field splitting

The spin triplet configurations within the ground state $^3A_2$ level form the optically addressable qubit basis used in experiment. These states are more commonly referred to as $m_s = +1$, $m_s = 0$, and $m_s = -1$ for $|\uparrow\uparrow\rangle$, $|\uparrow\downarrow\rangle + |\downarrow\uparrow\rangle$, and $|\downarrow\downarrow\rangle$ respectively. The energy separation of these levels are determined by the ground state Hamiltonian, which has many terms that take into consideration factors such as the magnetic field, the presence of nearby spin-carrying nuclei, and other nearby electronic dipoles. In the absence of these other factors, the most basic ground state Hamiltonian describes the spin-spin interaction of the two

unpaired electrons:

$$\hat{H}_{gs} = \hat{H}_0 = \frac{1}{\hbar}(\hat{S} \cdot \hat{D} \cdot \hat{S})$$

Here, $\hat{S} = (\hat{S}_x, \hat{S}_y, \hat{S}_z)$ is the spin-1 operator, and $\hat{D}$ is the zero-field splitting tensor:

$$\hat{S}_x = \frac{\hbar}{\sqrt{2}} \begin{pmatrix} 0 & 1 & 0 \\ 1 & 0 & 1 \\ 0 & 1 & 0 \end{pmatrix} \quad \hat{S}_y = \frac{\hbar}{\sqrt{2}} \begin{pmatrix} 0 & -i & 0 \\ i & 0 & -i \\ 0 & i & 0 \end{pmatrix} \quad \hat{S}_z = \hbar \begin{pmatrix} 1 & 0 & 0 \\ 0 & 0 & 0 \\ 0 & 0 & -1 \end{pmatrix}$$

$$\hat{D} = \begin{pmatrix} D_x & 0 & 0 \\ 0 & D_y & 0 \\ 0 & 0 & D_z \end{pmatrix}$$

Expanding the dot product $\hat{H}_{gs} = \frac{1}{\hbar}(\hat{S} \cdot \hat{D} \cdot \hat{S})$:

$$H_{gs} = \frac{1}{\hbar}(D_x \hat{S}_x^2 + D_y \hat{S}_y^2 + D_z \hat{S}_z^2)$$

$$= \hbar \begin{pmatrix} \frac{D_x}{2} + \frac{D_y}{2} + D_z & 0 & \frac{D_x}{2} - \frac{D_y}{2} \\ 0 & D_x + D_y & 0 \\ \frac{D_x}{2} - \frac{D_y}{2} & 0 & \frac{D_x}{2} + \frac{D_y}{2} + D_z \end{pmatrix}$$

The zero-field splitting tensor $\hat{D}$ is traceless, meaning that $D_x + D_y + D_z = 0$. Additionally, the longitudinal (D) and transverse (E) crystal field splittings can be written $D = \frac{3}{2}D_z$ and $E = \frac{1}{2}(D_x - D_y)$. Making these substitutions:

$$\hat{H}_{gs} = \begin{pmatrix} \frac{D_z}{2} & 0 & E \\ 0 & -D_z & 0 \\ E & 0 & \frac{D_z}{2} \end{pmatrix} = \begin{pmatrix} \frac{D}{3} & 0 & E \\ 0 & -\frac{2D}{3} & 0 \\ E & 0 & \frac{D}{3} \end{pmatrix}$$

For defects with C_{3v} symmetry, such as the hh and kk divacancies, the transverse splitting E is zero (this is not the case for Basal divacancies [18, 19]):

$$\hat{H}_{gs} = \hbar \begin{pmatrix} \frac{D}{3} & 0 & 0 \\ 0 & -\frac{2D}{3} & 0 \\ 0 & 0 & \frac{D}{3} \end{pmatrix}$$

Because the zero-field splitting Hamiltonian is a diagonal matrix, the eigenenergies λ_i and eigenstates $\vec{\boldsymbol{v}}_i$ are obvious:

$$\lambda_{+1} = \frac{D}{3} \qquad \vec{\boldsymbol{v}}_{+1} = |m_s = +1\rangle = \begin{pmatrix} 1 \\ 0 \\ 0 \end{pmatrix}$$

$$\lambda_{0} = \frac{-2D}{3} \qquad \vec{\boldsymbol{v}}_{0} = |m_s = 0\rangle = \begin{pmatrix} 0 \\ 1 \\ 0 \end{pmatrix}$$

$$\lambda_{-1} = \frac{D}{3} \qquad \vec{\boldsymbol{v}}_{-1} = |m_s = -1\rangle = \begin{pmatrix} 0 \\ 0 \\ 1 \end{pmatrix}$$

Thus, the spin sublevels of the spin-1 system are the eigenstates of the zero-field splitting Hamiltonian, where $|m_s = +1\rangle$ and $|m_s = -1\rangle$ are degenerate and are separated in energy by D from $|m_s = 0\rangle$. The values of D for the kk and hh divacancy are around 1.3 GHz ($5.3 * 10^{-6}$ eV) from previous studies. Next, we will explore how the degeneracy between $|m_s = +1\rangle$ and $|m_s = -1\rangle$ is lifted by Zeeman splitting the sublevels through application of an external magnetic field.

Zeeman Effect

With application of an external magnetic field $\vec{\boldsymbol{B}}$, the ground state Hamiltonian increases slightly in complexity with an added Zeeman term $\hat{H}_B$:

$$\hat{H}_{gs} = \hat{H}_0 + \hat{H}_B$$

$$\hat{H}_B = g_e \mu_B \vec{\boldsymbol{B}} \cdot \vec{\boldsymbol{S}}$$

Where g_e is the electron g-factor and $\mu_B = \frac{e\hbar}{2m_e}$ is the Bohr magneton. The g-factor is in reality a g-tensor, describing the magnetic moment for a particular magnetic field orientation. However, for the divacancy, the only non-zero elements are the diagonal elements and are all approximately equal to 2. The orientation along the z-axis is the longitudinal ($\|$) axis and the x and y axes are the transverse ($\perp$) axes. Typically in experiments the applied magnetic field will be composed of a static longitudinal component applied with a permanent magnet or coil and a time-varying transverse component applied through microwave striplines on the SiC sample surface:

$$\vec{\boldsymbol{B}}(t) = B_z + B_x = B_z + I(t)sin(\omega t) + Q(t)cos(\omega t)$$

Here, the amplitude of the out of phase components of the time varying field can be modulated using a signal generator using a technique called IQ modulation. $\hat{H}_B$ is rewritten:

$$\hat{H}_B = 2\mu_B(\vec{\boldsymbol{B}}_x(t)\hat{S}_x + \vec{\boldsymbol{B}}_z\hat{S}_z) =$$

$$= 2\mu_B \begin{pmatrix} B_z & I(t)cos(\omega t) + Q(t)sin(\omega t) & 0 \\ I(t)cos(\omega t) + Q(t)sin(\omega t) & 0 & I(t)cos(\omega t) + Q(t)sin(\omega t) \\ 0 & I(t)cos(\omega t) + Q(t)sin(\omega t) & -B_z \end{pmatrix}$$

There are two main points to note here. First, the degeneracy of the $|m_s = \pm 1\rangle$ states is lifted in the presence of a static field due to Zeeman splitting by $2\mu_B B_z$. This separation corresponds roughly to 2.79 MHz/Gauss. Second, there are off diagonal terms that couple $|m_s = \pm 1\rangle$ to $|m_s = 0\rangle$, but no off diagonal terms that couple $|m_s = +1\rangle$ to $|m_s = -1\rangle$. Another way of saying this is that $\Delta m_s = 2$ transitions are magnetically forbidden.

A change of basis to a rotating frame can be made by first separating out the time-invariant and time-varying components and using the rotating wave approximation. However, even without this treatment, it is obvious from the Hamiltonian that by modulating the amplitudes $I(t)$ and $Q(t)$ for certain durations t, the coupling between $|m_s = 0\rangle$ and $|m_s = \pm 1\rangle$ can be controlled to perform arbitrary qubit rotations about the Bloch sphere.

Electric fields and strain

Electric fields and strain couple to the divacancy in the same way. Returning to the picture of the bare Hamiltonian without the effects of magnetic fields and ignoring shear terms, we can generally write the effects of strain and electric fields as [20]:

$$\hat{H}_e = \Pi_z(\hat{S}_z^2 + \frac{S(S+1)}{3}\mathbb{I}) + \Pi_x(\hat{S}_y^2 + \hat{S}_x^2) + \Pi_y(\hat{S}_x\hat{S}_y + \hat{S}_y\hat{S}_x)$$

Where Π_i represents the electric and strain fields along a given axis. Specifically:

$$\Pi_{x,y} = E_{x,y}^0 + d_\perp F_{x,y} + e_\perp \epsilon_{x,y}$$

$$\Pi_z = D + d_\parallel F_z + e_\parallel \epsilon_z$$

Where D and $E_{x,y}^0$ are the crystal field splittings, F_i is the electric field, ϵ_i is the strain field, $d_{\perp,\parallel}$ are the spin-electric field coupling constants, and $e_{\perp,\parallel}$ are the spin-strain coupling constants. For hh and kk divacancies in SiC with C_{3v} symmetry, $E_{x,y}^0 = 0$. Also note that the term $\frac{S(S+1)}{3}$ is a global energy offset that ensures that the trace of the diagonal terms

of $\hat{H}_e$ is zero. The elements of the 3 by 3 matrix $\hat{H}_e$ are:

$$\begin{matrix} \frac{1}{3}(D + d_{\parallel}F_z + e_{\parallel}\epsilon_z) & 0 & d_{\perp}(-F_x - iF_y) + e_{\perp}(-\epsilon_x - i\epsilon_y) \\ 0 & \frac{-2}{3}(D + d_{\parallel}F_z + e_{\parallel}\epsilon_z) & 0 \\ d_{\perp}(-F_x + iF_y) + e_{\perp}(-\epsilon_x + i\epsilon_y) & 0 & \frac{1}{3}(D + d_{\parallel}F_z + e_{\parallel}\epsilon_z) \end{matrix}$$

We see that any strain or electric field shifts the energy of $|m_s = 0\rangle$ down by $\frac{-2}{3}(d_{\parallel}F_z + e_{\parallel}\epsilon_z)$ and shifts the energies of $|m_s = \pm 1\rangle$ up by $\frac{1}{3}(d_{\parallel}F_z + e_{\parallel}\epsilon_z)$. Detailed experimental characterization of the spin-electric and spin-strain parameters for the divacancy can be found in [21] and [22]. Additionally, the off diagonal terms couple $|m_s = +1\rangle$ and $|m_s = -1\rangle$ together, which are magnetically forbidden transitions that cannot be accessed through typical microwave driving but can be accessed here through electric fields and strain. Previous work with the divacancy has demonstrated $\Delta m_s = 2$ spin transitions through electrically driven spin resonance [21] and acoustic driving [22].

Hyperfine coupling and greater system Hamiltonian

Up until now, only the effects of magnetic, electric, and strain fields have been considered. In reality, there are a host of other parameters that shift the energies of the divacancy ground state sublevels and couple them together. The divacancy spin does not exist in a vacuum, but rather is part of a greater ecosystem of charges and nuclei in the lattice. The entire electron-nuclear system ground state Hamiltonian can be written:

$$\hat{H} = \hat{H}_B + \hat{H}_e + \underbrace{\sum_i S \cdot A_i \cdot I_i}_{nuclear\ hyperfine} + \underbrace{\sum_{j>i} I_i \cdot P^n_{i,j} \cdot I_j}_{nuclear\ dipole-dipole} + \underbrace{\sum_i \gamma_i I_i \cdot B}_{nuclear\ Zeeman} + \underbrace{\sum_i S \cdot P^e_{i,j} \cdot S_i}_{electron\ dipole-dipole}$$

The nuclear hyperfine term describes the dipole-dipole interaction of the central divacancy

spin S with other spin-carrying nuclear species with coupling strength determined by the hyperfine tensor A_i. In the case of the divacancy, I typically corresponds to the Pauli matrices $\{\sigma_x, \sigma_y, \sigma_z\}$ for spin-1/2 nuclei such as ^{13}C and ^{29}Si which respectively comprise approximately 1.1% and 4.7% of all nuclear species found in naturally abundant SiC. Hyperfine coupling with nearby nuclei will show up as a splitting in the ODMR spectra. A more detailed exploration of the hyperfine coupling of single divacancies to strongly and weakly coupled spins can be found in [23]. The nuclear dipole-dipole term describes coupling between nuclear species through the tensor $P^n_{i,j}$. The nuclear Zeeman term describes energy level splittings due to the external field, where γ_i is the nuclear gyromagnetic ratio. Finally, the electon dipole-dipole term describes couplings between the central spin to other electrons, impurities, and dopants in the system through the tensor $P^e_{i,j}$.

While the specifics of these additional terms in the Hamiltonian are beyond the scope of this thesis, special attention should be paid to the nuclear hyperfine interaction. Typically one third of all c-axis divacancies will have a nearby spin-carrying nuclear isotope (Fig. 2.5A), which will induce hyperfine energy splittings of several MHz within the $m_s = \pm 1$ sublevels (Fig. 2.5B) [23]. Thus, RF tones can be readily applied to induce entanglement and electron spin-conditional rotations of the nuclei (Fig. 2.5C) [23]. Due to their long coherence times, these nuclei act as *registers* that could act as critical memory components that store quantum information in future divacancy-based networks.

2.0.9 Formation energy

Not much attention has been given to the other defects in SiC that impact the divacancy's performance as a qubit. In reality, crystal growth, the presence of dopants, and irradiation process introduce other defect states, or "traps," within the SiC bandgap. The charge state dynamics of the defect ecosystem within SiC depends largely on factors such as dopant concentration and illumination energy, and will in turn impact the stability or prevalence of the various charge states of the divacancy.

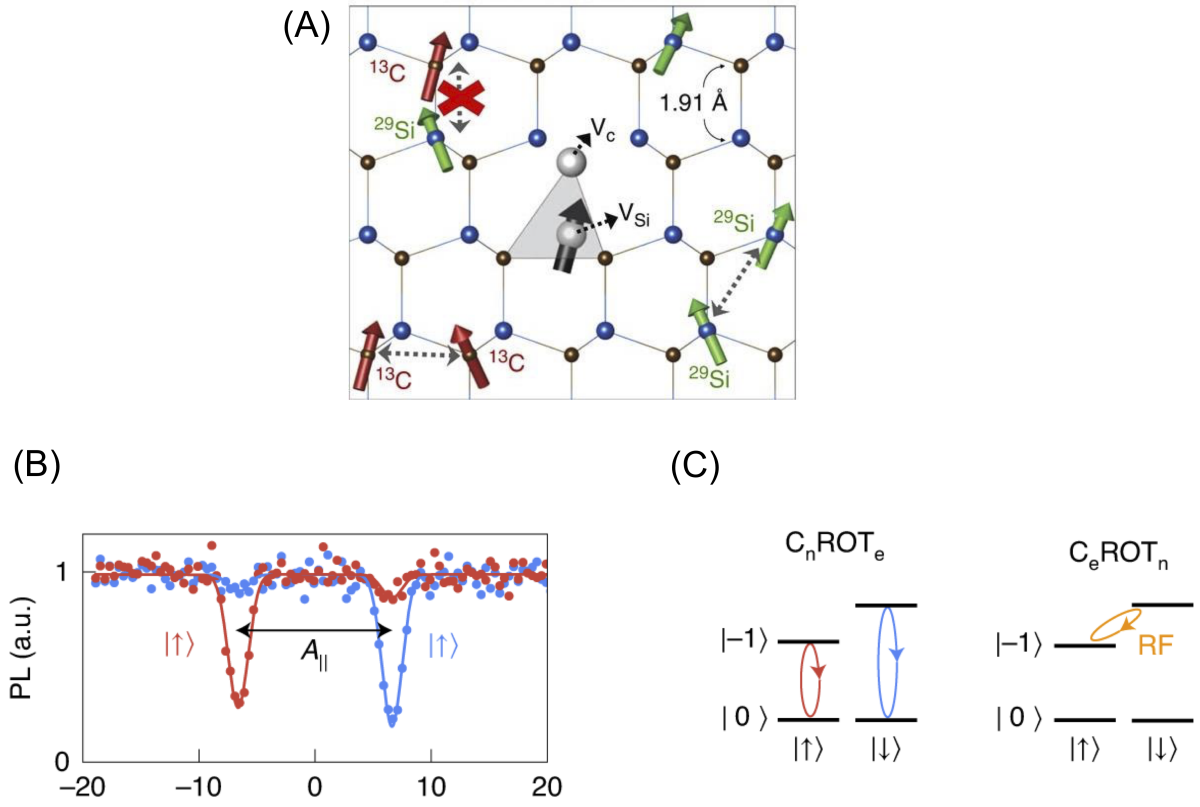

Figure 2.5: Spin I=1/2 nuclear registers. **(A)** Nearly one third of hh or kk divacancies will have a nearby ^{29}Si or ^{13}C. **(B)** These nuclei interact with the divacancy through hyperfine coupling, and induce energy level splittings that are seen in the ODMR spectra of the defect. The splitting goes as the strength of the parallel hyperfine coupling $A_{||}$, which is typically several MHz for strongly coupled nuclear spins. Here, $|\uparrow\rangle$ (red) and $|\downarrow\rangle$ (blue) are the nuclear spin states. **(C)** The electron spin-dependent hyperfine splitting allows rotations of the nuclei using RF frequencies (orange) only when the electron spin is in $|\pm 1\rangle$, enabling CNOT gates. Figures taken from [23] and [24].

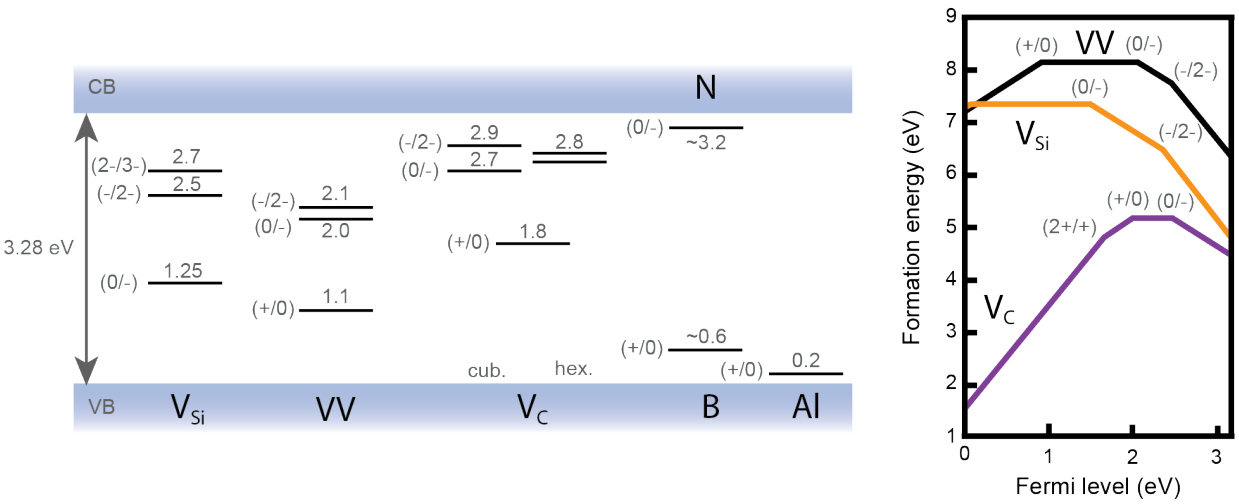

Figure 2.6: Charge transitions of defects in SiC. Charge transition levels are labelled in (A/B) format and indicate energy needed to add an electron to go from charge state A to charge state B. Energies are in eV and taken from distance from valence band. Figure on right displays formation energies for commonly found intrinsic defects in SiC. Figures adapted from [26] and [27].

The formation energy E^f of a defect is an important quantity that determines the stability of any one of its charge states for a given Fermi energy. The formation energy can be expressed [25]:

$$E^f[D^q] = E_{tot}[D^q] - E_{tot}[\text{bulk}] - \mu_D + q(\epsilon_F + \epsilon^{bulk}_{VBM} + \Delta V)$$

Here, the notation $E[A]$ refers to the total energy of a given DFT super cell A, D^q represents the defect in charge state q, μ_D is the chemical potential of the atomic constituents of the defect (and will be negative in the case of an atomic vacancy), ϵ_F is the Fermi energy referenced to the valence band minimum in the bulk crystal, and ΔV is the amount of energy needed to computationally align the bulk valence band minimum to the defect supercell $E_{tot}[D^q]$. Intuitively, this equation reveals how the formation energy is the energy difference between a defect complex and its constituent reference states, such as the energy of just the bulk crystal, chemical potential of just its atomic constituents, etc.

The formation energy is often plotted as a function of the Fermi energy of the material.

In these plots, the slope of the formation energy is equal to the charge state of the defect and the range over which the slope remains constant are the energies for which that particular charge state is stable. Hence, kinks in the formation energy curve signal a change in the favorable charge species. The energies at which these kinks occur are the defect charge transition levels (Fig. 2.6). Because the Fermi level of a semiconductor will depend on factors such as the dopant species and concentration, it is possible to engineer and tune the Fermi level to favor certain defect charge states. For example, because charge neutrality is favored at equilibrium, in intrinsic 4H-SiC the Fermi level is typically pinned so as to favor the neutral state of the carbon vacancy V_C, which is the most abundant defect in intrinsic SiC. However, at these Fermi levels, the divacancy can be either in its neutral or negative state. Thus, semi-insulating samples with a high density of carbon vacancies that pin the Fermi level closer to mid-gap, such as HPSI SiC, are preferable to ensure stability of VV^0[28].

2.0.10 Charge transitions of defects in the SiC bandgap

The most common defects found in SiC are the carbon vacancy (V_C) and the silicon vacancy (V_{Si}), but in doped material, shallow donor (N) and acceptor (B, Al) levels will form close to the conduction and valence band, respectively. In the case of heavy doping, the Fermi level will be pinned close to the shallow dopant levels, corresponding to a high prevalence of charge states closer to the band edges, such as VV^{2-} and VV^+ (Fig. 2.6), and a reduced stability of the neutral state VV^0. The the neutral divacancy undergoes a reduction in photoluminescence, or *quenching*, under optical illumination with energies $\leq$1.2 eV, especially when addressed with higher power resonant light ($\sim$1.1 eV). As the resonant laser power is increased, the defect is more likely to undergo two-photon ionization with the approximate 2.2 eV of combined energy from two resonant photons. This combined energy may efficiently drive the divacancy ($0 \rightarrow -$) transition at 2.0 eV, but may not have quite enough energy to induce a ($0 \rightarrow +$) transition, where $E_{0/+} = E_g - E_{(+/0)} = 3.28 - 1.1 = 2.18$ eV. For this reason, the "dark" state of the divacancy often observed when resonant excitation is used

is most likely the negative state VV^-. Additionally, the presence of shallow donors, such as nitrogen, which readily capture free charges results in a low divacancy recapture, meaning that divacancies "stuck" in VV^- are unlikely to reabsorb charges to return to VV^0.

Ionization and charge conversion of other defects in the SiC lattice under optical excitation frees up electrons or holes that can be reabsorbed by the divacancy complex, which in turn alters the prevalence of certain divacancy charge states. From an experimental perspective, while it may not always be possible to pin the Fermi level so as to favor VV^0, it is desirable to ensure stability of the neutral divacancy. This is because the various charge states of the divacancy have entirely different orbital and spin configurations, meaning spin information is not conserved when the charge state changes. Perhaps most notably, it has been experimentally confirmed that there is a revival in photoluminescence from the neutral divacancy upon illumination with a 705 nm (1.75 eV) laser [17]. This revival is associated with charge conversion from the "dark" state (VV^-) to the "bright" state (VV^0), where the revival in photoluminescence shows a clear resonance. The mechanism behind this charge resetting to the neutral state has two possible explanations. 1.75 eV is associated with the (+/0) transition of V_C, whereby the defect produces holes that are recaptured by the dark VV^- to form VV^0. An alternate explanation for the resonance around 705 nm may involve higher lying excited states of the negative divacancy that lie within the conduction band, which decay to the neutral divacancy state. Regardless of the mechanism responsible, due to the efficiency of the charge reset process, it has become routine to apply a 705 nm pulse at the beginning of experimental sequences to perform VV^0 initialization.

While entire areas of science are devoted to the study of defect charge states, as a general statement the presence of certain charge traps within a SiC sample will change the rate of free carrier generation and thus directly impact the rates at which the divacancy undergoes charge recapture. In turn, the charge stability, and therefore the charge lifetime, of the neutral divacancy complex is set by the trap concentration, dopant profile, and optical illumination energies. Thus, the material parameters of a SiC sample are crucial when

considering the demands on charge stability of the divacancy complex.

Chapter 3

Divacancy Characterization Techniques

In practice, all divacancy experiments begin with thorough characterization of the defect's optical and magnetic transitions via photoluminescence excitation (PLE), optically detected magnetic resonance (ODMR), and pulsed microwave Rabi measurements. These three measurements provide the three key parameters—the resonant transition frequency, microwave resonance, and π-pulse duration—needed to functionally operate a single divacancy qubit and are the building blocks needed to perform more complex experiments.

3.1 Photoluminescence excitation spectra (PLE)

PLE is the quintessential first experiment. It is a measurement of the optical absorption spectra of single divacancies, revealing the frequencies at which a divacancy will photoluminesce when illuminated and informing the experimentalist what laser frequencies to use for spin initialization and readout. To perform PLE, a narrow line, tunable laser is focused on a single divacancy and the laser frequency is swept while continuous (CW) mixing of the ground state spin sublevels is performed by applying microwaves via striplines patterend on the SiC surface, or wirebonds draped over the sample surface. Microwave mixing ensures

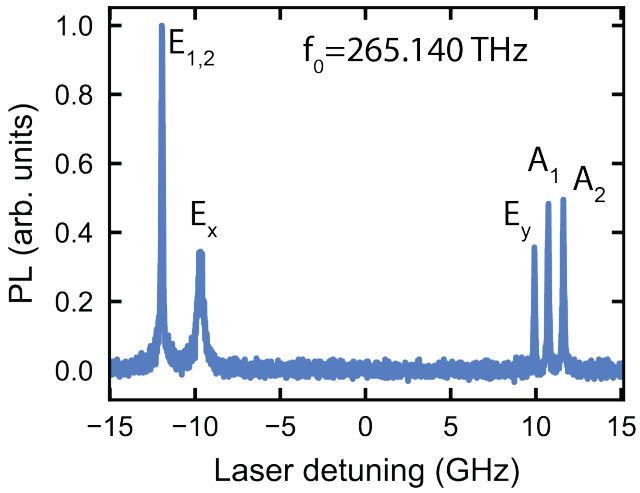

Figure 3.1: Photoluminescence excitation spectra (PLE) scan of single hh divacancy at T=5K. Five peaks are resolved, with E_1 and E_2 peaks overlapping in frequency (denoted $E_{1,2}$). Laser is detuned from central frequency f_0= 265.140 THz. Figure taken from [1].

that the defect does not become "trapped" in a particular spin sublevel and no longer photoluminesces even when the laser is tuned to one of the optical resonance frequencies. The PLE spectra of PL1 and PL2 divacancies typically displays six distinct resonances, split into two halves called the upper and lower branches (see Section 2.0.5) (Fig. 3.1). The lower branch consists of the E_1, E_2 and E_x transitions, in ascending frequency, while the upper branch consists of the E_y, A_1 and A_2 transitions, also in ascending frequency. Although the divacancy has six optical transitions, typically only five peaks are seen in the PLE spectra for c-axis divacancies because the E_1 and E_2 peaks often overlap in frequency. The frequency separation between the upper and lower branches is dictated by the transverse strain the defect is subject to, with typical low-strain divacancies exhibiting 10-15 GHz of separation between E_x and E_y. As strain increases, the separation between the branches widens and the transitions within each branch begin to mix (become closer in energy). Spin mixing in the excited state destroys the spin-selectivity needed for readout via the spin-photon interface, making high strain defects less desirable from an experimental perspective.

Because a PLE scan is often the first experiment performed on a single divacancy, the exact microwave transition frequencies between the $m_s = 0$ and $m_s = \pm 1$ sublevels are usu-

ally not well characterized at that point in the characterization process. For initial PL2 PLE scans, the zero-field splitting of PL2 divacancies (1.305 GHz) is typically used for microwave mixing. ODMR and additional rounds of PLE are then used to hone in on ideal powers and frequencies. The microwave power used in PLE scans can be fairly high, but care should be given so as not to heat the sample or cause the wirebonds to deteriorate. Excessively high microwave driving powers will cause mixing to occur too rapidly, rendering the PLE peaks invisible if the laser frequency is scanned too quickly such that the acquisition time is too short. The laser power used during PLE scans should also be moderated. Extremely high resonant laser powers (>mW) may cause ionization of the neutral divacancy VV^0, such that the defect goes "dark" and no longer photoluminesces. This shows up as a PLE scan with poorly defined resonances with non-Lorentzian shape due to the blinking that occurs as the defect ionizes. Extremely high laser powers will also generate high levels of photon scatter off the SiC surface, raising the background signal of the scan and reducing the visibility of the resonances. At moderately high powers, laser excitation generates charge carriers in the SiC that contribute to spectral diffusion of the PLE resonances, resulting in broadening and overlapping of the resonances. While this reduction in resolution is not desirable in most experiments, it is useful for increasing peak visibility in fast, broad scans to verify the existence of the upper and lower branches as well as the approximate strain splitting of a newly identified defect. Once approximate frequency ranges have been identified, the defect should be probed with low power excitation (microwatt to nanowatt range) in order to gain a clearly resolved scan of its individual optical resonances. However, the emitted PL signal is proportional to the excitation power and therefore excessively low laser powers may also reduce the visibility of the peaks.

PLE scans are used to screen single defects for particular criteria that make the defect a viable candidate for further experimentation. In particular, narrow optical linewidths are desirable because indistinguishable photon emission is required for quantum communication protocols. While previous studies have demonstrated close to lifetime-limited resonance

linewidths of 80 MHz in tunable SiC diode structures [17], the optical linewidth of a defect depends on the charge density of a particular SiC sample. A good figure of merit is to screen for defects with linewidths less than 250 MHz at operational laser powers. To identify the approximate optical linewidth and calibrate the power, the laser power of a PLE scan should be incrementally reduced until the linewidth of the resonances in the PLE scan cannot be narrowed further.

3.2 Optically detected magnetic resonance (ODMR)

Once a defect with well-separated, narrow optical resonances is identified, the magnetic resonance frequency is determined by continuously driving one of the optical transitions and sweeping the microwave drive frequency. This style of measurement with continuous microwave driving is often called continuous wave (CW) ODMR. A peak or dip in the collected photoluminescence will occur at the resonant microwave transition frequency, depending on the spin character of the optical transition being driven (Fig. 3.2). For example, optical pumping of any of the $m_s = \pm 1$ character optical transitions (E_1, E_2, A_1, A_2) will almost immediately initialize the defect into $m_s = 0$ due to preferential coupling via the spin-singlet intersystem crossing (Section 2.0.6). The defect remains trapped in $m_s = 0$, rendering it dark under laser excitation of the $m_s = \pm 1$ character optical transition frequency. When the resonant microwave frequency is applied, the defect is driven from $m_s = 0$ into $m_s = \pm 1$ so that it photoluminesces, resulting in a peak in the ODMR signal. Alternately, if the laser is tuned to one of the $m_s = 0$ character optical lines, the defect remains bright because of the high cyclicity of the transition. When the microwave frequency is at resonance, there will be a reduction or dip in the ODMR signal.

Typically, CW ODMR is performed by continuous driving of the $m_s = \pm 1$ character optical transitions because contrast is higher than when the $m_s = 0$ character optical transitions are pumped. In the presence of an externally applied static magnetic field (B_z),

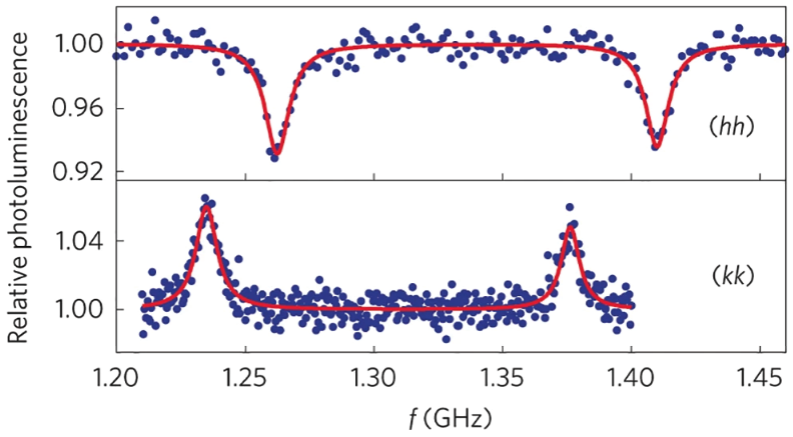

Figure 3.2: Optically detected magnetic resonance (ODMR) of hh and kk divacancies at T=20 K show resonant frequencies of $|0\rangle \leftrightarrow |+1\rangle$ and $|0\rangle \leftrightarrow |-1\rangle$ magnetic transitions. Here, a B=50 G field is applied to split the degeneracy of the $m_s = \pm 1$ spin sublevels. Figure taken from [8].

there will be two resonances in the ODMR spectra, corresponding to $|m_s = 0\rangle \leftrightarrow |m_s = +1\rangle$ and $|m_s = 0\rangle \leftrightarrow |m_s = -1\rangle$. The magnitude of the longitudinal field B_z can be determined by the splitting between the magnetic resonance frequencies for PL2 divacancies, where the splitting goes as $2\mu_B = 2 \times 5.78 * 10^{-5}$ eV/T = 27.95 GHz/T. The applied static field should be strong enough that the two ODMR resonances are well isolated to allow fully independent driving of each spin transition. ODMR calibration to find the requires adjustment of the microwave and optical powers. For CW microwave driving, the microwave power should be lowered until the linewidth of the ODMR resonance is narrower than 15 MHz to allow for accurate identification of the central resonance frequency. The resonant laser power should also be considerably lowered during ODMR to limit optical linewidth broadening that causes spin mixing. Once the resonant spin transition frequencies are identified with ODMR, CW PLE and CW ODMR experiments are iterated to correctly calibrate the resonant optical and microwave powers.

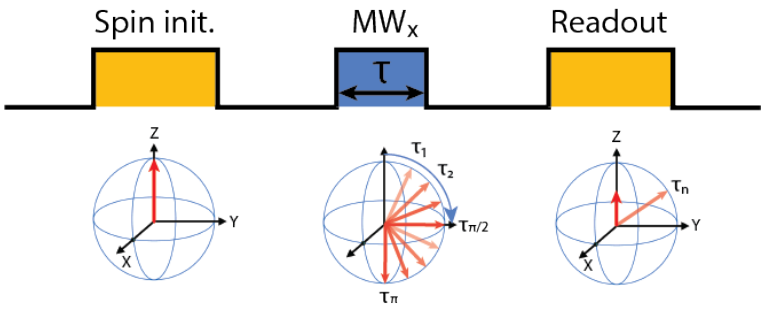

Figure 3.3: Tyical Rabi microwave measurement sequence. The square microwave pulse duration τ is swept to perform rotations $\mathrm{Rot}_x(\theta(\tau))$ about the Bloch sphere.

3.3 Pulsed Rabi measurements

After identification of the optical and microwave resonance frequencies with CW measurements, pulsed measurements are used to further calibrate the frequencies, powers, and excitation duration needed for full qubit control. In contrast to CW measurements, pulsed experiments allow for sequential excitation of specific processes so that logic gates can be performed on the qubit.

Rabi oscillations describe cyclic driving of a quantum two level system between its two states. In the case of the divacancy, pulsed Rabi experiments are used to identify the correct microwave frequency, power, and pulse duration required to transfer a qubit between $m_s = 0$ and either $m_s = +1$ or $m_s = -1$. Full transfer between the qubit basis states is called a π pulse because the effect of the microwave pulse is a 180° rotation about the Bloch sphere. IQ modulation of the delivered microwaves determines the axis of rotation imparted by the pulses. Typically the "I" component of the pulse is used for rotation about the x-axis of the Bloch sphere, while the "Q" component of the pulse is 90° out of phase with "I" and generates rotation about the y-axis. The axis of rotation of a pulse is often denoted by the subscript, such as π_x or π_y.

A typical Rabi sequence using $m_s = 0$ and $m_s = +1$ as the qubit basis is shown in Fig. 3.3. After initialization to $m_s = 0$, a microwave pulse of variable duration is applied to the defect and the spin state is optically read out. Assuming readout it performed by pumping a

$m_s = 0$ character optical transition, the PL signal will sinusoidally decrease with increasing microwave pulse duration until the qubit is fully transfered to $m_s = +1$, corresponding to a π rotation (Fig. 3.4). The PL signal at this minima should be as close as possible to the background count rate, indicating that the defect is not emitting PL and has been fully transferred to the dark state. A high level of PL above the background at the Rabi minima may indicate the following:

- Poor initialization of the defect into $m_s = 0$. Imcomplete initialization generates the state $\alpha\,|0\rangle + \beta\,|+1\rangle$, where $\beta \neq 0$, resulting in a spin state with some $|0\rangle$ component even after π rotation. In this case, either the laser initialization pulse duration or power should be increased, or the initialization laser frequency should be calibrated.

- Incorrect microwave frequency. The spectral bandwidth of a pulse is determined by its Fourier transform, which for a square pulse is a sinc function. Thus, even pulses that are detuned from the true magnetic resonance frequency may weakly drive spin transitions if they are strong enough. During a Rabi experiment, weak driving due to detuning shows up as incomplete transfer of population to the dark spin state, resulting in photoluminescence even when a π pulse is applied. To calibrate the microwave frequency, pulsed ODMR should be performed using a microwave pulse duration corresponding to the Rabi signal minima ($\tau = \pi$).

- Excessively long and low power microwave pulse duration. As previously mentioned, the spectral purity of a square pulse increases as its temporal duration gets longer. If the microwave pulse is only slightly detuned but excessively long and low power, the pulse may not have resonant frequency components that are at a high enough power. Instead, higher powers should be used to construct π pulses that correspond to a spectral bandwidth around the microwave carrier frequency that is wide enough to address frequencies within a FWHM of the ODMR resonance. The effects of Rabi oscillations can be understood through the rotating wave approximation. At extremely

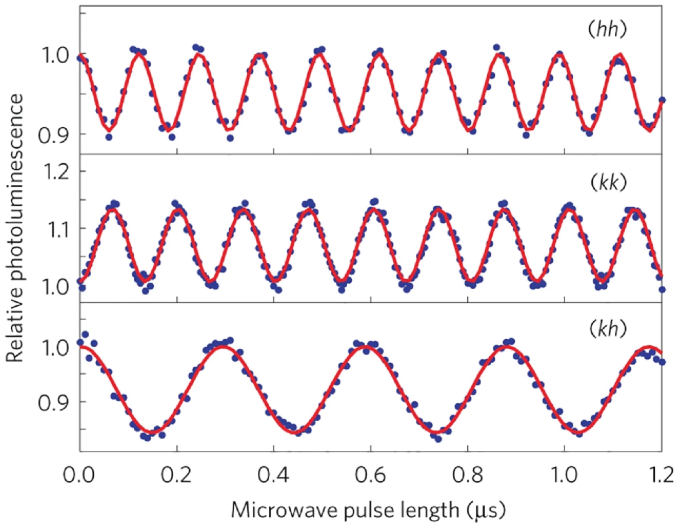

Figure 3.4: Rabi oscillations of hh, kk, and kh divacancies at T=20 K demonstrate coherent control of single spin defects. The signal minima and maxima correspond to full state transfer to one of the basis states. Intermediate points indicate the defect has been prepared to a superposition. Figure taken from [8].

high powers, this approximation breaks down, and population transfer is no longer purely sinusoidal [29].

Additionally, if the minima in the Rabi signal is significantly higher than the background noise of the SNSPD, the power of the readout power may be so high that laser scatter off the sample surface reaches the detector. In this case, the readout power should be lowered.

3.3.1 Differential measurements

It is often helpful to perform differential measurements, which contain two phases. In one phase, an experiment is performed for a defect initialized to $m_s = 0$. This is directly followed by the second phase, where the same experiment is performed after the defect is initialized to $m_s = +1$ or $m_s = -1$. These differential measurements are colloquially referred to as "pi-no-pi" experiments. Variations in the contrast in signal from differential sequences help to diagnose sources of error, such as initialization infidelity.

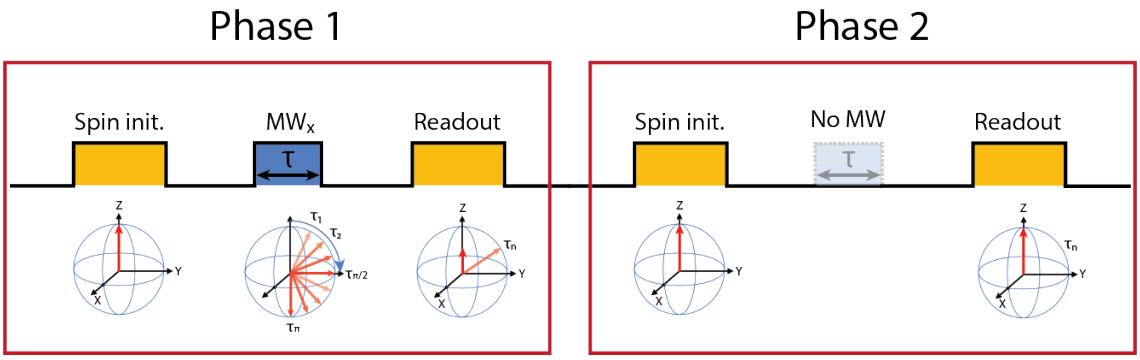

Figure 3.5: Typical differential Rabi measurement sequence. All differential measurements are divided into two consecutive phases, Phase 1 and Phase 2. Phase 1 typically involves microwave manipulation of the defect after preparation to $m_s = 0$, while Phase 2 involves no microwave manipulation of the defect. Phase 1 and Phase 2 must be the same duration in order to meaningfully compare counts per second measured during each phase. Similarly, when sweeping a parameter such as the microwave pulse duration τ during a differential sequence, the combined duration of Phase 1 and Phase 2 for a particular value τ_1 must be the same as the combined duration of Phase 1 and Phase 2 for another value τ_n in order to meaningfully compare the measurements.

A typical differential Rabi sequence is shown in Fig. 3.5. Ideally, the signal from Phase 2 of the experiment shown in Fig. 3.5 should not change as the duration τ of the microwave pulse in Phase 1 is swept. However, if initialization is poor, the defect will have some $m_s = +1$ component. The compounding effect of transferring more of the population to $m_s = +1$ during the preceding sequence causes the defect to become gradually darker upon readout. This manifests as sinusoidal variations in the signal from Phase 2 (Fig. 3.6) and can be ameliorated through application of a longer initialization laser pulse.

The endgame of differential experiments should be to achieve the highest possible contrast C between spin states. If using the sequence outlined in Fig. 3.5, maximum contrast should be achieved at the point of full transfer of the population to the dark state ($m_s = +1$) via a π pulse:

$$C = \frac{PL_{\text{No }\pi} - PL_{\pi}}{PL_{\text{No }\pi}}$$

Where PL is the photoluminescence signal associated with the qubit spin states. Once an initial π pulse calibration is performed, it is common to repeat PLE and ODMR experiments

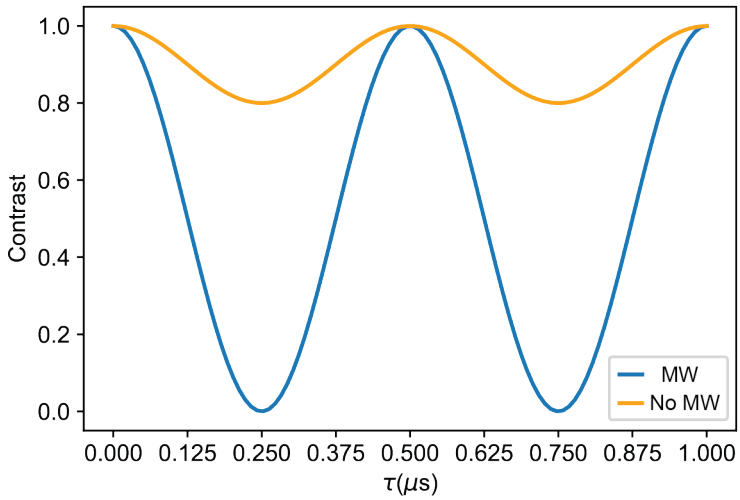

Figure 3.6: Poor spin initialization during Rabi results in low contrast at signal minima and presents as sinusoidal variation in signal from Phase 2 of experiment outlined in Fig. 3.5, corresponding to states that do not undergo microwave manipulation ("No MW").

in their pulsed format to ensure that all pulse powers, durations, and frequencies are tuned to provide maximum contrast.

3.4 Figures of merit

Despite the ability manipulate the divacancy spin state, no qubit is perfect and logical operations cannot be repeated indefinitely after spin initialization. Eventually, information is lost due to interaction of the qubit with its environment. Broadly, any loss is explained by either longitudinal or transverse coupling with the defect environment. Transverse interactions couple to the σ_x degree of freedom of a qubit, where $\langle 0| \sigma_x |1\rangle \neq 0$, while longitudinal interactions couple to the σ_z degree of freedom of a qubit, where $\langle +| \sigma_z |-\rangle \neq 0$ [30]. The timescales associated with the longitudinal and transverse coupling of a qubit to its environment are often used as figures of merit that describe how practically viable a particular qubit is. Entire PhDs have been spent mitigating the longitudinal or transverse coupling of a qubit or to remove the sources of these interactions entirely in order to preserve qubit states for longer.

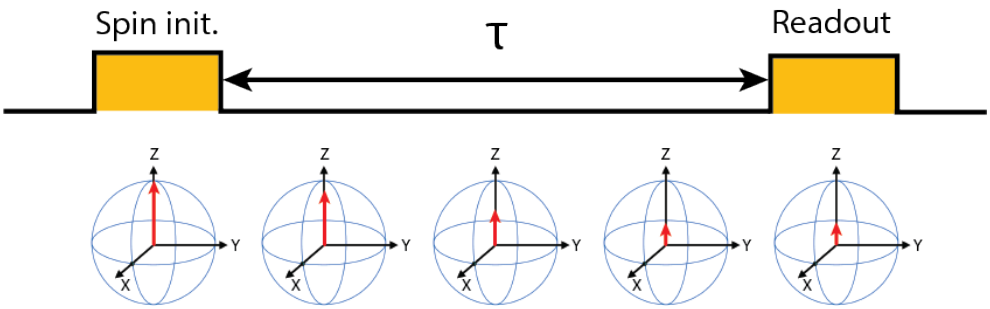

Figure 3.7: T_1 measurement sequence. The qubit is prepared into $m_s = 0$ and allowed to relax for duration τ. A differential measurement may be performed where the defect is rotated to $m_s = \pm 1$ via a π_x rotation, after which it is allowed to relax. The signal decays as e^{-t/T_1}

3.4.1 T_1 relaxation time

The spin T_1 describes the timescale it takes for a polarized spin to exponentially decay back into a thermal mixture of the ground state spin sublevels. Practically speaking, T_1 can be thought of as the spin flip lifetime in the ground state. Geometrically speaking, T_1 can be thought of as the shortening of a vector terminating on the surface of the Bloch as it recesses into the center. In the bulk SiC samples we study, T_1 is typically limited by longitudinal spin-lattice relaxation caused by phononic modulation in the spin-spin coupling between electrons in the defect [31]. As the inter-electron displacement changes due to vibrations in the lattice, the spin-spin interaction may be enhanced and a spin flip may occur. This is suppressed at low temperatures, resulting in demonstrations of T_1 times of up to 8 hours for the NV^- center in diamond [31, 32]. However, at low temperatures when phonons are "frozen out," other processes that contribute to T_1 decay become apparent. For example, T_1 decay may occur due to cross relaxation due to dipole-dipole interactions between single defects and other spin species, which is dependent on magnetic fields and impurity concentrations [33]. Other sources of T_1 decay include magnetic noise due to spin-carriers at the sample surface. A typical T_1 measurement sequence is shown in Fig. 3.7, where the T_1 time is equal to the characteristic timescale of the exponential decay in collected photoluminescence as τ is swept.

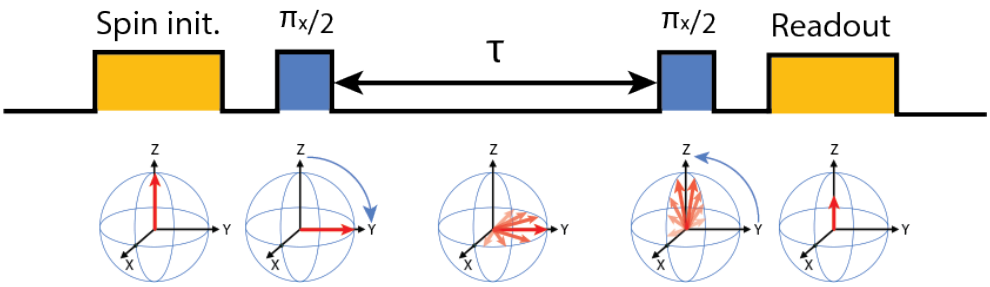

Figure 3.8: T_2^* measurement sequence. The qubit is prepared into a superposition on the equator of the Bloch sphere, after which it is allowed to decohere for duration τ. The spin is then rotated back onto the North pole of the Bloch sphere and is read out optically. A differential measurement may be performed where the defect is rotated to $m_s = \pm 1$ via a π_x rotation after optical spin initialization to $m_s = 0$.The signal decays as e^{-t/T_2^*}

3.4.2 T_2^* dephasing time

T_2^* is the spin dephasing time and describes the timescale over which the phase information contained in a quantum superposition is maintained. From a geometric perspective, dephasing can be thought of as the spreading or fanning of a vector prepared in a superposition state around the equator of the Bloch sphere due to transverse coupling with the environment (Fig. 3.8). In contrast to the T_2 coherence time (discussed later), T_2^* is an observed or effective quantity that includes the effects of decoherence from coupling to nearby paramagnetic nuclear spins [24, 34, 35] and magnetic and electric noise from unpaired electron spins in dangling bonds at the surface [36, 37].

T_2^* is often measured via Ramsey interferometry, whereby the magnetic drive (ω) is detuned from the qubit transition frequency (ω_q) such that $\Delta = \omega_q - \omega$. The Hamiltonian of the qubit subject to a time-varying magnetic field can be divided into constant and time varying parts:

$$\hat{H} = \frac{\omega_q}{2}\sigma_{11} - \frac{\omega_q}{2}\sigma_{00} + \Omega cos(\omega t + \phi)[\sigma_{10} + \sigma_{01}]$$

where $\sigma_{ij} = |i\rangle \langle j|$ and we have dropped the usual factor of $\hbar$ for convenience. Using the

definition $\Delta = \omega_q - \omega$, the Hamiltonian is rewritten:

$$\hat{H} = \hat{H_0} + \hat{H_V}$$

$$\hat{H_0} = \frac{\omega}{2}\sigma_{11} - \frac{\omega}{2}\sigma_{00}$$

$$\hat{H_V} = \frac{\Delta}{2}\sigma_{11} - \frac{\Delta}{2}\sigma_{00} + \Omega cos(\omega t + \phi)[\sigma_{10} + \sigma_{01}]$$

The rotating wave approximation is applied to the time varying part of the Hamiltonian:

$$\hat{H_I} = e^{i\hat{H_0}t}\hat{H_V}e^{-i\hat{H_0}t}$$

Using the definition $e^{(ia(\hat{n}\cdot\vec{\sigma})} = Icos(a) + i(\hat{n}\cdot\vec{\sigma})sin(a)$, the matrix form of $e^{\pm i\hat{H_0}t}$ is written:

$$e^{\pm i\hat{H_0}t} = e^{\mp\frac{i\omega t}{2}\sigma_z} = Icos(\frac{\omega t}{2}) \mp i\sigma_z sin(\frac{\omega t}{2})$$

$$= \begin{pmatrix} e^{\mp\frac{i\omega t}{2}} & 0 \\ 0 & e^{\pm\frac{i\omega t}{2}} \end{pmatrix}$$

Applying this transformation to the matrix form of $\hat{H_V}$:

$$e^{i\hat{H_0}t}\hat{H_V}e^{-i\hat{H_0}t} = \begin{pmatrix} e^{-\frac{i\omega t}{2}} & 0 \\ 0 & e^{\frac{i\omega t}{2}} \end{pmatrix} \begin{pmatrix} -\frac{\Delta}{2} & \Omega cos(\omega t + \phi) \\ \Omega cos(\omega t + \phi) & \frac{\Delta}{2} \end{pmatrix} \begin{pmatrix} e^{\frac{i\omega t}{2}} & 0 \\ 0 & e^{-\frac{i\omega t}{2}} \end{pmatrix}$$

$$= \begin{pmatrix} -\frac{\Delta}{2} & e^{-i\omega t}\frac{\Omega}{2}cos(\omega t + \phi) \\ e^{i\omega t}\frac{\Omega}{2}cos(\omega t + \phi) & \frac{\Delta}{2} \end{pmatrix}$$

$$= \begin{pmatrix} -\frac{\Delta}{2} & \frac{\Omega}{2}[e^{-i(2\omega t+\phi)} + e^{i\phi}] \\ \frac{\Omega}{2}[e^{i(2\omega t+\phi)} + e^{-i\phi}] & \frac{\Delta}{2} \end{pmatrix}$$

A critical assumption made in the rotating wave approximation is that the rapidly varying components ($e^{\pm i(2\omega t+\phi)}$) average out, and we are left with:

$$\hat{H_I} = \begin{pmatrix} -\frac{\Delta}{2} & \frac{\Omega}{2}e^{i\phi} \\ \frac{\Omega}{2}e^{-i\phi} & \frac{\Delta}{2} \end{pmatrix}$$

The eigenstates and eigenenergies of $\hat{H_I}$ are:

$$\lambda_1 = +\frac{\sqrt{\Omega^2+\Delta^2}}{2}, \;\; |v_1\rangle = \begin{pmatrix} cos(\theta/2) \\ -e^{-i\phi}sin(\theta/2) \end{pmatrix}$$

$$\lambda_2 = -\frac{\sqrt{\Omega^2+\Delta^2}}{2}, \;\; |v_2\rangle = \begin{pmatrix} sin(\theta/2) \\ e^{-i\phi}cos(\theta/2) \end{pmatrix}$$

Where $tan(\theta) = \Omega/\Delta$. When the qubit is interacting with the magnetic drive, it undergoes time evolution:

$$e^{-i\hat{H_I}t}$$

The Taylor expension of this time evolution is:

$$e^{-i\hat{H_I}t} = 1 - i\hat{H}t + \frac{1}{2!}(-i\hat{H}t)^2 + ...$$

And thus operating on an eigenstate of $\hat{H}$ with the operator $e^{-i\hat{H_I}t}$ results in:

$$e^{-i\hat{H_I}t}\,|v_i\rangle = [1 - i\hat{H}t + \frac{1}{2!}(-i\hat{H}t)^2 + ...]\,|v_i\rangle$$

$$= [1 - i\lambda_i t + \frac{1}{2!}(-i\lambda_i t)^2 + ...]\,|v_i\rangle$$

$$= e^{-i\lambda_i t}\,|v_i\rangle$$

The states $|0\rangle$ can be expressed as a linear combination of the eigenstates of $\hat{H}$:

$$|0\rangle = \begin{pmatrix} 1 \\ 0 \end{pmatrix} = cos(\frac{\theta}{2}) |v_1\rangle + sin(\frac{\theta}{2}) |v_2\rangle$$

The probability $P_0(t)$ to find the qubit in state $|0\rangle$ after some time T is:

$$P_0(t) = |\langle 0| e^{-i\hat{H}_I T} |0\rangle|^2$$

$$= \left| \begin{pmatrix} cos(\frac{\theta}{2}) & sin(\frac{\theta}{2}) \end{pmatrix} \begin{pmatrix} e^{i\tilde{\Omega}t/2} cos(\frac{\theta}{2}) \\ e^{-i\tilde{\Omega}t/2} sin(\frac{\theta}{2}) \end{pmatrix} \right|^2$$

$$= \frac{1}{2}(1 + cos(\tilde{\Omega}t)) + \frac{cos^2(\theta)}{2}(1 - cos(\tilde{\Omega}t))$$

$$= \frac{1}{2}[1 + cos(\sqrt{\Omega^2 + \Delta^2}t)] + \frac{cos^2(\theta)}{2}[1 - cos(\sqrt{\Omega^2 + \Delta^2}t)]$$

The probability $P_1(t)$ to find the qubit in state $|1\rangle$ is $P_1(t) = 1 - P_0(t)$:

$$P_1(t) = 1 - \frac{1}{2}(1 + cos(\tilde{\Omega}t)) - \frac{cos^2(\theta)}{2}(1 - cos(\tilde{\Omega}t))$$

$$= sin^2(\theta) sin^2(\frac{\tilde{\Omega}t}{2})$$

A $\pi/2$ pulse corresponds to an interaction duration that creates an equal superposition of both qubit states such that $P_0(T_{\pi/2}) = P_1(T_{\pi/2}) = 1/2$. Solving for $T_{\pi/2}$:

$$T_{\pi/2} = \frac{2}{\sqrt{\Omega^2 + \Delta^2}} sin^{-1}[\frac{\sqrt{\Omega^2 + \Delta^2}}{\Omega\sqrt{2}}]$$

From here, the Ramsey sequence $\hat{U}_R$ can be modeled as a rotation $R_0(T_{\pi/2})$, whereby the qubit interacts with the magnetic drive for duration $T_{\pi/2}$, followed by a free evolution $F(\tau)$, once again followed by a rotation $R_0(T_{\pi/2})$:

$$\hat{U}_R = R_0(T_{\pi/2})F(\tau)R_0(T_{\pi/2})$$

The rotation $R_0(T_{\pi/2})$ is described by time evolution whereby the qubit is subject to the interaction Hamiltonian $\hat{H}_I$. If we assume that the phase ϕ of the oscillating magnetic field is zero ($\phi = 0$), the matrix $\hat{H}_I$ can be written:

$$\hat{H}_I = \begin{pmatrix} -\frac{\Delta}{2} & \frac{\Omega}{2} \\ \frac{\Omega}{2} & \frac{\Delta}{2} \end{pmatrix} = -\frac{\Delta}{2}\sigma_z + \frac{\Omega}{2}\sigma_x$$

And therefore the rotation can be written:

$$R_0(T_{\pi/2}) = e^{-i\hat{H}_I t} = e^{-i(-\frac{\Delta}{2}\sigma_z + \frac{\Omega}{2}\sigma_x)T_{\pi/2}}$$

$$= \begin{pmatrix} cos(\frac{T}{2}) + i\Delta sin(\frac{T}{2}) & -i\Omega sin(\frac{T}{2}) \\ -i\Omega sin(\frac{T}{2}) & cos(\frac{T}{2}) - i\Delta sin(\frac{T}{2}) \end{pmatrix}$$

We perform the renormalization $T \to \tilde{\Omega}T$ and $\Delta, \Omega \to \Delta/\tilde{\Omega}, \Omega/\tilde{\Omega}$ (which will be useful later when simplifying terms). Once the qubit has undergone the first rotation, the microwave drive is turned off such that the Hamiltonian takes the form $\hat{H} = \frac{\Delta}{2}\sigma_z$ (we are still operating within a frame rotating at frequency ω such that the qubit splitting is Δ). The qubit is allowed to precess for duration τ, where the free evolution $F(\tau)$ is expressed:

$$F(\tau) = e^{-i\Delta\sigma_z\tau/2} = cos(\frac{\Delta}{2}\tau)\mathbb{1} + i\sigma_z sin(\frac{\Delta}{2}\tau) = \begin{pmatrix} e^{i\Delta\tau/2} & 0 \\ 0 & e^{-i\Delta\tau/2} \end{pmatrix}$$

The full matrix representation of the Ramsey sequence is $U = R_0(T_{\pi/2})F(\tau)R_0(T_{\pi/2})$, and the probability of finding the qubit in $|1\rangle$ is:

$$P_1 = |\langle 1|\, U\, |0\rangle|^2 = |U_{12}|^2 = \left| -i\frac{\Omega}{\tilde{\Omega}}[sin(\tilde{\Omega T})cos(\Delta\tau/2) - 2\frac{\Delta}{\tilde{\Omega}}sin^2(\frac{\tilde{\Omega T}}{2})sin(\Delta\tau/2)] \right|^2$$

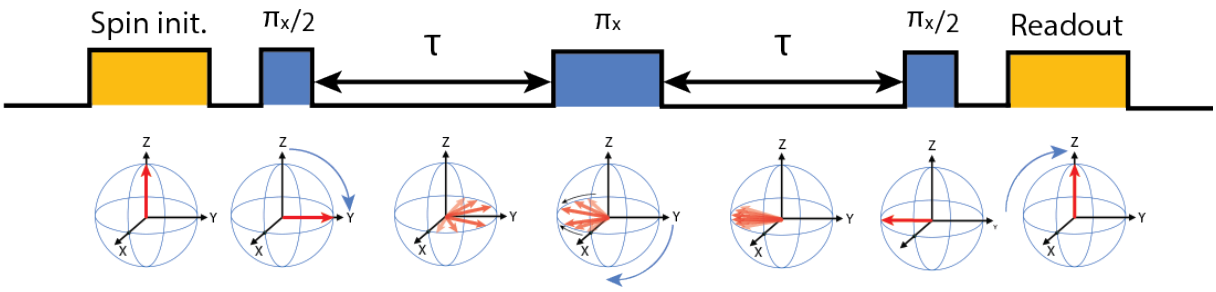

Figure 3.9: T_2 Hahn echo sequence. The qubit is prepared into a superposition on the equator of the Bloch sphere, after which it is allowed to decohere for duration τ. The qubit is then rotated with a π_x pulse, such that the effects of rapidly fluctuating decoherence sources catch up to the effects of slowly fluctuating decoherence sources, resulting in a refocusing or revival of the coherence, called the spin echo. A differential measurement may be performed where the refocusing pulse π_x is not performed.

Making the substitution $sin(\chi) = \Delta/\Omega$, the transition probability is written:

$$|U_{12}|^2 = |-i(cos(\chi)cos(\Delta\tau/2) - sin(\chi)sin(\Delta\tau/2)|^2 = |-icos(\chi + \Delta\tau/2)|^2 = cos^2(\chi+\Delta\tau/2)$$

While this expression returns an oscillatory signal that continues ad infinitum with free precession time (τ), in real life Ramsey experiments result in an oscillating signal with a decaying envelope. This decay comes from a distribution of detunings Δ due to the fluctuating magnetic environment of the qubit. In the context of the divacancy in SiC, this change in detuning is caused primarily by flip-flops between spin-1/2 nuclear species such as ^{13}C and ^{29}Si, which changes the effective field experienced by the defect. A full derivation of this exponential envelope is discussed in Ref. [38].

3.4.3 T_2 coherence time

T_2 is the spin coherence time and is one of the most important metrics of performance because it sets a limit on the number of logical gate operations that a qubit can undergo before information is lost. T_2 can be thought of as T_2^* dephasing with a filter function applied to cancel certain parts of the noise spectral density. To experimentally distinguish T_2 from T_2^*, a microwave refocusing pulse is applied after the qubit is placed in a superposition,

cancelling the effect of phase accumulation due to static inhomogeneities in the magnetic field. This inhomogeneity can be thought of as a source of σ_z dephasing, and the refocusing pulse is equivalent to a rotation about the x-axis of the Bloch sphere. Application of a single refocusing pulse is called a Hahn echo sequence and is pictured in Fig. 3.9. While a Hahn echo sequence uses a single pulse to undo dephasing from uni-axial (σ_z) quasistatic noise sources, multiple refocusing pulses can be used to further protect qubits from different types of errors. These dynamical decoupling sequences employ combinations of refocusing rotations about the Bloch sphere to address higher frequency of multi-axial noise sources. For example, the Carr-Purcell-Meiboom–Gill (CPMG-N) sequence, pictured in 6.8, consists of an even number of π_x rotations, where increasing the order (N) of the sequence protects against higher and higher frequency noise components. Other dynamical decoupling sequences such as XY4-N and XY8-N employ multi-axis rotations and are effective at undoing pulse calibration errors. In other words, different dynamical decoupling pulses effectively apply a different filter function to the spectral density of the environmental noise. While dynamical decoupling may extend the coherence time of a qubit in practice, the coherence time is ultimately limited by the relation $T_2 \leq 2T_1$. This relationship can be derived by writing the evolution of the density matrix for a single spin subject to an amplitude-damping channel [39].

Chapter 4

Experimental Apparatus for Divacancy Characterization

In this section we will discuss that experimental apparatus that allow us to physically work with VV^0. A large part of my PhD was spent designing and building a setup to characterize single divacancies. This section is aimed at walking any individual through how such a setup is built from scratch.

4.1 Confocal microscopy

Confocal microscopy is a technique used to generate an image at a particular focal plane. All images are created by collecting photons reflected off of or emanating from an object of interest. For the setups used in our research labs, the collected photons are typically either reflected photons from a focused laser scattering off of a physical feature or are emitted from a defect (photoluminescence). The captured photons allow an image to be generated. In the case of our confocal microscopes, the image size is exactly equal to the beam waist (several microns wide) of the focused laser spot used to probe the sample. Practically speaking, a single snapshot that is the size of the beam waist is not helpful if one is trying to create the image of a more macroscopic landscape. For example, one may want to generate a 100

μm square image to see what the divacancy density of a chip of SiC looks like. To do this, scanning confocal microscopy is employed, where implements such as a piezoelectric stages or micrometers turned by a mechanical motor raster the laser across the sample. Images are recorded at discrete intervals and stitched together to generate a larger picture of the surface.

Scanning confocal microscopy is used to measure a host of different systems, but the technique is commonly employed in biology settings where samples are stained with fluorescent protein markers and the photons emitted by those markers upon laser excitation are steered to an external detector. In the biological sciences, these kinds of microscope setups are sold as modular, bench-top units. For optical measurement of the spin defects, life is not so sweet. The demands of accommodating unique combinations of optical excitation and emission wavelengths means most researchers must build their own confocal setups. While the specifics of each confocal setup used to characterize divacancies in SiC, or the NV^- in diamond, or what have you, will be different, all confocal setups will include the following elements:

- **A laser:** to excite the optical transitions of the defect under study. More lasers may be added for uses such as charge initialization of the defect, or to allow more than one optical transition to be probed at a time.

- **A photodetector:** to detect photoluminescence from the optically-active defect. Photodetectors such as Si APDs from Hamamatsu are commonly employed in NV^- setups because the NV^- photoluminesces in the visible regime. When *single* photon sensitivity is required, superconducting nanowire single photon detectors (SNSPDs) are used.

- **An objective:** Objectives are a compact, packaged collection of lenses responsible for focusing a collimated laser onto the defect and re-collimating the emitted photoluminescence back to the rest of the optical elements so it can be spectrally picked off and

detected.

- **Mirrors, lenses, filters, fibers:** Laser photons must make it to the defect somehow. Lenses are used to collimate laser light so that it travels through space without diffusing. Mirrors steer collimated laser light onto the back of the objective so that it may be focused down onto the sample. Filters are used to spectrally separate laser photons from emitted photoluminescence. Selection of a good filter is critical for separating photoluminescence from the excitation path and sending it towards down the collection path to the photodetector. Fibers may also be employed instead of free space optics as a low-loss way to shuttle photons between remote locations, but this method requires fiber-coupling and fiber-compatible equipment.

Designing and building a confocal microscope is a tedious process not only because it requires physical labor, but because selecting the correct components can be daunting. In the lab, we often use components purchased from Thorlabs. As such, navigating the product information page and data sheets on the Thorlabs website is an essential skill. For optical components, always take note of the available anti-reflection coatings, the transmission and reflection plots (not just for normal transmission, but at different angles and for different polarizations of light), the maximum power ratings, and the size of the component (space considerations and effective working areas may make your life easier or harder).

The design of a confocal microscope will depend on the demands of the experiment. For example, for a researcher interested in maximizing their collection efficiency, it is important to have an extremely high NA objective and to reduce the number of lossy free-space components the photoluminescence interacts with by putting the collection path as close to the sample as possible. If the goal is to have five different lasers in the setup that must all somehow reach the sample, one must find creative ways to spatially combine the individual laser paths together using dichroic mirrors to allow all those lasers to reach the sample, while also ensuring that photoluminescence can be spectrally separated and sent to a detector. For the

remainder of the this section, we will operate under the assumption that a high collection efficiency of photoluminescence from the divacancy is desirable.

4.1.1 Selecting a microscope objective

Microscope objectives are a packaged series of lenses that focus light onto the sample. The internal workings of an objective are often mysterious, but the demands of the confocal setup will determine the main specifications to look for:

- **Working distance** The working distance of an objective is a measure of how far away from the objective light gets focused. If an objective needs to be mounted outside of a cryostat, a long working distance is desirable because of the vacuum window glass that comes between the sample and the objective. For setups where the objective is mounted inside the cryostat, the need for a long working distance is minimal because the objective can be brought into very close proximity of the sample.

- **Numerical aperture (NA)** The NA measures the angle of the effective cone of light emanating from a sample that an objective can collect and collimate. The NA is defined as NA$= n * \sin(\theta)$ where n is the index of refraction of the propagation media and θ is the half angle of the cone of light that enters the objective. An objective with a higher NA is more desirable because a larger cone of light can be collected. It is possible to find off-the-shelf objectives specified for the near-IR with NA=0.8, but higher NA objectives can be customized to order ($$$).

- **Transmission data** Transmission and reflectance of the objective at different wavelengths is a crucial factor which doesn't require too much more discussion.

- **Coverglass correction** Many objectives are sold for biological science research, where coverglass slips are placed over the sample. The coverglass between the objective and the sample creates a slight change in the index of refraction as well as spherical

aberrations. Thus, many objectives come with either a correction collar that is rotated to maximize signal, or an immobile (fixed) coverslip correction specified for a particular thickness of glass.

4.1.2 Selecting a laser

Resonant excitation of divacancies with a narrow linewidth lasers ensure that optical linewidth measurements of defects are not laser-limited, and is necessary to ensure that only a single optical transition is addressed at a time. Tunable lasers are used to resonantly excite transitions, but tend to be much more expensive and finicky. Lasers come in a variety of packagings. The most basic laser component that can be purchased from Thorlabs is an individual laser diode. However, these are standalone units that are neither pre-collimated nor fiber-coupled and are not very practical for integrating into a setup. The more convenient form of laser is fiber-coupled, meaning that its output is routed into an optical fiber and the end of that fiber can be plugged into a host of other fiber-compatible optical elements such as collimation packages.

4.1.3 Laser collimation

Assuming the laser is fiber coupled, the next step is to collimate it such that it propagates without spreading. Fiber collimators are readily available on Thorlabs, Newport, and other lab supplies companies and are fundamentally just a lens in a metal packaging with a slot to plug in a fiber. To pick the correct collimation package, identify a package that is specified for the wavelength of your laser. Typically this means that the glass used in the package is coated to mitigate reflections and therefore improve transmission at the wavelength of interest. For example, for divacancy characterization, typically Thorlabs C-coated products are desirable as they have been optimized for transmission between 750 nm and 1150 nm, which should encompass the full range of wavelengths needed for divacancy characterization. Fixed collimation packages have a set distance between the fiber and the lens, and therefore

do not require adjustment by the user. While these fixed packages are "plug-and-play," and require little to no adjustment, they do have the downside that the output beam diameter cannot be changed.

To select a collimation package, first determine what size beam diameter you need. The desired beam diameter is usually equal to or slightly larger than the back aperture of the objective you are using. Filling or slightly overfilling the back aperture ensures a tight focus on the sample with maximal power density whereas under filling causes a slightly large beam waist at the focus and therefore a lower power density. Next, find the NA of the fiber out of which laser light is emitted. Fiber NA's are always well documented and can be found on any fiber specification sheet. Make sure the collimation package has an NA that somewhat closely matches the NA of the fiber (but if in doubt, pick a slightly larger NA so as to collect all of the laser light). Finally, make sure that the collimation package is compatible with the fiber termination, whether that be FC/PC or APC.

Once a collimation package has been selected, it's time to collimate! In the case of a fixed focus package, all that needs to be done is to plug in the fiber. If an adjustable collimator was purchased, find a room with ample space (>5 meters), plug the laser fiber into the package, mount the packaging into a kinematic collimator mounting adapter (also available on Thorlabs), attach a post to the adapter, put on the appropriate laser eye protection, and shoot the laser beam across the room. Find a laser card and track the spot size of the laser as it propagates. If the laser focuses and diverges, it is not collimated. Adjust the ring on the collimation package to move the lens elements in the package relative to the laser fiber. This will have the effect of shifting the distance from the fiber to the laser focal point. Notice how rotation of the adjusting ring in one direction causes the focus of the laser beam to shift closer or further away from the collimator. Use this information to determine which way to turn the ring such that the laser focus moves further and further away (this is why collimation is often referred to as "focusing at infinity.") Adjust the ring until the laser maintains the same beam size over the entirety of the propagation distance.

Collimation can be tedious because it is easy to lose track of the laser beam while tracking its propagation through space. To make this job easier, it's helpful to make collimation a two person job, where one person turns the adjustment ring and the other person keeps track of the laser focus. Equally annoying is collimation of a near-IR laser because those wavelengths are invisible to the human eye. Laser viewing cards that fluoresce under IR light are available from Thorlabs. The Thorlabs VRC4 laser card is particularly good for divacancy-related work because it does not bleach and the fluorescent spot on the card remains crisp, making it easier to determine the laser spot size by eye. "Find-R-Scope" hand-held IR viewers are also available for purchase online and are extremely helpful when looking at light in areas where are card cannot be easily used.

4.1.4 Periscope alignment

A fast steering mirror (FSM) or periscope can be used to achieve the "scanning" part of scanning confocal microscopy. In essence, these motorized components allow for the laser to be rastered across the sample. The periscopes used in the Awschalom lab typically have three degrees of motion (x, y, and z) and are formed using three motorized Newport micrometer stages (IMS series) controlled by a Newport XPS Motion Controller (XPS-D4) (Fig. 4.1). Kinematically mounted Thorlabs elliptical mirrors (PFE10-P01, H45E2, KS2) are attached to two of the motorized stages. Elliptical mirrors with a two-inch major axis are used because they have a larger effective surface area than standard 1-inch mirrors, providing users with more flexibility. The objective is mounted to the the stage closest to the sample and cryostat (A in Fig. 4.1). Typically, this stage is responsible for depth control and shuttles the objective along the z-axis of the periscope to move the focus of the objective in and out of the sample. To mount an objective, check the threading on the backside of the objective (RMS threading is most common). Purchase a threading adapter that allows the objective to be mounted into a threaded kinematic mount (such as Thorlabs KM200T).

The function of the periscope is to scan a microscope objective across a sample in all three

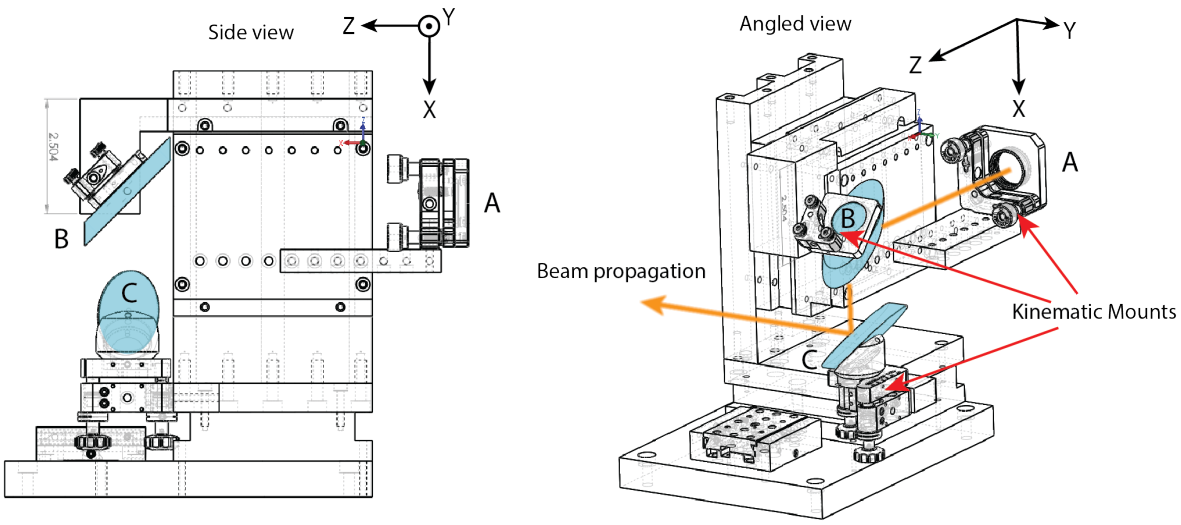

Figure 4.1: Periscope assembly. The objective/alignment laser is mounted in A. Elliptical mirrors (blue shaded regions) are placed in kinematic mounts with tip and tilt degrees of freedom (B and C). When the z-axis of the periscope is jogged, A moves relative to B. When the x-axis of the periscope is jogged, the distance between A and B is unchanged while both A and B move in unison relative to C. When the y-axis of the periscope is jogged, A, B and C all move in unison relative to the rest of the confocal setup.

dimensions while ensuring the path of the excitation lasers coupled into the objective are correctly aligned to the back of the objective even when the objective is physically moved. Concurrently, collected and collimated photoluminescence exiting the backside of the moving objective should be coupled back into the rest of the setup such that it reaches the detector without any shifts in angle. In other words, because the free space optics in the confocal microscope are static, the periscope has the job of ensuring that translation of the microscope objective does not necessitate adjustment of the static part of the confocal setup. To align a periscope, first set up an alignment laser:

1. Select a visible laser such as the compact, pre-collimated Thorlabs CPS635R module and mount it in an adapter with pitch and yaw control (Thorlabs KAD8F).

2. Find a lens tube that is at least 1 meter long (the longer the better). Long lens tubes can be made by screwing multiple Thorlabs SM1L40 tubes together. Mount a single threaded iris (Thorlabs SM1D12C) onto one end of the tube. Add one more lens tube to the other side of the iris.

3. Mount a threaded power meter (Thorlabs S121C, PM100D) to the end of the lens tube that was added after the iris.

4. Mount the alignment laser on the end of the lens tube, opposite the end with the power meter.

5. Close down the iris to generate a small aperture.

6. Turn on the alignment laser. Adjust the tip and yaw of the laser kinematic adapter mount to maximize transmission of the laser through the iris onto the head of the power meter.

The above steps ensure that the path of the laser is exactly co-linearly aligned with the axis of the kinetic objective mount. Next, screw the alignment laser into the threaded objective mount on the periscope and follow these steps:

1. Mount the alignment laser in the objective mount (Point A in Fig. 4.1) such that it points away from the cryostat and towards the rest of the confocal setup. The elliptical mirrors mounted to the other two stages of the periscope (Points B and C in Fig. 4.1) should be roughly positioned such that the laser reflects off both of them and propagates towards the rest of the confocal setup.

2. Jog the periscope along the z-axis such that the only the stage connected to the objective mount/laser moves between its two extrema of travel towards and away from the sample. In other words, only Point A shown in Fig. 4.1 should be moving.

3. Pick a spot several feet away from the periscope, and observe the movement of the laser beam on a sheet of paper stationed at that point. The laser spot will likely move as the z-axis stage is jogged. The aim of the alignment is to ensure that the laser spot does not change position as the z-axis stage moves. Adjust the micrometers on the kinematic objective mount that holds the laser until no deviation is seen on the sheet of paper (Fig. 4.2).

4. Once the z-axis has been aligned, move on to the y-axis. During y-axis adjustment, both the stage connected to the objective/alignment laser (Point A in Fig. 4.1) and the mirror closest to the objective/alignment laser (Point B in Fig. 4.1) are moved in unison, such that their spacing relative to the mirror farthest from the objective changes. Jog the y-axis of the periscope, and repeat Step 3, adjusting only the micrometers on the kinematic mount of the mirror closest to the objective (Point B in Fig. 4.1) such that the laser spot on the piece of paper does not move while the periscope jogs.

5. Move on to the x-axis. This entails all three motorized stages moving in unison (aka the x-axis stage moves and brings the y-axis stage and z-axis stage with it) such that none of the optics on the periscope move relative to each other. Instead, the periscope is moving relative to the rest of the setup as a unit. Jog the x-axis of the periscope, and repeat Step 3, adjusting only the micrometers on the kinematic mount of the mirror farthest from the objective (Point C in Fig. 4.1) such that the laser spot on the piece of paper does not move while the periscope jogs.

The above process ensures that the path of the laser is parallel with the motion of all three periscope stages, so that movement in the stages do not translates to shifts in the location or angle of incidence of the laser on the two mirrors (Fig. 4.2). It is very important to align the periscope by only jogging one axis of motion and adjusting only the corresponding optic at a time. Once a periscope has been aligned, the objective can be screwed back into the kinematic mount and is ready for use. However, when handling new kinematic mounts, it

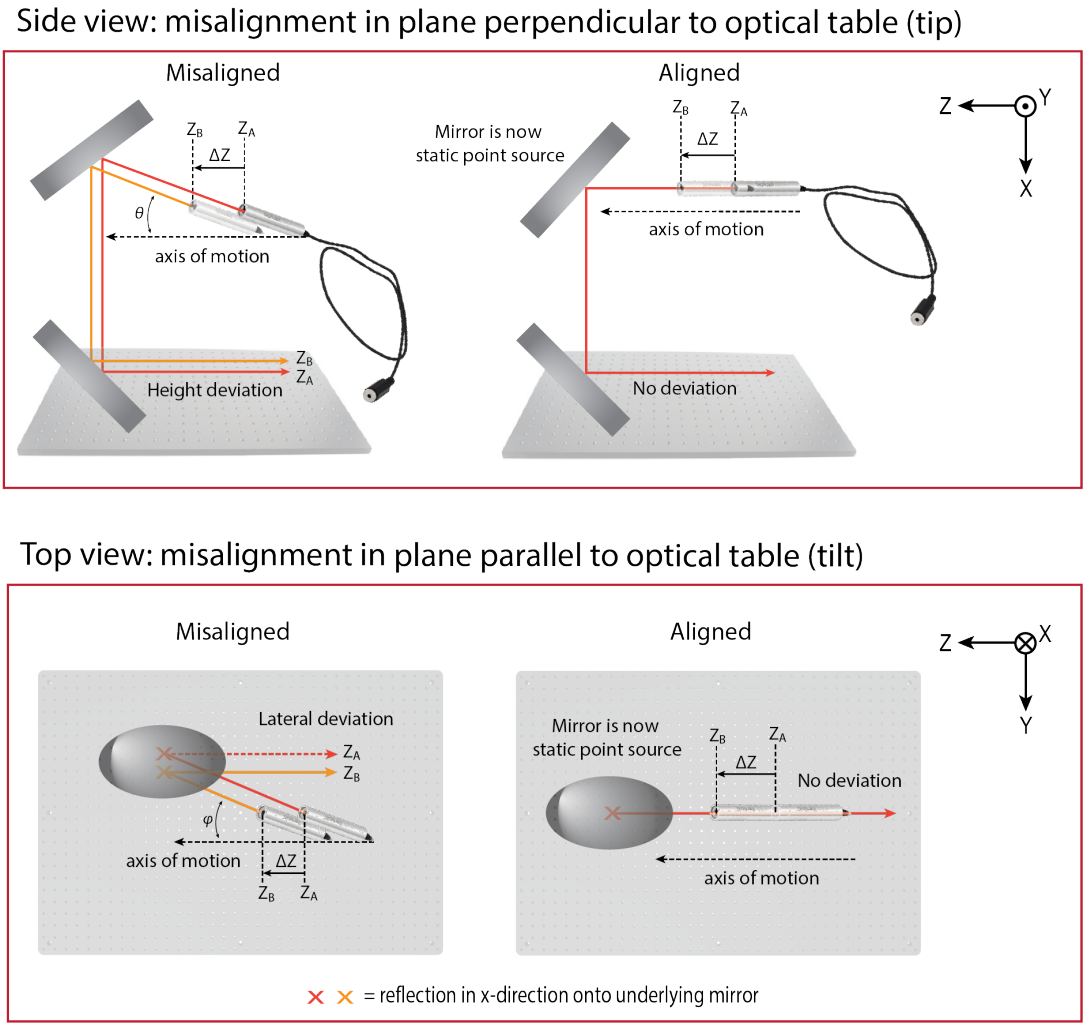

Figure 4.2: Periscope alignment. The aim of periscope alignment is to ensure that beam propagation is exactly parallel with the axis of motion. Here, for alignment of the z-axis of the periscope, tip (θ) and tilt (ϕ) misalignment present in different ways. For misalignment in the plane perpendicular to the optical table (tip), misalignments will appear as height deviations in the laser beam as the periscope stage is jogged. The tip axis of the kinetic mount holding the alignment laser should be adjusted until no deviation is seen in height. For misalignment in the plane parallel to the optical table (tilt), misalignments will appear as lateral deviations in the laser beam as the periscope stage is jogged. The tilt axis of the kinetic mount holding the alignment laser should be adjusted until no lateral deviation is seen. Once the z-axis of the periscope is aligned, the mirror closest to the alignment laser effectively acts like a static point source when the z-axis is jogged. To align the x-axis (y-axis), the same procedure is followed but adjustments are only performed on the kinematic mount holding the mirror closest to (farthest from) the alignment laser.

is common for the springs and mechanical components to shift and settle over several days. Thus it is recommended that the periscope alignment be checked several days after the initial alignment procedure, and that small adjustments be made as necessary.

4.1.5 Defining an excitation path

The periscope alignment sets the alignment of the rest of the setup. After aligning the periscope, the goal is to get the collection and excitation paths to be totally colinear with the laser coming out of the periscope. For now, let's focus on getting the excitation laser to be totally colinear with the alignment laser coming out of the periscope. First, place two irises along the path of the alignment laser coming out of the periscope, at least a foot or so apart, and screw those irises down into the optical table. Two points define a line, and these irises set a reference line that can later be used to realign the collection and excitation paths in case things become misaligned after the periscope alignment laser is removed.

Set up the excitation laser by first collimating it (Section 4.1.3). After collimation, mount the excitation laser to a post screwed into the optical table. Next, place a coupling optic, such as a dichroic mirror, at a 45 degree angle relative to the path of the alignment laser (note here, I said *alignment* laser and not *excitation* laser). The dichroic is referred to here as a coupling optic because it is responsible for coupling the excitation laser into the setup so that its path overlaps with the alignment laser path and so that the excitation consequently enters the periscope at the correct angle. The dichroic can be thought of as a fancy edgepass mirror that allows certain wavelengths of light to pass through, while it reflects other wavelengths. Use at least one mirror pair in a bow tie or parallel configuration (Fig. 4.3) to steer the excitation laser onto the coupling optic (dichroic) and roughly onto the two irises. This will result in the excitation laser and the periscope alignment laser sharing the same path. To do this, coarsely adjust the relative positions of the two mirrors by changing the location they are mounted on the optical table. Once this rough adjustment is done, use the micrometers on the kinematic mirror mounts to walk the laser beam so that it exactly passes through

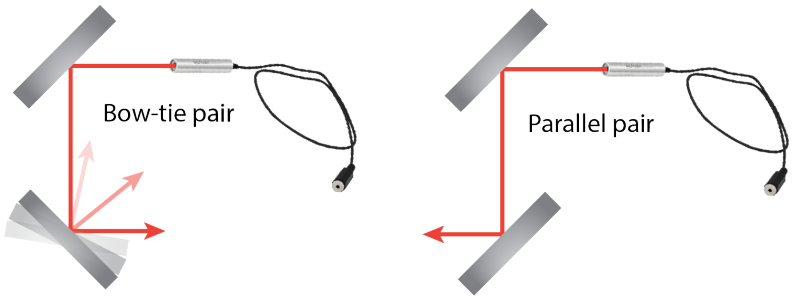

Figure 4.3: Mirrors can be placed in bow-tie or parallel configuration for beam steering. Bow-tie configurations are common when changing the direction of beam propagation.

the closed down apertures of the irises. This alignment process is discussed in more detail in Sections 4.1.6 and 4.1.7.

4.1.6 Laser alignment with mirrors

For each laser, at least two mirrors are needed to steer the laser beam to an area of interest. Typically, protected aluminum (Thorlabs PF10-03-G01) or protected silver (Thorlabs PF10-03-P01) mirrors are a good option because they are extremely broadband. Always check the reflectance data of optical components, especially for polarized light and for different angles of incidence, to check that they operate without any surprises at your wavelength, polarization, and angle of interest.

At least two mirrors should be used each time the direction of the laser is changed. A standard steering technique is to use a mirror pair in either a bow-tie or parallel configuration, as pictured in Fig. 4.3. Why not just use a single mirror with tip and tilt degrees of motional freedom? In confocal microscopy, all the excitation and collection paths must be co-linear (share the exact same path). It is not possible to tip or tilt a single mirror to make one beam colinear with another. Mirror pairs allow one to use one mirror to change the incident location of the beam on the second mirror, where the second mirror is then used to provide angle control (Fig. 4.4). Let's imagine a laser beam reflecting off of a single mirror as a single ray vector, and the reference path as a line. If the origin point of the ray vector is not somewhere on the reference line (Point A in Fig. 4.4), no amount of angle control will make

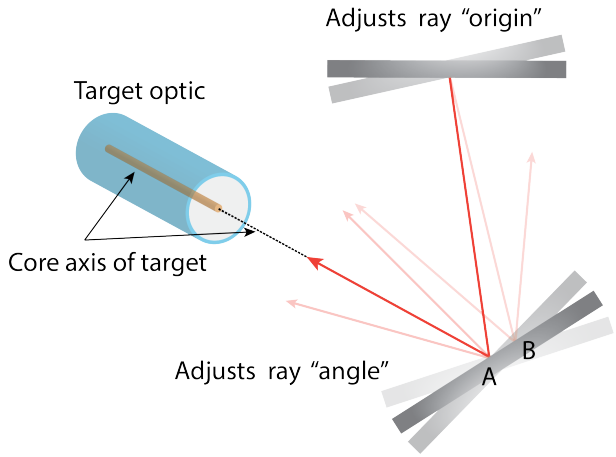

Figure 4.4: Walking the beam. Two mirrors are necessary when steering a beam to be colinear with another reference beam or the axis of a target optic such as a fiber or objective. The far mirror adjusts the location of incidence (A or B) of the beam on the mirror closest to the target. The beam can only be in alignment when it is incident on the intersection of the core axis of the target optic with the close mirror (A). From there, the angle of the beam is adjusted by the close mirror. The iterative process of adjusting both mirrors is called walking the beam.

it co-linear with the reference (Point B in Fig. 4.4). Thus two mirrors are needed: one to shift the origin point of the vector to be on the reference, and the other to align the vector to be parallel with the reference.

4.1.7 Walking a beam

The process of using a mirror pair to align a beam to be co-linear with some reference path is called "walking the beam" (Fig. 4.4). The feedback process for this kind of alignment takes two forms. It can be visual, where we use our eyes to see if the beam is hitting the two points that define the reference path (such as the two irises mentioned in Section 4.1.5). Or, it can be based on signal from a detector. For example, during fiber coupling, two mirrors may be used to maximize transmission of a beam into a fiber with a power meter attached to the other side. The power meter signal is used to feed back on the mirror adjustments so a global maxima of transmission is found. Regardless of the end goal, two mirrors in a bow-tie or parallel configuration 4.3 are necessary to walk a beam. The mechanical procedure for

walking the beam goes as follows:

1. Pick one micrometer knob on each kinematic mirror mount to be adjusted. Assign one of the two micrometers as the "constant" micrometer and the other as the "adjust" micrometer.

2. Turn the constant micrometer clockwise, by about a tenth or eighth of a turn.

3. Turn the adjust micrometer in whichever direction maximizes a feedback signal such as power, photoluminescence, or visual reference. Make a mental note of this signal.

4. Turn the constant micrometer clockwise again by an tenth or eighth of a turn.

5. Repeat Step 3 again. If the new maxima is greater than it was before, continue with Steps 2 and 3. Fine tune the angle of rotation of the constant micrometer as needed.

6. If the signal maxima decreases as the constant micrometer continues to be turned clockwise, turn the constant micrometer counterclockwise and repeat Steps 2 and 3 and iterate until a global maxima is found.

7. Repeat Steps 1 through 6 for the other two micrometer knobs on the kinematic mirror mounts that have not been adjusted yet to align the other degree of freedom.

While the above process is described for a situation where two kinematically mounted mirrors are used, walking the beam is an iterative process that can be used for any situation where there are two optics. When beam walking is used to align to single defects, the thing being aligned dictates the laser power at which the walking should occur. In the case that the collection path is being aligned, higher laser powers should be used. In the case that the laser excitation path is being walked, low laser powers should be used. This is because a lower power corresponds to a smaller laser spot size, where a smaller spot size allows for finer control and adjustment to ensure the center of the laser spot is really "on" the defect.

4.1.8 Defining a collection path

The collection path is the path along which emission from the phonon sideband (see Section 2.0.7 is spectrally picked off, filtered to remove laser scatter, and routed towards a photodetector. The collection optic, usually a dichroic mirror, that is used to pick off the collection path is a crucial element in the confocal setup and should be selected carefully. In designing the confocal setup I built during my graduate work, we considered many dichroics with a frequency cutoff close to the ZPL of the divacancy (1130 nm) so that we could collect as many photons from the divacancy's phonon sideband as possible. While there were several options, we selected the Thorlabs DMSP1020B shortpass dichroic because of its superior reflectance of both S and P polarized light, and its large surface area that allowed for more flexibility during alignment.

Once the key collection optic has been selected, it's time to set up the mirror pairs, filters, and fiber coupling scheme to get photons from the divacancy sideband into the fiber connected to the photodetector. Place the dichroic filter in the periscope alignment laser path at a 45 degree angle to define where in the setup the collection path will begin. Next, decide which filters will be used to remove laser scatter off the sample surface. As the goal is to collect photons from the phonon sideband with longer wavelengths, the filters should pass wavelengths longer than the laser. For example, resonant excitation of PL2 divacancies is typically around 265.2 THz. To filter laser scatter, two FEL1150 long pass filters are often placed in series to provide extra attenuation of the resonant laser. When off resonant excitation at 905 nm is used, an additional filter is needed to attenuate laser scatter, such as the Thorlabs FEL1050.

Once the dichroic and filters are selected, a mirror pair and pre-aligned fiber launch (Section 4.1.9) should be set up. The mirror pair steers photoluminescence into a collection optic mounted to a fiber launch, which focuses the collected photons into a fiber connected to the photodetector. Selecting the collection optic is another crucial step of setup design. Typically, either an aspheric or achromatic lens is used. Aspheric lenses reduce spherical

aberrations that cause light hitting different parts of the lens to focus at different depths. Achromatic lenses reduce chromatic aberrations that cause different colors of light to focus at different depths away from the lens. In general, from my graduate work, I found that the choice of aspheric versus achromatic did not matter that much. Rather, the collection efficiency was more a matter of trial and error and more likely had to do with the NA of the collection optic. This brings us to a very important point: the NA of the collection optic should ideally be perfectly matched the collection fiber. If a perfect match cannot be found, it is better for the NA of the fiber to be slightly larger than that of the collection optic.

4.1.9 Fiber launch alignment

A fiber launch is a manually adjustable three-axis stage that allows users to optimize the coupling of light into a fiber (Fig. 4.5). The top of the fiber launch has a two small optical breadboards to accommodate a threaded collection optic and a fiber patch cable. The breadboard holding the collection optic remains stationary while the breadboard that holds the patch cable can be moved using the micrometers. Before the fiber that routes defect photoluminescence to the SNSPD can be mounted to the fiber launch, the fiber launch must be pre-aligned such that the central axis of the fiber patch cable mount is colinear with the central axis of the collection optic. To perform this alignment, follow these steps:

1. Find a visible wavelength, fiber-coupled alignment laser such as the Thorlabs HLS635.

2. Plug the alignment laser into the fiber patch cable holder. This holder should be mounted to the breadboard that can be adjusted with the micrometers. Place the collection optic in a threaded mount attached to the immobile breadboard. The positions of the mounts should be coarsely adjusted such that the alignment laser propagates through the collection optic.

3. Find a part of an optical table that has plenty of free space such that the alignment laser can propagate for a long distance (>2 meters).

4. Square the base of the fiber launch with the grid defined by the optical table. A good way to do this is to place two screws in the optical table and then push the fiber mount base against the screws, clamping down the fiber launch to ensure that the edge of the fiber launch base is parallel with the lines defined by the screw holes in the optical table.

5. Align the focus (z-axis) by collimating the alignment laser through the collection optic. Adjust the z-axis micrometer of the fiber launch to bring the fiber and collection optic closer or further away from each other until the alignment laser propagates without focusing. Because the wavelength of the alignment laser will likely be different from the wavelength of the collected photoluminescence, chromatic aberrations will require adjustment of the focus when performing final alignments using real photoluminescence as a feedback signal. However, this step will set the relative positioning to be roughly correct. Note that this step will be impossible if the laser and collection optic are not somewhat level. Adjust the x and y axes coarsely so that the beam at least makes it through the optic for z-alignment to be possible.

6. Pick a set of holes on the optical table that are parallel to the z-axis of the fiber launch, and close to the path of propagation of the alignment laser.

7. Align the x and y axes. Find a beam block or alignment screen such as Thorlabs TPSM1/M. Note where the alignment laser spot falls on the beam block when the beam block is brought closer to or farther from the fiber launch along the line defined in Step 6. Make sure that the same part of the base falls on the line defined in Step 6 when moving the beam block. Adjust the x and y micrometers on the fiber launch such that the laser spot always lands on the same part of the beam block regardless of the distance between the beam block and the fiber launch.

8. Iterate Steps 7 and 8 until the fiber launch is fully aligned.

9. The alignment laser can now be removed and replaced with the patch cable that is needed for fiber coupling.

The steps outlined above can be thought of as adjusting the fiber launch such that the fiber and the collection optic share the same central axis.

4.1.10 Back-aligning the collection path

Once the fiber launch has been pre-aligned, mount the fiber launch on the optical table such that the alignment laser in the fiber launch reflects off of a mirror pair and off the collection dichroic, into the rest of the setup. Because the dichroic will likely have a pass band that does reflect the alignment laser light in the same way that the dichroic will reflect collected photoluminescence, it may be helpful to replace the alignment laser with a near-IR laser for this step.

Until now, two alignment lasers have been discussed: one placed in the objective mount to align the periscope, and one mounted to the fiber launch to align the collection path. The goal is to now use the mirror pair in the collection path to make the lasers co-linear. Walk the beam of the back-alignment laser mounted to the fiber launch using the mirror pair such that it perfectly overlaps the path of the laser in the objective mount. This alignment can be easily checked by using a translucent piece of lens tissue to see if the laser spots are coincident along various parts of the setup. If irises have been set up along the path of the alignment laser mounted to the periscope, those can also be used.

4.1.11 Selecting fibers

The fiber used to channel collected photoluminescence to the photodetector should be specified to maximize transmission of those photons over long distances. For divacancy characterization, a polarization maintaining 1060 XP fiber with metal jacketing is often used to reduce coupling of room lights into the fiber. Fiber terminations are also critical. The

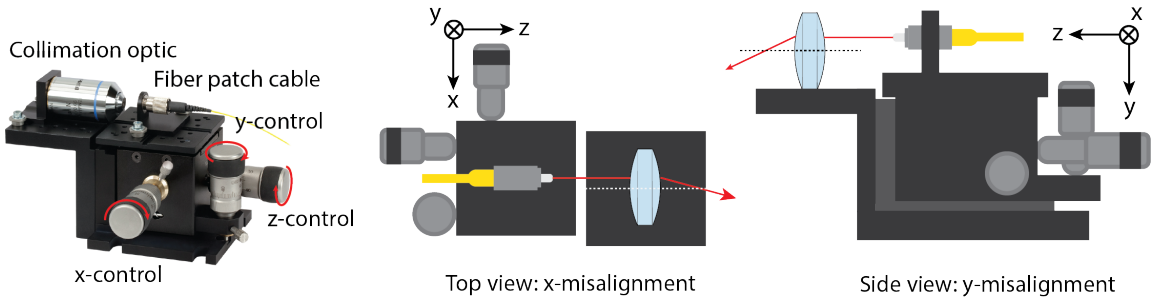

Figure 4.5: Misalignment of the fiber launch causes deviation of the laser path relative to the central axis of the collimation optic (dashed lines).

setup I built used a UPC termination, which stands for "ultra physical contact." Other fiber terminations include FC/PC ("ferrule connector physical contact") and APC ("angled physical contact"). FC/PC is the most common termination and is sufficient for defect photoluminescence collection. APC terminations minimize back-reflections of light off the ferrule interface and should be used for fiber-coupled lasers because back reflections into the laser diode may cause power instability.

Using polarization maintaining fibers is not particularly important for fiber-coupled lasers, as there should be a full suite of polarization control such as half and quarter wave plates in the confocal setup. However, for entanglement experiments, the polarization of emitted photoluminescence is important, so a polarization maintaining collection fiber should be considered.

4.1.12 Fiber coupling

Fiber coupling optimizes transmission of external light source into a fiber by using a mirror pair, a pre-aligned fiber launch (Section 4.1.9), and a focusing optic such as a lens. The focusing optic should be specified for the wavelength of interest and should be as closely NA-matched to the fiber as possible. From there, a power meter can be attached to the end of the fiber, while the beam that is to be coupled into the fiber is walked using the mirror pair (Fig. 4.4) to maximize the transmitted power into the fiber (Section 4.1.7).

4.1.13 Superconducting nanowire single photon detectors

Many single photon-sensitive detectors exist, but here we will discuss superconducting nanowire single photon detectors (SNSPDs). In its most basic form, an SNSPD is simply a cryogenically cooled, meandering nanowire made out of superconducting material such as Nb or NbN. The nanowire is connected to external readout circuitry that measures the voltage across the wire. When no photons are incident on the nanowire, it remains in a superconducting state such that it has zero resistance. Upon a photon incidence event, the superconductivity of the nanowire is broken, and the finite resistance of the wire is measured out as a voltage spike on the readout circuitry. The nanowire eventually returns to a superconducting state over a timescale called the reset time. The Quantum Opus SNSPDs used in the Awschalom group have been designed with anti-reflection coatings to improve detection in the near-IR regime and they have 80% or greater quantum efficiency. Their typical reset time is on the order of tens of nanosecond with a jitter of tens of picoseconds. The bias current of the SNSPD used in experiments should be adjusted such that the ratio between the background dark counts and photoluminescence counts is maximized. While somewhat arbitrary, the bias current is often set such that there are only 5 to 10 background counts per second.

4.1.14 Acousto-optic modulators (AOMs)

AOMs are used to generate laser pulses. Two varieties of AOMs exist: free-space and fiber-coupled. Fiber-coupled AOMs are "plug and play," and therefore do not require any alignment, while free-space AOMs need to be aligned. At their core, both types of AOMs use a piezoelectric crystal such as quartz. Electrical actuators attached to the piezo apply an ac signal that generates a periodic modulation of the crystal's index of refraction. This effectively creates a grating, such that light passing through the modulated piezo undergoes Bragg diffraction. Gating the ac signal on the actuators turns the diffraction peaks on and off, allowing the laser to be pulsed.

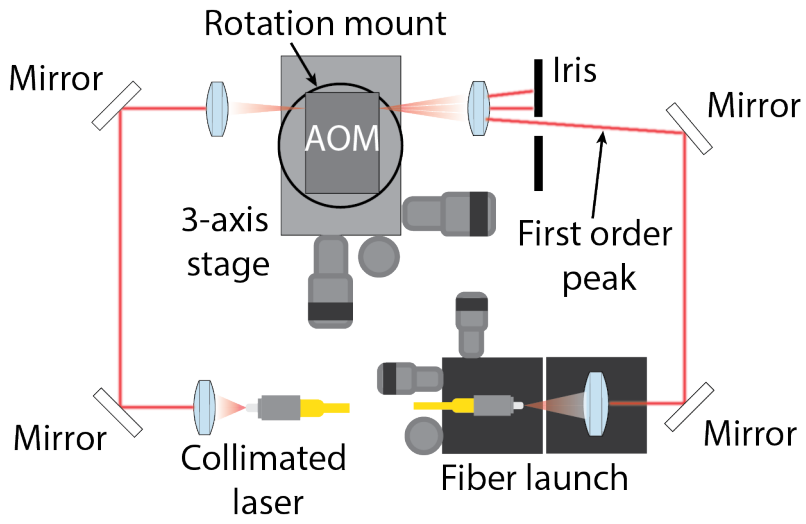

Figure 4.6: Free space AOM box should be aligned to maximize both power output of first order diffraction peak while also maximizing the extinction ratio.

Free-space AOMs should be set up as a separate part of the confocal setup that laser light passes through before entering the excitation path. For a fiber-coupled laser, the AOM setup will consist of a collimation optic, an AOM, a focusing lens pair, a rotation stage, a three-axis translation stage, an iris, two mirror pairs, and a fiber launch with a collection optic on it to route laser light back to the rest of the setup. These components are all mounted on an optical breadboard that can be placed remotely away from the rest of the setup in a modular fashion (Fig. 4.6). To align the AOM box, follow these steps:

1. Collimate the light coming out of the fiber-coupled laser following the steps outlined in Section 4.1.3. Mount the collimation optic to the breadboard.

2. Place a mirror pair next to the output of the laser. Place the focusing lens pair after the mirror pair. Adjust the spacing of the lens pair such that they are $2f$ apart, where f is the focal distance of the lenses. Use the mirror pair to steer the laser through the lenses such that the laser passes through the center of each lens. The laser will become tightly focused between the lenses. Obviously, the $2f$ pair should be selected such that their separation is greater than the width of the AOM and the stages the AOM is mounted on.

3. Mount the rotation stage on top of the three-axis translation stage. Mount the AOM on top of the rotation mount. Mount this stack to the breadboard, between the $2f$ focusing lens pair.

4. Place a power meter at the output aperture of the AOM. Use the rotation stage and three-axis translation stage to maximize power transmission of the laser through the aperture of the AOM. This should correspond to the AOM being placed at the point of tightest focus of the laser.

5. Turn on the RF modulation of the AOM and visually find one of the first order peaks of the laser. Use an iris to block the zeroth order peak output such that only the first order peak reaches the power meter. Use the mirror pair, rotation stage, and translation stage to maximize the power of the first order peak.

6. Place a mirror pair behind the iris, making sure that the iris only allows the first order peak to hit the mirrors. This mirror pair will eventually be used to fiber couple the laser so that it can be routed to the rest of the confocal setup.

7. Place a pre-aligned fiber launch (Section 4.1.9) behind the second mirror pair.

8. Walk the first order peak of the AOM into the patch cable mounted on the fiber launch using the steps for fiber coupling steps outlined in 4.1.12.

9. Check the extinction ratio of the AOM. To do so, check the power P_{off} transmitted through the output fiber when the laser is on but the AOM RF drive is off. Next, check the power P_{on} of the first order AOM peak that is transmitted through the output fiber. It is undesirable for laser light to be leaking into the setup and onto the sample when the AOM is turned off, since this may cause unwanted excitation, ionization, or charge resetting effects during an experimental sequence. To ensure that this does not happen, make sure that $P_{off}/P_{on} > 10^{-3}$. If the extinction ratio is not high enough,

the angle of incidence of the laser into the AOM may need to be adjusted, or the AOM may be functioning improperly.

4.1.15 Divacancy characterization setup layout and components

The confocal microscope can be divided into an excitation component (Fig. 4.7) and a collection path (Fig. 4.8). In addition to free space optics such as mirrors and filters, the confocal microscope used in the experimental work discussed in this thesis uses a variety of other components such as lasers, cameras, and filters. These components include:

- **Olympus 100x LMPLN-IR/LCPLN-IR** microscope objective with NA=0.85 and 1.48 - 1.18 mm working distance. This objective is meant for cryogenic use and is mounted inside the cryostat.
- Two **Toptica DL Pro** tunable, near-IR lasers. Two lasers are used so more than one of the divacancy's optical transitions can be addressed at a time.
- **QPhotonics QFLD-905-200S** 905 nm fiber-coupled laser mounted in **Thorlabs CLD1015** driver for off-resonant excitation.
- **Thorlabs LP705-SF15** 705 nm fiber-coupled laser mounted in **Thorlabs CLD1011LP** driver for divacancy charge reinitialization.
- **QPhotonics QFLD-1160-300s** temperature tunable fiber-coupled laser mounted in **Thorlabs CLD1015** driver for divacancy spin-to-charge conversion via optical ionization.
- **Newport FSM-300-01** fast steering mirror system for 2D rastering and scanning of the sample surface.

All laser pulse generation is done outside of the confocal setup inside AOM "boxes," where the AOMs receive TTL pulses from the AWG. In the case where free-space AOMs are used,

the modulated laser light is fiber-coupled and sent to the confocal setup where it is collimated and coupled into the excitation path. A more thorough description of free-space AOM box alignment is outlined in Section 4.1.14. For fiber-coupled AOMs, no alignment is necessary. The two resonant lasers in the confocal setup used in the work presented in this thesis were spectrally and temporally controlled in a box that is separate from the rest of the setup (Fig. 4.9). This box is entirely fiber-coupled and contains:

- Two **AAOptoelectronics MT250-IR6-Fio-SMO-J1-A-VSF** fiber-coupled AOMs used to pulse the two resonant lasers.
- Two **Thorlabs V1000A** optical variable attenuators for voltage-adjustable attenuation of the resonant lasers.
- Two **Thorlabs TW1064R5A1A** 90:10 split fiber couplers to pick off 10% of the resonant laser power for wavelength/mode characterization and the other 90% to the AOMs and rest of the confocal setup.
- Two **Thorlabs TW1064R5A1A** 50:50 split fiber couplers to send 50% of the picked off laser emission to the Fabry-Perot interferometer, and the other 50% to the wavemeter.
- **Thorlabs SA200-8B Fabry-Perot** interferometer used to determine if tunable lasers are single mode.
- **Newport SPSN-9-22-FCAPC 2x2 Single Mode Fiber Switch** to control which of the resonant lasers is routed into the Fabry-Perot interferometer.
- **High Finesse WS-7** fiber-coupled wavemeter to monitor the wavelength of the two tunable lasers.
- Two **Thorlabs FPC034** manual fiber paddles to adjust the polarization of the laser light.

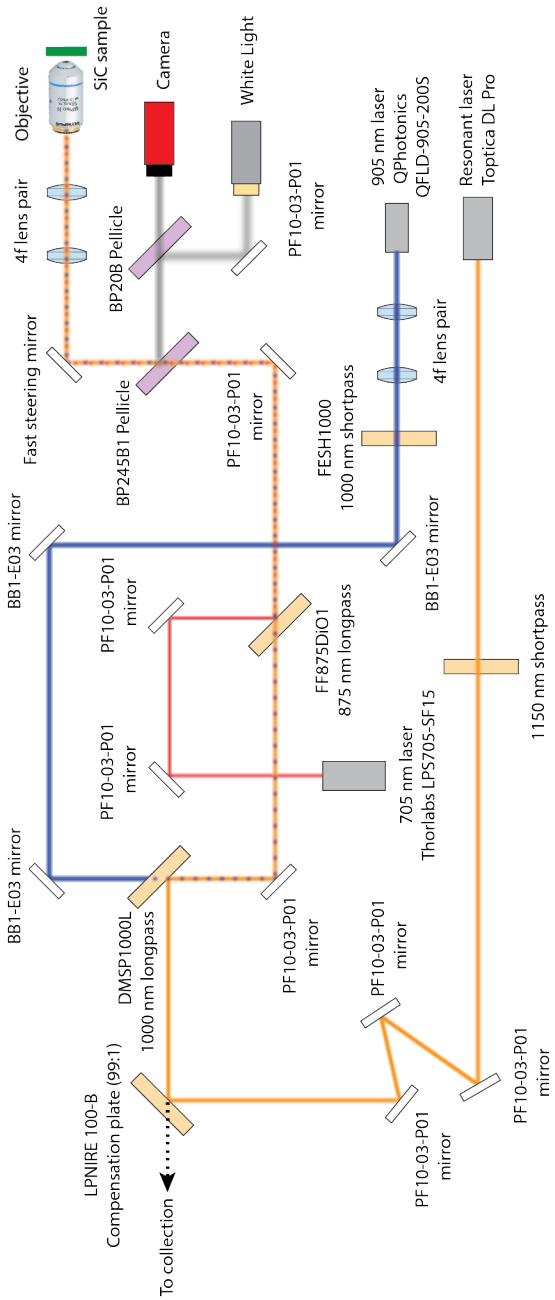

Figure 4.7: Confocal microscope excitation path. The 705 nm and 905 nm lasers are subject to temporal control via free-space AOMs before entering the confocal setup. The two resonant lasers are spectrally and temporally controlled before entering the setup. Dashed lines indicate overlaps of different laser wavelengths.

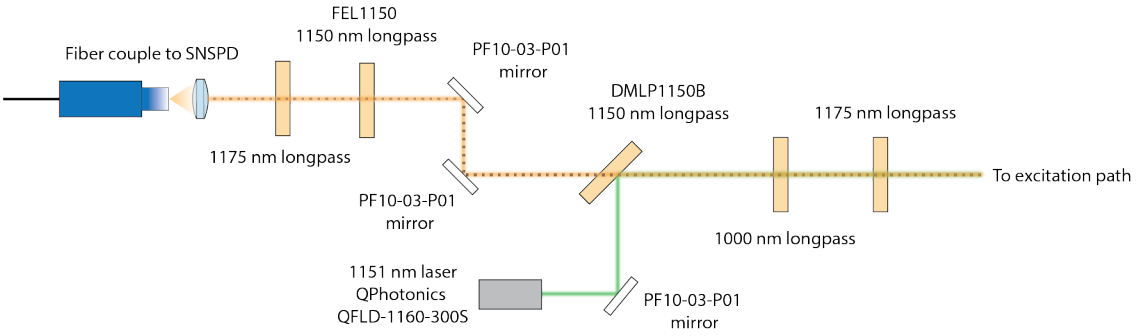

Figure 4.8: Confocal microscope collection path. An 1151 nm laser is used for spin-to-charge conversion. Instead of using an AOM, the 1151 nm ionization laser is directly modulated. Dashed lines indicate overlap of different wavelengths.

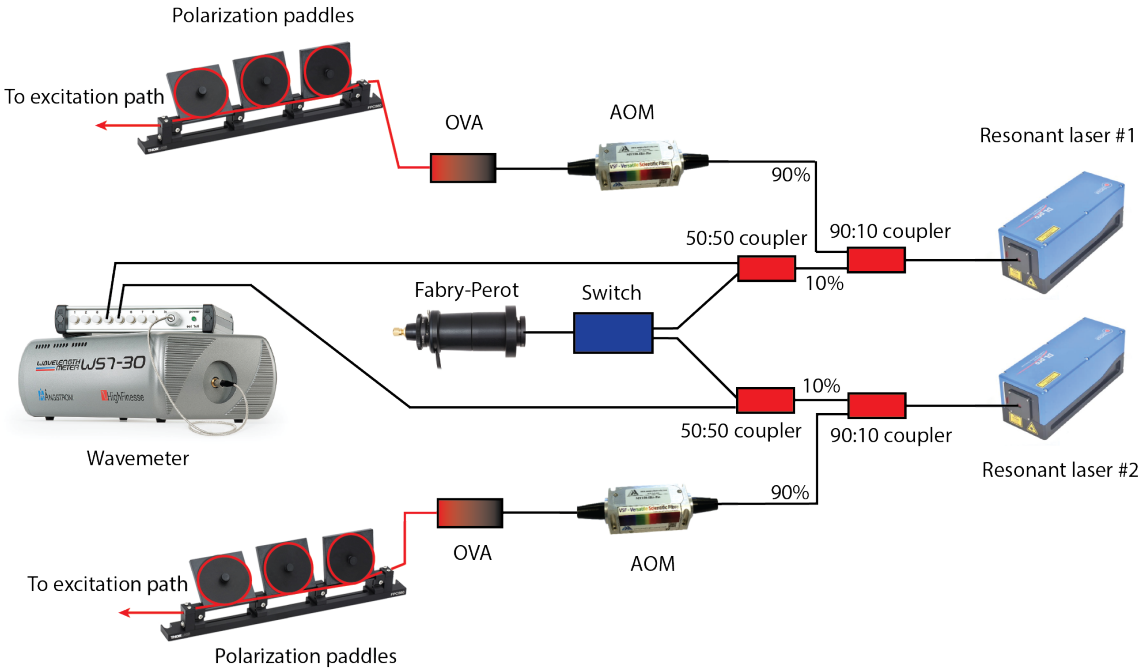

Figure 4.9: AOM box containing fiber-coupled optics for spectral and temporal control of tunable resonant lasers. Laser emission is sent to a Fabry-Perot interferometer to determine if the laser is single mode at a given wavelength, as well as a wavemeter to measure the output wavelength.

4.2 Electronics

A typical electronics configuration for a divacancy characterization setup is shown in Fig. 4.10. Generally, the electronics in a divacancy characterization setup can be divided into those responsible for defect excitation and manipulation, and those responsible for signal collection. The key piece of equipment that maintains synchronization between all electronic components is the arbitrary waveform generator (AWG). The AWG can be thought of as the "conductor" of the setup because it sends voltage pulses to various components (AOMs, signal generators, microwave switches, etc) to turn those components on or off. The shortest pulse that an AWG can produce is determined by the AWG sampling frequency multiplied by the minimum sample number. However, when very fast pulses are needed and a high sampling rate is used, it can be common for an entire pulse sequence to contain so many points that the AWG runs out of memory. Fortunately, most divacancy characterization experiments do not require extremely fast pulses and the most demanding part of sequences will typically come from generating microwave pulses that are several tens of nanoseconds long.

Most AWGs have a combination of analog and digital outputs. Whereas analog output channels on the AWG can produce any arbitrary pulse shape, digital outputs are constrained to square pulses of a set height (typically around 2-5V). The requirements on the number of analog or digital channels will depend on the type of experiment being performed. For divacancy experiments, one digital channel is necessary to gate photon counts from the SNSPD, at least two analog channels are necessary in order to perform IQ modulation of the microwave signal generators for spin manipulation, and at least one digital channel is required to pulse each laser. If differential measurements are being performed (Section 3.3), an additional digital channel is needed to gate pulses from the SNSPD for post-processing.

4.2.1 Excitation and control electronics

The excitation electronics generate the laser and microwave pulses to excite divacancy optical transitions and perform spin manipulation. In addition to gating of the AOMs via the AWG, the excitation electronics consist of the following:

- **SRS SG396** signal generator that produces microwave frequencies for driving of divacancy spin transitions. The signal generator has two inputs on the back panel that receive analog pulses from the AWG so that IQ modulation can be performed.
- One **Minicircuits ZASWA-2-50DR** microwave switch connected to the output of the signal generator (Microwave gate in Fig. 4.10) to ensure complete attenuation when no microwave driving is supposed to be happening. Each switch is gated via an input port that receives digital pulses from the AWG, and two output ports. ZASWAs require a +5V and -5V DC power supply, which is typically provided using a **BK Precision 1550 DC Power Supply**. Unused ZASWA outputs should be terminated with a 50Ω cap to prevent unwanted microwave reflections.
- **Amplifier Research Model 25S1G4A** 25 Watt, high frequency amplifier to amplify microwave signals after pulse shaping and switching.
- **Narda 4216-20** -20dB directional coupler to pick off and analyze both the microwave input and output power to and from the SiC sample.
- **Herotek DZM185AB** Schottkey diode used to monitor ac MW pulse power via rectification. The diode is typically connected to the -20dB pickoff signal from the Narda 4216-20 directional coupler.

4.2.2 Collection electronics

Collection electronics are used to route voltage pulses from the SNSPD to the DAQ system for data collection and post-processing.

- **National Instruments USB 6343 DAQ** for rapid counting and acquisition of voltage pulses from the SNSPD. DAQ data is sent to a server that is accessed by a computer.
- Two **Minicircuits ZASWA-2-50DR** microwave switches. One switch is responsible for gating counts from the SNSPD to the DAQ (Readout ZASWA in Fig. 4.10). A second switch is responsible for routing those counts to different input channels on the DAQ to discern between counts collected during different phases of an experimental sequence when differential measurements are performed (Differential ZASWA in Fig. 4.10). These switches are also powered by a **BK Precision 1550 DC Power Supply**. Unused ZASWA outputs should be terminated with a 50Ω cap to prevent unwanted microwave reflections.

4.3 Cryogenics

Because the divacancy's optical fine structure is only well-resolved at low temperature [16], cryogenics are necessary for useful divacancy operation. Typical divacancy characterization setups use Montana closed-cycle cryostats to cool the SiC chip down to 4 to 5 Kelvin. The SiC chip is typically glued and wirebonded to a PCB for microwave manipulation. The PCB is then mounted to the 4 Kelvin stage of the Montana such that the chip is externally visible via a vacuum window made out of NBK glass. This window allows optical access for laser excitation of the sample. Piezo controllers inside the Montana can also be used for fine tuning the location of the sample with respect to the window.

Although Montana cryostats are known for being user friendly, there are a host of issues that can occur while cooling down. Dirty o-rings may cause small leaks that cause the inside of the cryostat to become covered in ice, hindering the ability to image the sample. If any component mounted to the 4 Kelvin stage touches the warmer stages or the radiation shield, which is at room temperature, the sample may fail to cool and the optical fine structure may not be resolvable. This kind of thermal touch is usually fairly easy to diagnose because the

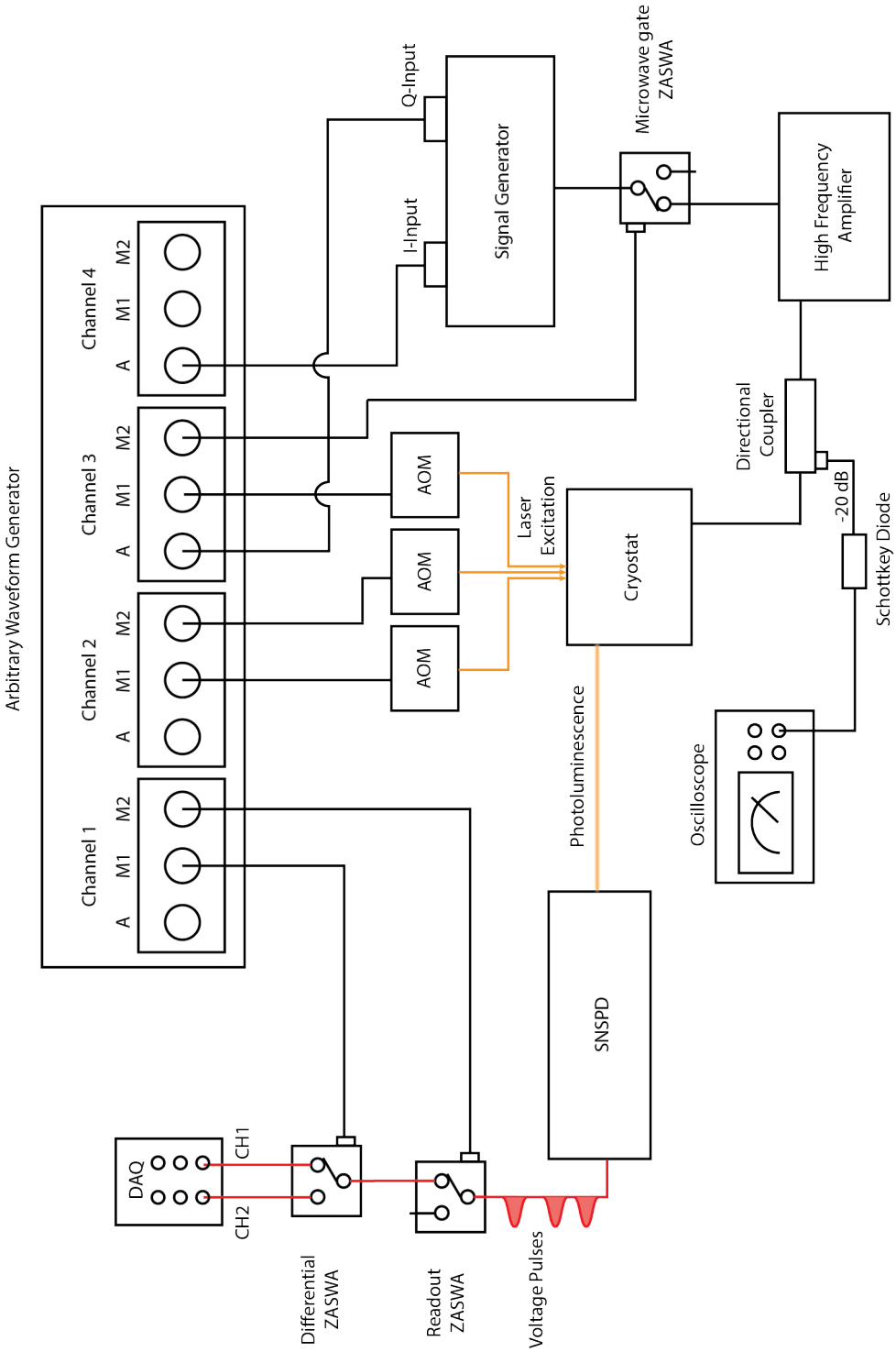

Figure 4.10: Typical electronics configuration for divacancy characterization setup. The arbitrary waveform generator (AWG) has four channels, each with a single analog (A) output and two digital marker (M) outputs.

outside of the cryostat will become covered in ice. Finally, if the microwave power delivered to the sample is too high, heating of the sample may occur and cause a jump in temperature. Thermal expansion of the sample may cause the defect to drift relative to the focus of the objective, and realignment may be necessary.

Chapter 5

Single-shot Readout of Single Divacancies using Spin-to-Charge Conversion

Despite our fairly sophisticated theoretical understanding of divacancy physics and the experimental techniques used to probe these physics, the reality is that divacancies and solid state spin defect-based systems in general need to overcome key hurdles in order to viably integrate them into distributed quantum networks. While some may argue for extending coherence, deterministic defect formation, or developing complex sensing schemes, none of these capabilities are useful unless the qubit can be clearly read out. This brings us to the crux of this thesis, which is the pursuit of single-shot readout of single divacancies in SiC, ultimately made possible by the advances developed in [1]. To fully appreciate the work laid out in [1], a solid understanding the of both "fidelity" and "contrast" is of the utmost importance. We start with a discussion of those concepts here in the context of divacancy readout.

5.1 Readout fidelity and contrast

Fidelity: As its latin root suggests, fidelity can be thought of as the confidence with which one can trust the information carried in a signal. From the perspective of quantum information, fidelity is the experimental probability of measuring a qubit to be in the state it was intended to be prepared in, or the likelihood that one qubit state will pass a test to identify as another qubit state. Given two pure states ρ and σ, fidelity is given by their overlap $F = |\langle\rho|\sigma\rangle|^2$ where a high level of overlap corresponds to high level of fidelity between the states. Identification of the causes of qubit infidelity is complex because sources of infidelity introduced during the preparation, control, and measurement processes will often present in identical ways during qubit readout. For example, it is impossible to distinguish whether a qubit state was prepared poorly or whether it was read out incorrectly. These types of errors are called state preparation and measurement (SPAM) errors. Separate from SPAM errors, the qubit state may undergo computational errors such as decoherence or relaxation due to T_1 and T_2 type processes. However, we know that we have a high level of initialization and control of single divacancies (meaning "P" part of "SPAM" is negligible) and we also have a fairly good handle on ways to characterize and address T_1 and T_2 type processes. The true glaring source of infidelity is the "M" part of "SPAM" due to spin-flips out of the excited state (see Section 2.0.6) during defect spin state readout. These spin flips cause a defect that should be in a bright state to register as being in the dark state, and vice versa, meaning that the readout cannot be fully trusted.

Contrast: The contrast of a qubit is the degree to which the signal from its two states is distinguishable. For example, for two states $|HI\rangle$ and $|LO\rangle$, the contrast between the signal S from the two states is given by:

$$C = \frac{S_{|HI\rangle} - S_{|LO\rangle}}{S_{|HI\rangle}}$$

In optically-active spin defects, the measured signal S is given by the photoluminescence rate associated with $m_s = 0$ and $m_s = \pm 1$, and contrast is often determined using differential pulse sequences (see Section 3.3). While near unity contrast is desirable, the reality for most divacancy experiments is that contrast is hindered by SPAM errors, poor collection efficiency, and readout infidelity.

Contrast vs. fidelity: A useful way to distinguish between contrast and fidelity is to consider a photon binning experiment where statistics are collected on the frequency with which some number of photons are collected per readout window from a divacancy prepared to $|0\rangle$ or $|1\rangle$. The signal from the two states will be distributed about two levels N_0 and N_1. In this picture, contrast can be thought of as how far apart those photon number distributions are, while fidelity is their degree of overlap (Fig. 5.1). Experimentally, it is necessary to have a high degree of both fidelity and contrast. Even with near-perfect fidelity, if contrast is low, the margin of error to discern between two states may not be sufficient to account for factors such as limited detector sensitivity and background noise. Alternately, if contrast is high but fidelity is low, the measured value cannot be decisively linked to the qubit state that it heralds. In other words, the measurement cannot be trusted. Notably, poor contrast and fidelity may stem from the same root cause. For example, improper initialization of a divacancy to $m_s = 0$ due to an insufficiently long resonant laser initialization pulse will increase SPAM errors while also reducing contrast because some percent of the time, the spin is not polarized to the bright state, therefore causing the average amount of photoluminescence to be lower.

5.2 The need for single-shot readout

Typical divacancy measurements require averaging over thousands of experiments to determine what the spin state is after a particular experimental sequence. This act of averaging essentially takes a quantum measurement and makes it a classical one, which kind of defeats

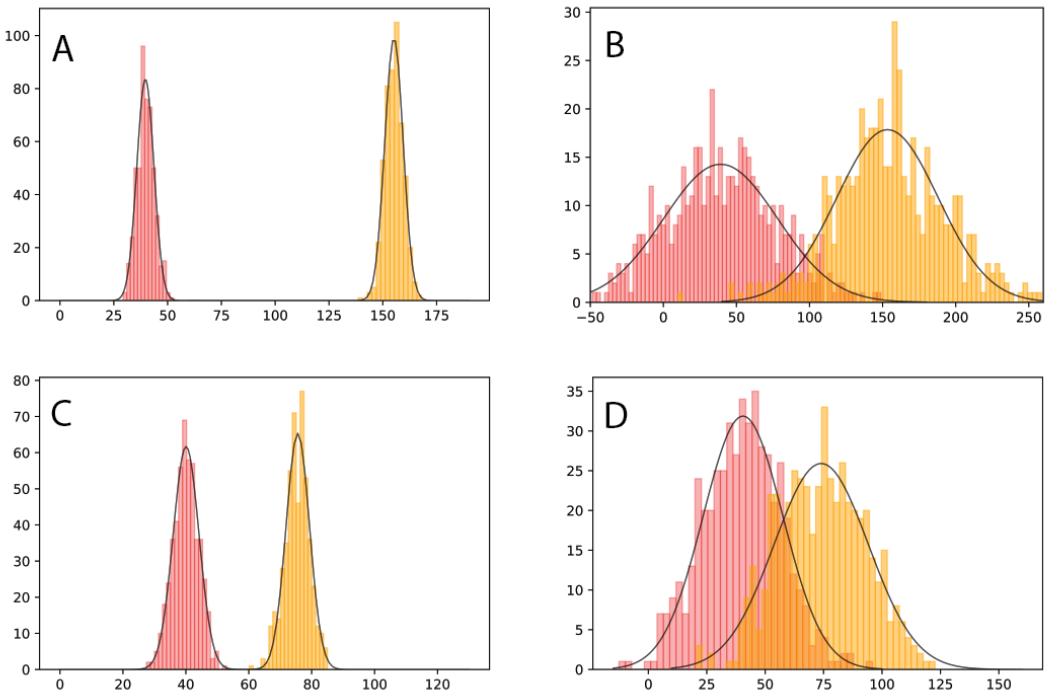

Figure 5.1: Fidelity versus contrast. The abscissa represents the photons collected per readout window (per shot) and the ordinate axis represents the frequency with which those events occur. For two distributions of data corresponding to preparation and measurement of two different states, having both high fidelity and high contrast is desirable, although one does not connote the other. **(A)** and **(C)** both have high fidelity due to minimal overlap of the distributions, but **(A)** has higher contrast and is therefore more desirable. **(B)** and **(D)** both have low fidelity due to large overlap between the distributions, but **(B)** has higher contrast than **(D)**.

the whole point of having a qubit. The reason why averaging is needed in the first place is because we often do not have enough signal (photons) to trust our measurements. Single-shot readout (SSR) means that the signal from the defect is high enough that the need for averaging is eliminated and qubit state can be determined within a single optical readout pulse. SSR is a necessary aspect of qubit operation because it enables a wide variety of quantum applications—it is used to verify spin-photon entanglement in quantum communication schemes [12] and is needed for implementation of quantum repeaters [40] and error correction schemes with nuclear registers [41–43].

The metrics used to determine whether SSR has been achieved are flexible because SSR has no inherent requirements relating to the contrast or fidelity of a system, besides the fact that more than one photon must be collected per shot. Thus, the SSR capabilities of defect-based system are often reported as the threshold number of photons (N) needed to distinguish the dark qubit state from the bright qubit state (contrast) and the fidelity associated with that cutoff. For a single-shot cutoff of N=1 photons, if on average only 2 (0) photons are collected per shot from the bright (dark) state with 100% fidelity, then the system is said to have single-shot readout with 1 photon per shot. However, the problem here is that it is not experimentally practical to consistently distinguish between zero and one photons, which is very low contrast. On the other hand, if 500 (400) photons are collected per shot from the bright (dark) state, but with a collected photon distribution overlap of 50% when the cutoff is set to N=550, that system is also be said to have single shot readout with 50% fidelity. However, if 550 photons are measured during a readout window, the state which was measured is unclear. Thus, SSR is somewhat of an arbitrary descriptor although it is generally implied that a system reported to have single-shot readout has a high level of both contrast and fidelity, and that at least one photon is collected from the bright state.

SSR capabilities vary drastically amongst existing qubit platforms. In the world of quantum dots, SSR performed with single charge sensors has been possible since the early 2000s [44] and is now a mainstay of the field. For superconducting transmons, SSR is commonly

performed using non-linear resonators that amplify microwave readout of the qubit [45], highlighting the beauty of harnessing well-developed microwave electronics and fabrication techniques. Optically-active qubits tend to pose a challenge for SSR because photon collection is an inherently lossy process and some qubits with extremely desirable coherence properties may be poor emitters. For example, rare earth ions exhibit extremely stable and narrow optical lines, but lack intrinsic cycling transitions and require cavity enhancement to collect sufficient signal.

How then do we achieve SSR for the neutral divacancy in SiC? These defects are fairly bright emitters due to their short excited state lifetimes and high cyclicity, so in theory there should be plenty of signal to go around. However, the crux of the issue is that we have a limited window during which we can collect photoluminescence from the divacancy before a spin-flip occurs, and not a lot of those photons that *do* count make it through to our detectors because confocal collection efficiencies are so bad. In other words, our fidelity and contrast are bad. For a divacancy in bulk SiC, it is estimated that only approximately 1% of total emitted photoluminescence is collected due to the cumulative effects of Fresnel reflections, refraction, and lossy optics. These phenomena are universal for defect-based systems in general, and can be combated by boosting the amount of collected photoluminescence through photonic enhancement with fabricated devices [14] or improving the design of confocal microscope systems. At the end of the day, it's all about getting as many photons out of the defect as possible before a spin-flip occurs and information is lost!

5.3 Context of experimental work

The divacancy in SiC has been a workhorse defect of the Awschalom group since the early 2010's. As the group gains more experience working with VV^0, the viability of VV^0 as a candidate for quantum communication and sensing have become even more apparent. Upon entering graduate school, there was growing excitement among the older graduate students

that it would be possible to hit milestones such as single-shot readout and entanglement with VV^0. Even now, our group's experimental work with VV^0 is at a juncture where we can perform benchmark quantum communication demonstrations that have already been done in other qubit systems, or branch off and perform exploratory work that highlights the unique strengths of qubit systems in a fabrication-amenable semiconductor. The beauty of VV^0 is that these efforts are not mutually exclusive. During the completion of my second year, research in our group showed that single VV^0 integrated into SiC diodes exhibited extremely stable, narrow optical linewidths that could be frequency-tuned under bias. At the same time, previous work performing all-optical spin-to-charge conversion of the NV^- in diamond via two-photon ionization set a precedent for attempting to do the same with VV^0. Combining this technique with the SiC diode work, the prospects of performing charge conversion of single VV^0 in a charge-sensitive SiC electrical device generated a lot of excitement in the group. It was within this context that I began the bulk of my graduate research. The experimental work I conducted has been aimed at harnessing SiC fabrication and growth capabilities to facilitate developments that will make VV^0 a truly scalable, field-deployable quantum platform.

The initial aim of the experimental work presented in this chapter was to perform electrical single-shot readout (SSR) of a single VV^0 via spin-to-charge conversion (SCC) by performing two-photon ionization of the defect in a SiC avalanche photodiode (APD). This is a mouthful and, as is always the case in research, the initial idea was (and still is) highly ambitious. Our hope was to induce avalanche breakdown of a SiC APD device through spin-dependent generation of a single charge from a divacancy, which could then be detected as an electrical signal. While electrical readout of divacancy spins is still an ongoing project, this section is comprised of the the intermediate successes and discoveries made along the way.

Many challenges presented themselves during initial experiments. SiC p-i-n mesa structures were fabricated in-house with the aim of improving current distribution through the

sample and increasing the chances of reaching avalanche breakdown in the diode. While fabricating isolated mesas certainly did reduce the amount of leakage current in reverse bias compared to bulk p-i-n samples, these structures suffered from a multitude of limitations. Two sets of devices were made from electron irradiated p-i-n SiC samples consisting of both a $1\mu m$ and $10\mu m$ intrinsic layer. While the thinner i-type layer in the $1\mu m$ sample would have been preferable for voltage tuning, narrowing, and reaching avalanche breakdown at lower applied biases, no single defects were identified due to the incredibly narrow region of interest. In contrast, the $10\mu m$ sample contained numerous defects, but those defects did not display the level of linewidth narrowing seen in the bulk p-i-n sample used in the previous diode studies [17]. In addition, avalanche breakdown was never successfully identified in the mesa structures, and attempts to reach Geiger mode often resulted in irreversible damage. Perhaps most importantly, spin-to-charge conversion via two-photon ionization was never fully realized in these mesa samples. The contrast between spin states never increased past approximately 30%, regardless of the applied bias, the wavelength of the ionization laser, or the pulse sequence duration and ordering. Many different lasers were swapped out in the confocal setup in the hopes of finding a magic frequency at which spin-to-charge conversion would work, but with little success. Ultimately we concluded that the all-optical spin-to-charge conversion process might be limited by material properties of the p-i-n samples, and the same spin-dependent two-photon ionization process was performed on a variety of SiC samples. Particularly high contrast SCC was observed in the isotopically purified sample used in past work [23]. While the reason behind this is still somewhat unknown, there are strong cases to be made that the slightly n-type material supplies just enough charges to support ionized states of the divacancy.

It is very important to note here that SSR via SCC is not a quantum nondemolition measurement (QND). However, SCC becomes a powerful tool for sensing schemes or any protocol that benefits from higher signal-to-noise while not having quantum non-demolition requirements. Regardless of these limitations, the longstanding hurdle of performing SSR

of the divacancy was ultimately surmounted. Although these results are not exactly what I had initially envisioned, I believe they bring the divacancy in SiC to the forefront as an extremely robust system that is ripe with opportunities to combine classical electronics with quantum capabilities.

5.4 Five-second coherence of a single spin with single-shot readout in silicon carbide

Solid-state defect spins hold promise for use in quantum information processing, sensing, and communication because of their unique combination of long coherence times [8, 19, 24, 46], a spin-photon interface [10, 18], and the availability of nuclear registers for use as robust quantum memories [23, 47]. The neutral divacancy (VV^0) in SiC boasts these features with the added advantages of the SiC material platform, including wafer-scale commercial availability, CMOS compatibility, and the ability to fabricate hybrid photonic [14, 48], electrical [17], and mechanical devices [22, 49].

Typically, for optically active defects spins, single-shot readout is performed through spin-dependent fluorescence probed with narrow-line lasers resonant with the defect's optical cycling transitions [15, 50]. However, this method suffers from spin-flip errors due to non-unity branching ratios in the defect's optical excited state [10]. As a result, only a finite number of spin-correlated photons are scattered before destroying the state. Combined with poor collection efficiencies, the number of measured photons per shot is usually low ($N<<1$) unless photonic devices are used to enhance emission and collection. As such, a key hurdle for the divacancy system to date has been the ability to perform single-shot readout of the defect's spin state [51]. This single-shot readout unlocks the ability to perform the entanglement distribution [12] and quantum error correction [52] needed to make quantum networks a reality and provides an increased signal-to-noise ratio for quantum sensing.

Another avenue towards single-shot readout is spin-to-charge conversion (SCC), which

maps the defect spin state onto a robust, long-lived charge state. For isolated single defect spins, SCC is an all-optical technique that has been used to achieve high-fidelity single-shot readout, but has thus far been limited to demonstrations using the NV^- center in diamond [53, 54]. In this work, we demonstrate the first ever implementation of SCC for VV^0 in SiC by performing spin-selective ionization followed by all-optical single-shot readout of the charge state. Using this technique, we can determine an initially prepared spin state with over 80% fidelity. We note that in this work, we do not pre- or post-select the charge state or resonance condition, a common strategy used to artificially boost fidelity at the cost of success rate [50, 53, 54]. Critically, we also achieve this readout in the absence of photonic enhancement, demonstrating the value of SCC to other systems where nanofabrication remains a challenge, or where detector technologies may be limited. Additionally, we deepen our understanding of the SCC process for the VV^0 defect with ab initio DFT calculations that clarify the charge transition process, which combined with theoretical modelling, assist with further optimization of this type of readout.

The high-fidelity and single-shot readout provided by the SCC technique enable us to perform experiments that would otherwise be infeasible due to low SNR, such as when the time per experimental 'shot' becomes prohibitively long. With this advantage, we employ the SCC technique to probe the unexplored limits of the spin lifetime and coherence time for VV^0. These times fundamentally determine the divacancy's performance in future quantum architectures by limiting metrics such as quantum memory times and sensitivity for ac sensing schemes [55–57]. Here, we first establish an experimentally-limited lower bound on the spin T_1 time of at least 103 seconds for VV^0, over two orders of magnitude longer than previously reported [23]. In this isotopically purified sample, we combine the reduction of the defect's noisy nuclear environment with the use of dynamical decoupling sequences to preserve coherence [58, 59]. As a result, we measure a T_2 time of 5.3 ± 1.3 seconds, over three orders of magnitude greater than the natural Hahn-echo T_2 time [8]. These metrics establish VV^0 as a premier system with coherence times that exceed previous reports for

electron spin qubits in both natural and highly isotopically purified silicon [60, 61], diamond [62, 63], and SiC [19, 64].

The results presented in this work develop SiC-based systems as a promising platform for quantum technologies, where both deterministic readout of the spin state and long coherence times are necessary for heralded entanglement generation, high gate fidelities, and the development of network components such as quantum repeaters. This work also opens avenues that utilize the CMOS compatibility of SiC for the integration of electron spin-based systems in classical electrical devices that are sensitive to single charges.

5.4.1 Results

Optical and charge transitions of the divacancy in SiC The neutral divacancy in 4H-SiC is a deep-level defect consisting of a carbon and silicon vacancy pair. The dangling bonds from atoms neighboring these vacancies form a spin-triplet ground state [65] with spin sublevels that can be polarized and read out with laser light and manipulated with microwaves (Fig. 5.2A). In this work, we use laser light resonant with the E_x and $E_{1,2}$ spin-selective optical transitions ('resonant excitation'), corresponding to the $m_s = 0$ and $m_s = \pm 1$ spin sublevels [10], respectively (Fig. 5.2B). The divacancy spin state can be efficiently initialized to $m_s = 0$ via excitation of the $E_{1,2}$ transition, which depletes the $m_s = \pm 1$ population through optical pumping and non-radiatively polarizes into $m_s = 0$ via a spin-singlet intersystem crossing [66, 67]. In past work, spin-photon readout is performed by collecting photoluminescence (PL) scattered when pumping on one of the more cycling resonant optical lines, such as the E_x transition. However, when pumping on a single optical transition, spin-flips from the excited state [66] cause a depopulation that prevents indefinite optical readout. The finite number of photons emitted before destroying the state ultimately limits the fidelity of the spin-photon readout technique.

As an alternative to readout via the spin-photon interface, the divacancy hosts robust charge states [26] that can be manipulated and read out using laser light [17, 68, 69]. In

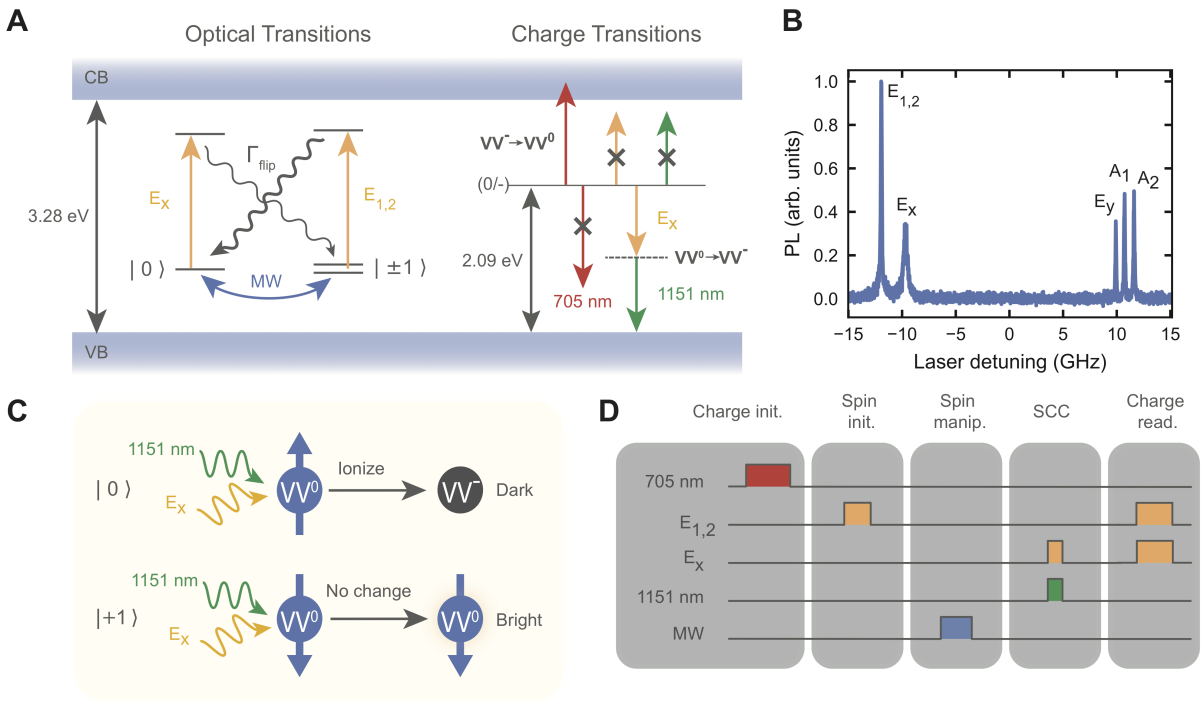

Figure 5.2: Control and readout of spin and charge states of the divacancy. **(A)** Optical and charge transitions of the divacancy. Excitation of the E_x and $E_{1,2}$ spin-selective optical transitions is performed using 1131-nm light (yellow). Spin-flips (Γ_{flip}) prevent indefinite readout of the spin state with laser pumping. Microwave (MW) manipulation is used to induce ground-state spin-sublevel transitions. SCC is performed by excitation of the E_x transition followed by an ejection of a hole by the 1151-nm ionization laser (green). The dashed line represents the VV^0 excited state. The 705-nm light (red) resets the divacancy from VV^- to VV^0. The individual lasers used for SCC and charge resetting do not have enough energy to induce other charge transitions via a one-photon process (denoted by an "X"). **(B)** PL excitation spectrum of a single divacancy reveals its six spin-selective optical transitions at T=5 K and B=18 G with continuous microwave driving of the $m_s = 0 \leftrightarrow m_s = +1$ transition. Detuning is relative to a center laser frequency of 265.1408 THz, and the transverse strain splitting is 9.78 GHz. The E_x and E_y optical transitions are $m_s = 0$ character, while the E_1, E_2, A_1, A_2 transitions are $m_s = \pm 1$ character [10]. **(C)** Mapping of the spin state onto the charge state. Pumping of the Ex transition allows for ionization of $m_s = 0$ with the 1151-nm laser. The SCC step is followed by charge readout via pumping of both the E_x and $E_{1,2}$ transitions. Detection of PL signifies that the divacancy is in its bright, neutral (dark, ionized) state and therefore was prepared to $m_s = +1$ ($m_s = 0$). **(D)** Typical experimental pulse sequence. After the charge and spin initialization and microwave manipulation of the spin state, single-shot readout of the spin state is performed with SCC followed by readout of the charge state.

this work, we use the fact that non-neutral states of the divacancy do not appreciably photoluminesce under resonant excitation that is tuned to the neutral state's zero-phonon line (ZPL). When the optical lines corresponding to both $m_s = 0$ and $m_s = \pm 1$ of VV^0 are simultaneously pumped ('charge readout'), the emitted PL does not reflect the spin state but rather whether the defect is in the neutral state or not, provided the lasers are on resonance. Thus, a reduction in PL distinguishes 'dark' ionized states from the 'bright' neutral state (Fig. 5.2C), as the optical lines are stable in this sample. For the VV^0 in SiC, this dark state has been established as the negatively charged divacancy (VV^-) [17, 27, 68, 69]. Crucially, probing the divacancy charge state with this light is not energetic enough to convert VV^- to VV^0 and vice versa via a direct one-photon process (Fig. 5.2A). The result is that non-destructive measurement of the charge state of the defect is possible with high fidelity. In this work, we also rely on deterministic preparation of the defect into the neutral charge state (VV^0). Previous reports have shown that laser light above 1.3 eV resets the charge state from VV^- to VV^0, and that light around 705 nm (1.76 eV) is extremely efficient in charge initializing the divacancy to its neutral state [17]. However, the fidelity of this process has remained unexplored to date.

Mapping of the spin state onto the charge state (SCC) via a spin-selective two-photon ionization process provides us with an avenue towards performing high-fidelity, deterministic measurement of the spin state via readout of the charge state. Here, we access the defect's excited state in a one-photon, spin-selective manner using a narrow-line laser tuned to one of the resolved optical transitions (Fig. 5.2A, Fig. 5.2B). A second 'ionization laser' (1151 nm) takes the defect from its excited state to the ionized state (VV^-) via a one-photon process by ejecting a hole [70]. We select the ionization laser wavelength based on the results of DFT calculations we perform for the VV^0 charge transition energies, which for the (0/-) transition is calculated to be 2.09 eV, in good agreement with previous work [65, 70]. The ionization laser (1151 nm) is red-detuned from the defect's ZPL (1131 nm) so as not to excite any optical transitions, while still providing enough energy to ionize the defect from the excited

state, as the combined energy of these photons (2.17 eV) enables the 2.09 eV (0/-) charge transition [26, 70] to occur (Fig. 5.2A). Specifically, we go beyond this estimate based on the charge transition levels and directly compute using DFT the energy required to go from the VV^0 optical excited state to the VV^- state with a hole at the valence-band maximum. Our DFT calculations show that photoionization from the excited state requires 1.03 eV, an energy that is slightly less than the calculated ZPL of 1.196 eV, in good agreement with experimental results (Supplementary Materials). This means that we can use a narrow, low-power resonant laser tuned to a single optical transition to provide spin-selectivity alongside a high-power, red-detuned ionization tone to induce, in total, a two-photon spin-dependent ionization of the defect.

Once we have spin-selectively mapped the spin onto the defect's charge state with the SCC step, we can then perform single-shot readout of the charge state by addressing the defect with both E_x and $E_{1,2}$ resonant light and collecting PL (Fig. 5.2C). Thus, we are equipped with a full suite of techniques to initialize the charge and spin state on-demand, manipulate the spin with microwave pulses, convert the spin state to a charge state, and perform charge readout with these lasers and controls (Fig. 5.2D).

5.4.2 Charge control and readout

We first demonstrate the robustness of the divacancy charge state and our ability to perform single-shot, high-fidelity optical readout of this state. We characterize the longevity of the VV^0 charge state with a sequence consisting of a 705 nm charge initialization pulse, a variable delay, and an optical charge readout from which we extract a charge lifetime $\tau_{ch} = 6.9 \pm 0.9$ s (Fig. 5.3A) (Supplementary Materials). The finite duration of the charge lifetime when the defect is not under illumination is likely due to diffusion of charges from nearby shallow nitrogen donors, as the material is slightly n-type (Materials and Methods). The charge lifetime is a critical timescale that dictates the longest permissible time during an experiment where the neutral defect, and therefore the spin, remains stable. Thus, the charge

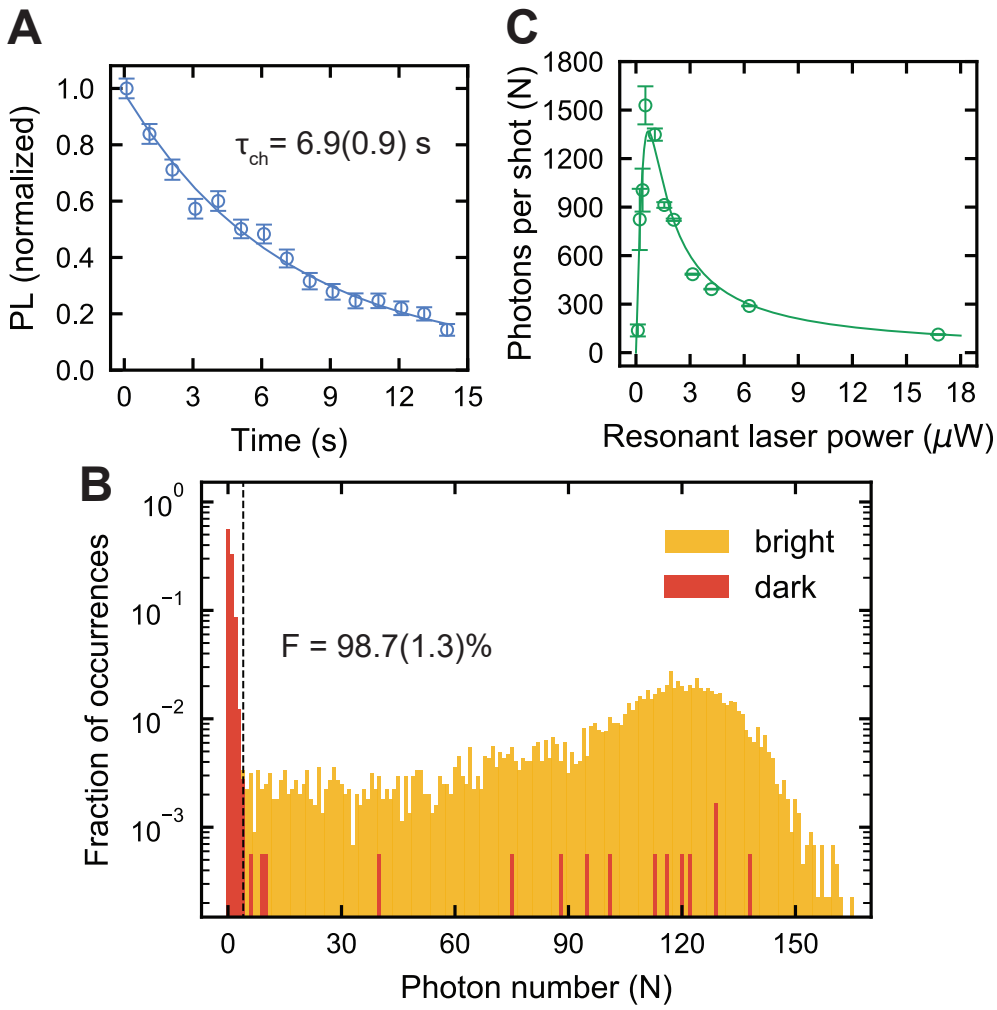

Figure 5.3: Single-shot readout of the divacancy charge state. **(A)** Charge readout PL signal dependence on delay time between the charge initialization and readout follows an exponential decay $e^{-t/\tau_{ch}}$, where τ_{ch} is the charge lifetime. We find that τ_{ch} is 6.9(0.9) s. **(B)** Log-scale histogram of photon number distributions collected during a charge readout for preparation into the neutral bright state and ionized dark state. We use a 20-ms readout window with 4.05μW combined resonant laser power, selected to maximize the readout fidelity. For a cutoff of N = 4 photons, the single-shot readout fidelity of the charge state is 98.7(1.3)%. The false-positive rate $p_{0|1}$ =1.17%, and false-negative rate $p_{1|0}$= 1.26%. **(C)** Extracted photons per shot from observed PL rate and charge state decay for various combined resonant laser powers. The maximal extracted photons per shot is N= 1529(117). The line is a fit from a model (Supplementary Materials). All data are taken at B = 18 G and T = 5 K. All reported errors represent 1 SE from the fit, and all error bars represent 1 SD of the raw data.

lifetime ultimately limits the qubit's lifetime and is a stringent cutoff for sensing and memory applications. Fortunately, previous work has shown much longer charge lifetimes [68], where future tuning of the Fermi level or balance of deep traps in the material may extend our measured timescale by many orders of magnitude. Interestingly, this charge instability is also linked to our ability to optically ionize the defect on-demand, representing a tradeoff to be optimized in future materials design. Our measured charge lifetime, however, is still many orders of magnitude longer than the saturated spin-flip lifetime, which we measure to be 3.3 ± 0.1 μs (Supplementary Materials), resulting in a longer possible readout window and more scattered photons before destroying the state.

We next demonstrate our ability to perform single-shot readout of the charge state. First, we either charge-initialize to the bright state using a long, 705 nm laser pulse or spin-agnostically initialize to the dark state using an 'ionization pulse' where both E_x and $E_{1,2}$ resonant lasers and the 1151 nm ionization laser are simultaneously turned on. This preparation into either the bright or dark charge state is followed by optical charge readout. Fig. 5.3B displays the number distribution of photons collected during the charge readout step for both the prepared bright and dark initial state. We calculate that for preparation into the bright (dark) state the mean photon number is N=100 ± 1 (N=1.3 ± 1.1) (Supplementary Materials). We determine that for a cutoff of N=4 photons, the fidelity, F_{charge}[71] is maximized at $98.7 \pm 1.3\%$ (Supplementary Materials), representing the total fidelity of our ability to prepare and readout the defect's charge state in a single shot. Despite the absence of solid-immersion lenses and other photonically enhancing structures, we achieve a high number of photons per shot. The non-unity fidelity likely arises from imperfect charge state preparation due to optical excitation of nearby traps, as we discuss in the following sections. The high single-shot photon number and the near-unity fidelity of the charge readout technique exemplify its advantage over traditional spin-photon readout.

Fig. 5.3C shows the projected number of photons per shot during these charge readout windows using various resonant laser powers. With increased laser power, more photons

are scattered per second, but additional two-photon ionization occurs, reducing the time during which the charge state can be read. On the other hand, if the laser power is too low, very few photons per second are scattered but readout time is still limited by the charge lifetime and the readout window cannot be arbitrarily extended. As a result, there is an optimal choice of laser power to maximize the readout, which in our case results in over 1500 photons per shot at $\sim$1 μW. This behavior is understood with a simple predictive model (Supplementary Materials). The high number of scattered photons means that single-shot readout of the charge state is possible even with extremely low collection efficiency or in systems with much lower quantum yield.

Having established our ability to perform high-fidelity single-shot readout of the charge state, we next characterize the various charge transition processes induced by the lasers used in our experiments. We first characterize the rate at which we initialize the divacancy to the neutral state with the 705 nm charge repump laser. After preparing the defect in the dark charge state, a time-varying charge initialization pulse is applied to reset the defect to the neutral, bright state. Using a charge readout, we measure the recovery rate of the bright state as a function of the 705 nm laser power (Fig. 5.4A). The charge repump rate is 993 ± 17 MHz/W, consistent with the one-photon repumping rate described in [17].

We next characterize the ionization rate solely from the resonant lasers and ionization laser, respectively, by initializing into the bright state and measuring the charge state after a variable length laser pulse. The exponentially fit ionization rates for various powers of the resonant lasers are displayed in Fig. 5.4B. The ionization rate is initially quadratic and then increases linearly as 10.6 ± 0.9 MHz/W, signaling saturation of the optical transition (Supplementary Materials). At the relevant resonant laser powers in our experiment, we observe ionization rates around 100 Hz. On the other hand, ionization from solely the 1151 nm laser increases linearly with power as 95.7 ± 3.7 kHz/W (Fig. 5.4C). Ideally, the 1151 nm laser by itself should cause no ionization, where here a small residual rate likely arises from excitation of nearby traps, freeing carriers that alter the defect's charge state.

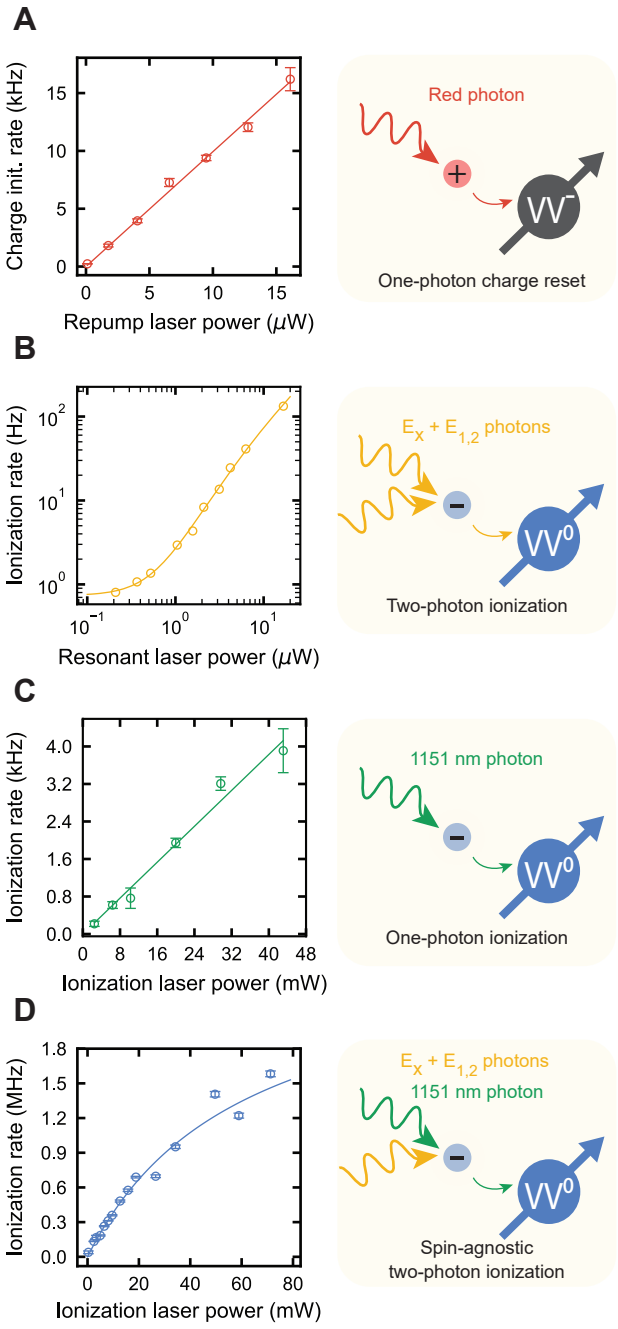

Figure 5.4: Optical charge reset and ionization processes. **(A)** Power dependence of the charge reset rate using the 705-nm laser. The reset rate is linear (red line fit) with power as 993 ± 17 Hz/μW. **(B)** Ionization rate dependence on combined reso-nant laser power (E_x and $E_{1,2}$ lines). The solid line is a fit using a saturating two-photon ionization model (Supplementary Materials). **(C)** Ionization rate dependence on 1151-nm laser alone. The ionization rate is linear with power (solid line fit) as 95.7 ± 3.7 kHz/W. **(D)** Spin-agnostic ionization rate dependence on the 1151-nm laser ionization power. The resonant laser excitation is beyond saturation at 15 μW.

Figure 5.4: The solid blue line is a fit from our model including the effect of stimulated emission (Supplementary Materials), where the low-power ionization rate is 37.4 ±0.7 MHz/W. All data are taken at B = 18 G and T=5K. All reported errors represent 1 SE from the fit, and all error bars represent 1 SD of the raw data.

Finally, we characterize our ability to ionize the defect once it is in its optical excited state, which is the prerequisite for spin-dependent ionization. After charge initializing to the bright state, we spin-agnostically ionize the defect using a variable length pulse where both the E_x and $E_{1,2}$ resonant lasers and the 1151 nm ionization laser are on at the same time. For these experiments, the resonant power is kept such that the defect optical transition is saturated. The decay rate of the signal from charge readout is displayed for various ionization powers in Fig.. 5.4D, where the saturating behavior can be understood through the effect of stimulated emission, discussed later (Supplementary Materials). Importantly, the spin-agnostic ionization rates (order MHz) are nearly three orders of magnitude greater than the unwanted ionization rate from only the 1151 nm laser (order kHz) or only the resonant lasers (order 100 Hz) for the relevant powers used in our experiments. This confirms that for experiments where both resonant excitation and the 1151 nm ionization laser are used, the dominant source of ionization is a two-photon process where one photon induces a resonant, ground to excited state transition of the defect and a second photon from the ionization laser subsequently converts the defect to its negative charge state.

5.4.3 Spin-to-charge control

Given that we can perform high-fidelity, single-shot readout of the divacancy charge state, and that we can ionize the defect with a combination of resonant and red-detuned laser light, we can selectively map the divacancy spin state onto its charge state to achieve single-shot readout of the spin state. Specifically, after charge initialization to VV^0 and spin initialization to $m_s = 0$, we spin-selectively photo-ionize the $m_s = 0$ state to VV^- by simultaneous excitation of the E_x optical transition ($m_s = 0$ character) while applying the 1151 nm

ionization laser. This is the SCC pulse that results in the process shown in Fig. 5.2C. The defect can be protected from this spin-selective ionization by rotating into $m_s = +1$ via the application of a microwave π pulse so that the laser no longer optically excites it (Fig. 6.7). Thus, a spin initialized to $m_s = +1$ does not undergo ionization and remains in VV^0, forming the basis of spin contrast for the SCC process. Importantly, SCC is performed using the E_x transition due to its high cyclicity, which increases the number of times the excited state can be populated before a spin-flip occurs. Spin-flips cause destruction of the spin state [26] and prevent ionization from occurring, therefore reducing the fidelity of the conversion process (Supplementary Materials). Thus, a key aspect of the SCC process is ensuring the rate of spin-selective ionization exceeds the rate of spin-flip errors.

After SCC, we perform single-shot readout of the charge state. The charge readout signal for states prepared to $m_s = 0$ and $m_s = +1$ as the SCC pulse duration is swept is shown in Fig. 5.5A. After the SCC contrast reaches a maximum, the contrast decreases with increased spin-selective ionization pulse durations due to a reduction in PL from states prepared into $m_s = +1$. This decreasing PL is caused by non-spin selective ionization, but has a rate of decay that exceeds the ionization rate from only the 1151 nm laser (Fig. 5.4C). Therefore, we attribute this non-spin selective ionization to other mechanisms such as weak excitation of the $m_s = \pm 1$ optical transitions by the E_x laser, or heating effects induced by the high-power ionization laser that cause additional orbital or spin mixing.

We next characterize the end-to-end fidelity of the combined initialization, SCC, and readout process by examining the resulting single-shot photon number distribution. Fig. 5.5B shows histograms of the photon statistics for states prepared into $m_s = 0$ and $m_s = +1$. We extract a maximum end-to-end SCC fidelity of F_{SCC}=80.8 $\pm$ 0.6% (Supplementary Materials). When corrected for the charge initialization and charge readout fidelity, we obtain a SCC conversion fidelity of $F'_{\mathrm{SCC}} = F_{\mathrm{SCC}}/F_{\mathrm{charge}}$=81.6%, revealing that the main source of infidelity is the SCC conversion process and not the charge readout. We eliminate infidelity arising from errors in spin manipulation and selectivity of the spin-photon interface,

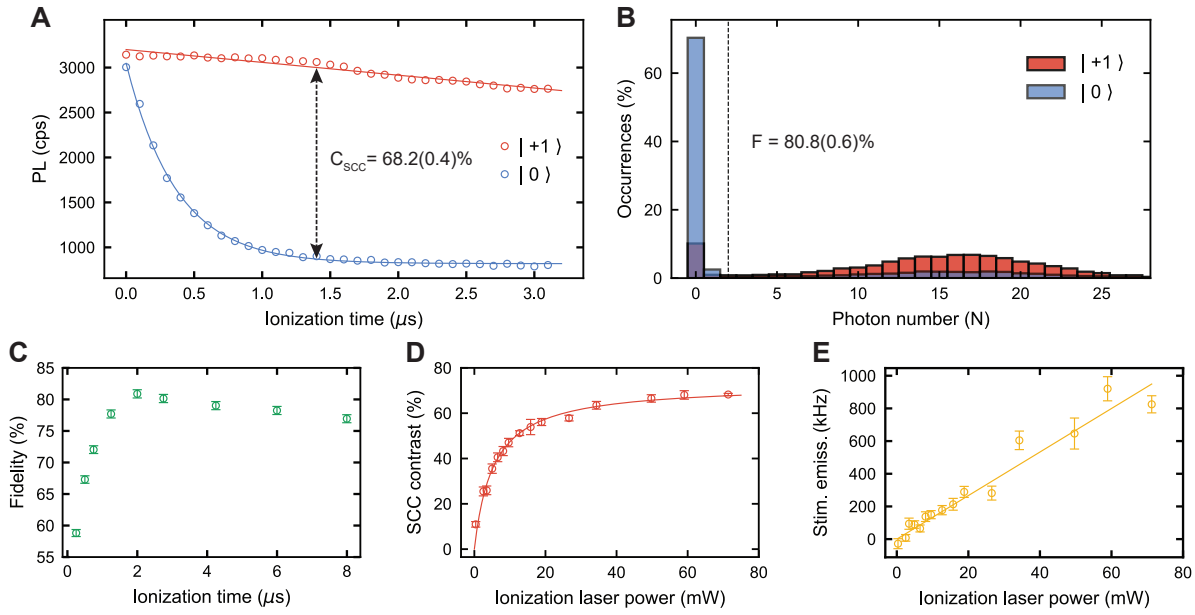

Figure 5.5: Single-shot readout of the spin state with SCC. **(A)** Charge readout signal following SCC step for preparation into $m_s = 0$ and $m_s = +1$. The maximum fitted contrast is 68.2(0.4)% at an ionization laser power of 71 mW and a SCC pulse duration of t_{ion} =1.39 μs using 14.95 μW of resonant power. cps, counts per second. **(B)** Charge readout photon number distribution after SCC step for preparation into $m_s = 0$ and $m_s = +1$. The end-to-end process fidelity is 80.8(0.6)% for a cutoff of N = 2 photons. **(C)** Dependence of SCC fidelity on SCC pulse duration. **(D)** Dependence of SCC contrast with 1151-nm ionization laser power. The contrast follows a saturation behavior (red line fit; Supplementary Materials). **(E)** Calculated stimulated emission rate dependence on 1151-nm ionization laser power. The stimulated emission rate increases linearly as 13.3 MHz/W (yellow line fit). All data are taken at B = 18 G and T = 5 K. All reported errors represent 1 SE from the fit, and all error bars represent 1 SD of the raw data.

due to our observation of over 99% Rabi contrast in fluorescence readout, consistent with previous reports [23]. This fidelity is greater than the SCC contrast (Fig. 5.5A) due to non-zero background counts and appreciable ionization during the readout window. We track the SCC end-to-end fidelity (F_{SCC}) while sweeping the SCC pulse duration (Fig. 5.5C) and find that fidelity is maximized for a pulse duration of approximately 2 μs. We note that in Fig. 5.5B, there is significant population distribution above and below the N=2 single-shot cutoff for both spin preparations, corresponding to a false positive rate $p_{0|1}$=27% and false negative rate $p_{1|0}$=11%, for $m_s = 0$ and $m_s = +1$, respectively (Supplementary Materials). This indicates that incomplete ionization of $m_s = 0$ is the dominant source of infidelity in our SCC process, which we discuss below.

Although we increase the ionization laser power to maximize SCC contrast and fidelity, we observe that the SCC contrast (C_{SCC}) unexpectedly saturates with power (Fig. 5.5D), limiting our single-shot readout fidelity. We attribute this saturation behavior to stimulated emission from the excited state induced by the 1151 nm ionization laser [72]. Stimulated emission induces an excited to ground state transition of the defect, effectively increasing the spin-flip rate and decreasing the occupation time in the excited state. This results in a reduced chance of ionization via SCC before a spin-flip occurs, and manifests as the saturating behavior seen in Fig. 5.5D. We model the dynamics of the SCC process using a set of differential equations to describe the various rates of ionization and spin-flips in our system (Supplementary Materials). Using the measured spin-agnostic ionization rate (Fig. 5.4D), the spin-flip rate, and the time evolution of Fig. 5.5A, our model predicts a maximum SCC fidelity of about 72%, which is consistent with our experimental findings. The reduction in the excited state lifetime due to stimulated emission reduces the occupation of the excited state and lowers the ionization rate, which also explains the behavior seen in Fig. 5.4D. Finally, by subtracting the spin-agnostic ionization rate (Fig. 5.4D) and the spin-flip rate from the SCC rate (Fig. 5.5A), we extract the stimulated emission rate. This rate is shown as a function of the ionization laser power in Fig. 5.5E (Supplementary Materials).

Importantly, we find that the simple ratio of the ionization cross section from the excited state to the stimulated emission cross section (σ_i/σ_s) determines the resulting fidelity of SCC, where larger ratios are desirable. We directly calculate this metric with DFT, which indicates that the ratio is only optimal for a narrow energy window below the ZPL energy and above the energy of the first vibronic peak in the emission sideband (Fig. 6.4B, 6.4D). Our theoretical results also show that the cross sections and the ratio σ_i/σ_s do not change as a function of the light polarization when the incident light is parallel to the threefold rotation axis (C_{3v}) of the defect (Fig. 6.5A, 6.5B). Surprisingly, however, a significant increase in the ratio σ_i/σ_s may be obtained by using polarized light perpendicular to the defect axis (Supplementary Materials). This suggests that a change in the ionization laser geometry and polarization may drastically increase the SCC fidelity. These investigations into the limitations of SCC due to stimulated emission through DFT and modelling create a set of guidelines and considerations for designing qubits and optimizing these types of spin-to-charge experiments.

5.4.4 Extending coherence with dynamical decoupling

Having demonstrated the ability to spin-selectively ionize the defect, we take advantage of the single-shot readout afforded by the SCC technique and perform measurements that reveal the exceptionally long spin coherence time of the defect's spin state. We first perform T_1 relaxation measurements using SCC readout (Fig. 5.6A). Although the charge state has appreciable decay on these timescales, we normalize our measurements such that we can extract the pure spin relaxation time. Despite no obvious spin T_1 decay in Fig. 5.6A, we investigate the T_1 time using a square goodness of fit test and place a lower bound of 103 seconds on the T_1 time with 95% confidence (Supplementary Materials). This minute-scale lower bound eliminates T_1 spin relaxation as a concern for this system, and is on par with the longest reported times for the NV^- center in diamond at equivalent temperatures [62].

In natural SiC, spin decoherence is dominated by magnetic fluctuations from flip-flop

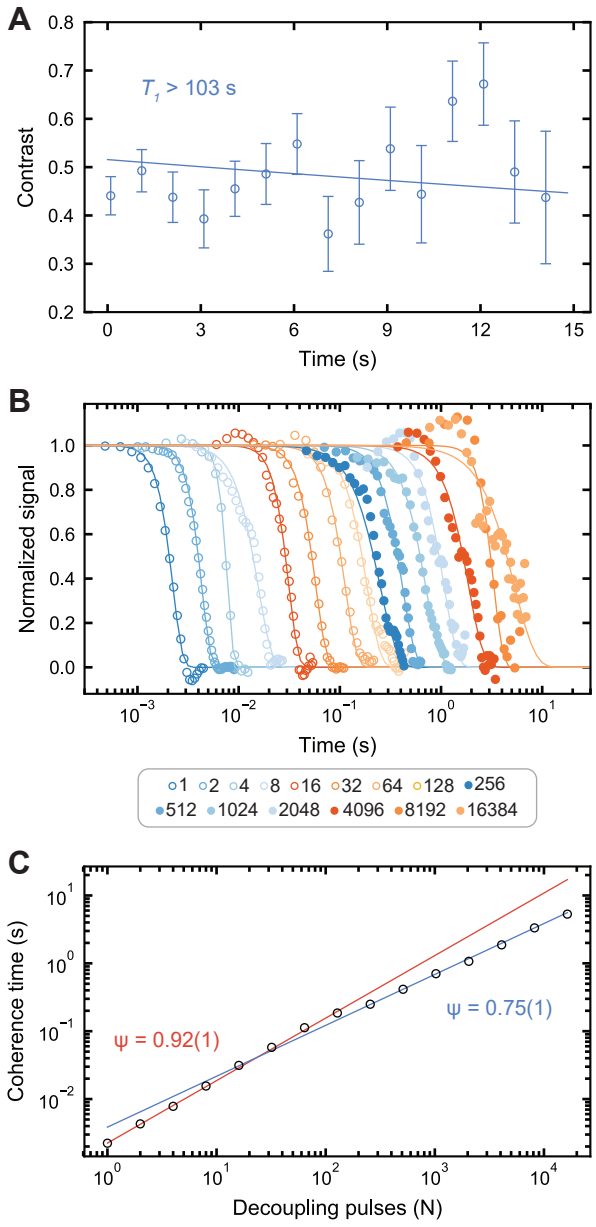

Figure 5.6: **(A)** T_1 spin relaxation time of divacancy using single-shot readout. Using a goodness of fit test with a 95% confidence interval, we estimate that $T_1 \geq$103 s (Supplementary Materials). The fit (solid line) is for a T_1 of 103 s. **(B)** T_2 decay curves measured after applying dynamical decoupling pulses sequences of increasing pulse number, N. We avoid electron spin echo envelope modulation oscillations by enforcing pulse spacing requirements as in [62], eliminating sharp dips, and smoothing to find the coherence function envelope. The envelope is fit to a stretched exponential function $Ae^{-(\frac{t}{\tau})^n}$, where n is a stretch factor. **(C)** Extension of T_2 coherence time with total decoupling pulse number. We fit in log space the low (blue) and high (red) pulse number regimes as $T_2 \sim N^{\psi}$. All data are taken at B = 18 G and T = 5 K. All reported errors represent 1 SE from the fit, and all error bars represent 1 SD of the raw data.

interactions between ^{29}Si and ^{13}C possessing I=1/2 nuclear spins [24]. The sample studied here was isotopically engineered to reduce the occurrence of nuclear flip-flops and extend the coherence time [23] (Materials and Methods). In this work, we further extend this spin coherence by applying dynamical decoupling sequences [58] (Fig. 6.8). Fig. 5.6B displays the coherence for sequences consisting of N = 1 to N = 16384 pulses, measured with single-shot readout. With the combination of isotopic purification and dynamical decoupling, we measure a maximum T_2 time of 5.3 ± 1.3 seconds, an improvement of over two orders of magnitude over the previously reported extended coherences in the divacancy system [19].

The dependence of coherence (T_2) on pulse number (N) (Fig. 5.6C) can be modeled as $T_2 \sim \psi^N$ where ψ varies with the frequency cutoff, shape, and roll-off behavior of sources of dephasing in the system [73]. We find that the scaling of coherence for low pulse numbers has $\psi = 0.92 \pm 0.01$ and at high pulse numbers $\psi = 0.75 \pm 0.01$ (Fig. 5.6C). This may suggest that dephasing is dominated by two separate noise sources, each with differing associated frequency cutoffs that dominate in different regimes [74]. The existence of these two competing noise sources is supported by previous work on the same isotopically purified sample that suggests both a fast paramagnetic and slow nuclear spin bath play a role in dephasing [23], though certain broad Lorentzian baths may exhibit a similar $\psi \approx 1$ [73] to $\psi \approx 2/3$ crossover [63]. Another possibility is that our experiments become dominated by control errors at high pulse number and do not protect the state as effectively, as we observe the contrast decreasing in this regime (Fig. 6.9).

Even after over 104 pulses, the measured coherence time does not saturate. Given the long T_1 times, we expect coherence times greater than five seconds to be possible with even longer decoupling sequences (Materials and Methods). The combination of dynamical decoupling and isotopic purification in this work results in coherences that exceed state-of-the-art single spin measurements in other competing systems [62]. These ultralong coherences offer many advantages for SiC-based quantum technologies. For example, in ac sensing protocols, long coherence times extend the phase accumulation period and increase sensitivity to weak

signals. Additionally, the reduction of memory storage errors that comes with long coherence times is vital for the development of quantum repeaters, which are a necessary component for future quantum networks.

5.4.5 Discussion

The all-optical spin-to-charge conversion technique demonstrated here can be extended to other emitters where single-shot readout is needed [75–77], particularly in platforms where the photonic devices typically used to boost collection efficiency can degrade charge and optical qualities, or where detector or emitter quantum efficiency is low. Additionally, coherence protection combined with the high-fidelity readout provided by the SCC technique brings the SiC material platform to the forefront for use in sensing and communication protocols that require both deterministic readout and quantum state preservation.

Looking forward, use of auxiliary microwave drives [54] to recover leakage of population from the qubit states, optimization of the ionization laser wavelength to maximize σ_i/σ_s, and further extension of the charge state stability via growth techniques may present pathways to improving the SCC technique. Our DFT calculations additionally suggest that a significant reduction in undesirable stimulated emission can be achieved by employing polarized light with incidence orthogonal to the defect axis, while still effectively ionizing the defect. We note, however, that the stimulated emission from defects is also of fundamental interest for future developments of lasers and new kinds of sensors [78]. Furthermore, the charge itself may lead to new sensing opportunities [79], while the use of electrical depletion can reduce some of the remaining noise in the system to further increase coherence [17, 80, 81]. Electron spin coherences in this platform could also be improved by further reducing magnetic noise through materials growth, or by operating in decoherence protected subspaces with basal divacancy defects [19].

Integration of SCC with the optical tuning capabilities offered by SiC devices, such as p-i-n diodes [17], could be used to construct highly scalable, tunable SiC quantum nodes

for future entanglement schemes. More generally, the SCC technique in SiC enables the translation of quantum spin-based information into charge-based information in a wafer-scale material with mature electronics technology. Thus, this work unlocks a new generation of devices where semiconductor structures such as MOSFETs, diodes, and APDs can be embedded with single spins to bridge the gap between quantum and classical electronic devices.

5.4.6 Materials and methods

Measurements are performed at T = 5 K in closed-cycle Montana Cryostat with a 0.85 NA near-infrared objective. All measurements are performed at low field of around 18 Gauss on a single hh divacancy in 4H-SiC. We use two Toptica DLC PRO lasers for narrow-line laser control of the defects. The 1151 nm ionization laser is a QPhotonics QFLD-1160-300S temperature tunable laser diode. PL is detected with a Quantum Opus superconducting nanowire single photon detector. Photon counting and time tagging experiments use a PicoQuant Picoharp 300 Time-Correlated Single Photon Counting (TCSPC) system. Charge initialization is achieved by applying a 705 nm light for 5-10 ms. For most experiments the 705 nm laser power is 200 nW at the sample. Spin initialization is achieved by pumping on the $E_{1,2}$ transitions, while the E_x transition serves as the cycling transition for readout and spin-to-charge conversion. When performing SCC, to mitigate the effects of this non-selective ionization, we saturate the defect with resonant laser excitation to maximize the chances of desirable spin-selective ionization during the SCC step before a charge conversion error occurs. Additionally, for subsequent experiments we utilize the highest possible ionization laser power of 71 mW to increase the likelihood of ionization during the SCC step. This maximum power is also used to perform spin-agnostic ionization when preparing into the dark, ionized state in Fig. 5.3C. Driving of transitions between the $m_s = 0$ and $m_s = \pm 1$ spin sublevels is performed using 1.357 GHz microwaves applied through Ti/Au striplines patterned on the sample surface. Microwave extinction and filtering is an important parameter to increase

coherence and lifetime. We use a 800 MHz highpass filter after amplification, and switch the microwave pulses on and off with a ZASWA-2-50DR+ both before and after amplification. Further extinction is achieved utilizing the IQ modulation of the source, which also provides phase control of the microwave pulses. We use this phase control to perform the XY-8 pulse sequences for dynamical decoupling which reduces sensitivity to pulse imperfections and drift. For all spin control experiments, we use π pulses with a length of approximately 1-2 μs. We stop our experiments at pulse number N = 16384 for CPMG due to compounding pulse infidelity that reduces contrast and because our measured coherence approaches the charge lifetime for this defect. In Fig. 5.6B, the coherence function is normalized such that the contrast reduction and the finite charge lifetime do not affect the fitted coherences.

For the coherence measurements, two fiber-coupled AOMs (AA Opto-electronic MT250-IR6-Fio-SMO) are used in series on the resonant lasers to achieve high extinction. Pulsing of the red charge reset tone (705 nm) and the 1151 nm ionization laser is achieved with direct modulation of the laser diode with a Thorlabs CLD1015 diode control unit. Extinction from this modulation is high, where we note the finite charge lifetime is not affected by extra extinction of the 705 nm laser in the off state. All parameters in the text have errors reported at one standard error (SE).

The sample consists of epitaxial 4H-SiC grown by chemical vapor deposition on a 4° off-axis n-type 4H-SiC. The layer thickness is $\sim$90 μm, and uses isotopically purified Si and C precursor gasses as in reference [23]. Secondary ion mass spectroscopy reveals purities of 99.85% ^{28}Si and 99.98% ^{12}C. C-V measurements show slightly n-type behavior with a carrier concentration of $6 * 10^{13}$ cm^3. Single defects are created using a $1 * 10^{13}$ cm^2 dose of 2-MeV relativistic electrons. Subsequent annealing at 810°C in Ar gas results in isolated single VV^0. We note that this slight n-type behavior causes VV^0 to be unstable under illumination, where the negative charge states are favored. This is key, however, to our ability to ionize the VV^0 effectively. The available carriers from these dopants provide the necessary charges to continually source and redistribute charges for these processes. SCC

naturally requires charge unstable defects.

5.4.7 Computational details

We carried out hybrid DFT calculations to determine the excitation energies of the VV^0 defect and the charge transition energy to the VV^- defect. All calculations were performed using the dielectric-dependent hybrid (DDH) functional [82] and the Quantum Espresso code [83]. We used a 5x5x2 G-centered supercell, SG15 ONCV pseudopotentials [84] and a plane-wave basis set with a kinetic energy cut-off of 80 Ry. In the case of charged defects, we applied corrections to the total energy as derived in [85]. We computed the optical matrix elements pertaining to the ionization and stimulated emission cross sections using a G-centered supercell with 1296 atomic sites and the PBE functional [86]. Electron-phonon spectral functions were computed using the generating function approach within the displaced harmonic approximation [72, 87, 88]. The phonon modes of the defective solid were obtained using a 5x5x2 supercell generated with the PHONONPY [89] package and extrapolated to larger sizes (16x16x5 supercell). Additional details are reported in the Supplementary Materials.

Chapter 6

Supplementary materials

6.1 Charge lifetime calculation

To determine the charge lifetime, the decay in the PL signal is modelled as:

$$A * e^{-t/\tau_{ch}} + y_0 \tag{6.1}$$

where A is the PL rate, y_0 is the background laser scatter and dark count rate, and τ_{ch} is the charge lifetime. From our data we find $\tau_{ch} = 6.98 \pm 0.88$ s, as shown in the fit displayed in Fig. 5.3A.

6.2 Mean photon number for photon number distribution calculation

For a normalized, discrete photon number distribution m_j, the mean value μ of the distribution is calculated as:

$$\mu = \sum_{j=0}^{len(m_j)} j * m_j \tag{6.2}$$

where j is the photon number. The error of the mean is taken to be $\sqrt{\mu}$.

6.3 Projected photons per shot calculation for charge readout

The PL signal decays over a charge readout window as:

$$A * e^{-t/\tau} \tag{6.3}$$

where A is the PL rate with units of photons/second, and τ is the decay constant in seconds. The projected photons per shot collected over the charge readout window is the integral of the decay curve from zero to infinity, which for for a given power goes as $A * \tau$. We use this expression to find the dependence of the photons per shot n_{shot} on resonant laser power p. It takes the form:

$$n_{shot}(p) = A(p) * \tau_{ion}(p) \tag{6.4}$$

The ionization rate, $1/\tau_{ion}$, follows a saturation behavior with power and thus takes the form:

$$\frac{1}{\tau_{ion}} = \frac{1}{t_0} + \frac{p * b}{1 + \frac{p_{sat}}{p}} \tag{6.5}$$

where t_0 is the charge lifetime, p_{sat} is the saturation power, and b is the ionization rate at saturation. This equation represents both the intrinsic charge lifetime decay and the two-photon ionization from a saturable two-level system. Additionally, $A(p)$ is the power-dependent PL rate which also saturates with power:

$$A(p) = \frac{c}{1 + \frac{p_{sat}}{p}} \tag{6.6}$$

where c is the photoluminescence rate at saturation and p_{sat} is the saturation power. To find $n_{shot}(p)$, we use Equations 6.5 and 6.6 to evaluate $A * \tau$:

$$n_{shot}(p) = \frac{c * t_0 * p}{p + p_0 + b * t * p^2} \tag{6.7}$$

We use Eq. 6.7 to calculate the projected photons per shot as displayed by the fit in Fig. 5.3C.

6.4 Charge repump/reinitialization rate calculation

As the duration of the 705 nm charge reset pulse increases, the PL signal for the subsequent charge readout steps grows as:

$$A * (1 - e^{-(t-t_0)/\tau_r}) \tag{6.8}$$

where A is the PL rate, t_0 is a time offset, and τ_r is the characteristic charge initialization time, from which we define the charge reset rate to be $1/\tau_r$.

6.5 Charge readout fidelity and end-to-end fidelity of SCC calculation

We take the definition of fidelity from Ref.[71] as:

$$F = 1 - \frac{1}{2}(1 - p_{0|0} + p_{0|1}) = \frac{1}{2}(p_{0|0} + p_{1|1}) \tag{6.9}$$

The convention of the notation $p_{A|B}$ used here can be interpreted as the probability of measuring A while preparing or expecting the outcome B. Here, $p_{0|0}$ is the normalized true positive probability, $p_{0|1}$ is the normalized false positive probability, $p_{1|1}$ is the normalized true negative probability and $(1 - p_{0|1}) = p_{1|1}$. Using Eq. 6.9, for a single shot cutoff of n photons, the single shot charge readout fidelity is calculated as:

$$F_{charge} = \frac{1}{2}\left(\frac{\sum_0^n p_d}{\sum_0^\infty p_d} + \frac{\sum_n^\infty p_b}{\sum_0^\infty p_b}\right) \tag{6.10}$$

Where p_d and p_b are the unnormalized photon distributions for the prepared dark and bright states, respectively. Similarly, for a single shot cutoff of n photons, the end-to-end SCC fidelity is calculated as:

$$F_{SCC} = \frac{1}{2}\left(\frac{\sum_0^n p_0}{\sum_0^\infty p_0} + \frac{\sum_n^\infty p_{+1}}{\sum_0^\infty p_{+1}}\right) \tag{6.11}$$

where and p_0 and p_{+1} are the unnormalized single shot photon number for $m_s = 0$ and $m_s = +1$, respectively. Eq. 6.11 is used to calculate the data displayed in Fig. 5.5C. In all experiments, the reported cutoff n is selected to maximize the fidelity F.

6.6 Fitting of SCC traces and SCC contrast calculation

We fit the signal of the charge readout after varying the SCC duration as an exponential decay:

$$A_i e^{-t/\tau_i} + y_i \tag{6.12}$$

where A_i and y_i are PL rates, and τ_i is the decay time constant. We calculate the contrast C_{SCC} in the charge readout between $m_s = 0$ and $m_s = +1$, denoted by the subscripts 0 and +1, after a given SCC pulse duration t_{ion} as:

$$C_{SCC} = \frac{(A_{+1}e^{-t_{ion}/\tau_{+1}} + y_{+1}) - (A_0 e^{-t_{ion}/\tau_0} + y_0)}{\frac{1}{2}(A_{+1} + y_{+1} + A_0 + y_0)} \tag{6.13}$$

The fits in Eq. 6.13 are used to calculate the contrast to better eliminate noise and to allow for better error estimation.

6.7 Chi-squared goodness of fit test to predict T_1 longitudinal lifetime

To place a lower bound on the T_1 time of the defect we perform a χ^2 test for goodness of fit by producing a χ^2-distribution comparing our data to equations of the form:

$$A * exp(-\frac{t}{T_{1,test}}) \tag{6.14}$$

We first fit the PL rate A to our collected data for a given $T_{1,test}$ value. We then calculate the χ^2 value of our test T_1 decay curve 6.14 to the data. The χ^2 value corresponding to a given test curve is calculated as:

$$\chi^2 = \sum_{i}^{k} (\frac{\chi_i - \mu_i}{\sigma_i})^2 \tag{6.15}$$

where χ_i is the measured value at point i, μ_i is the predicted value from the generated decay curve at point i, and σ_i is the standard deviation of the measured value. Here, there are $k = 15$ data points that each correspond to a different time t_i.

We use a χ^2 goodness of fit test to determine the lower bound on the T_1 value. For a right-handed test with a confidence level of 95% and 13 degrees of freedom (corresponding to the k=15 data points and 2 fit parameters), the critical chi-squared value is 22.362. We find that all chi-squared distributions generated for $T_{1,test} < 103.3$ seconds exceed this critical value. Thus, we place a lower bound estimate of 103.3 seconds on the T_1 time with 95% confidence.

6.8 Modeling the SCC process

To model the dynamics of the SCC process, we create a set of differential equations describing the rates of ionization and spin-flips in the system. We assume the orbital dynamics of the

defect are fast and average over the photon absorption and emission events, treating the population in the excited state (P_{ES}) generally in the form of a saturation curve. The saturation curve is generally in the form:

$$P_{ES}(p) = \frac{A}{1 + p_0/p} = \frac{A}{1 + \tau_{absorb}/\tau_{emit}} = \frac{A}{1 + R_{emit}/R_{absorb}} \tag{6.16}$$

with p_0 representing the power by which a photon is absorbed on average once per optical lifetime ("saturation power"). As shown above, the factor p_0/p can also be understood as the ratio of time for absorption and emission, or equivalently the ratio of emission to absorption rates. Because the spin-flip process occurs due to a set branching ratio from the excited state, the spin-flip rate (R_{sf}) depends on the excited state population and also follows a power-dependent saturation curve with respect to the resonant power p_{res}:

$$R_{sf}(p_{res}) = \frac{R_{sat}}{1 + p_0/p_{res}} \tag{6.17}$$

with R_{sat} as the saturated spin-flip rate. On the other hand, the ionization rate from the excited state (R_I) is also related to the population in the excited state times a one-photon power-dependent rate of ionization from the excited state. We denote the ionization laser power p_i, where assuming the two-photon ionization from solely the resonant laser is low:

$$R_I(p_{res}, p_i) = \frac{a p_i}{1 + p_0/p_{res}} \tag{6.18}$$

where a is the linear ionization rate per unit power. We note here that the rate from the excited state is actually $2a$, given that the excited state is only populated half of the time at saturation. With our resonant laser only pumping the highly cycling E_x transition, the spin flips deplete the $m_s = 0$ state and populate the $m_s = \pm 1$ state. This results in the following equations for the populations in the bright $m_s = 0$ (B_0), bright $m_s = \pm 1$ (B_1), and dark populations (D):

$$\frac{dB_0}{dt} = -R_I(p_{res}, p_i)B_0 - R_{sf}(p_{res})B_0 \tag{6.19}$$

$$\frac{dB_1}{dt} = +R_{sf}(p_{res})B_0 \tag{6.20}$$

$$\frac{dD}{dt} = +R_I(p_{res}, p_i)B_0 \tag{6.21}$$

We can solve Equations 6.19-6.21 assuming the system is fully initialized into either $m_s = 0$ (B_0), where $B_0(0) = 1$, or $m_s = \pm 1$ (B_1), where $B_1(0) = 1$. Upon charge readout, we only see if the defect is bright or dark, measuring $B(t) = B_0(t) + B_1(t)$ with $B(t) + D(t) = 1$. Using the condition $B_0(0) = 1$, the analytic form of the time dependence during the SCC process upon solving becomes:

$$B(t) = \frac{R_{sf} + R_I e^{-(R_{sf}+R_i)t}}{R_{sf} + R_I} \tag{6.22}$$

where the exponential term has a rate $R_{SCC} = R_{sf} + R_I$ We use Eq. 6.22 to model the effect of the balance of ionization rate and spin-flip rates on the final maximal SCC contrast $C = max(1 - B(t))$. In this case, this occurs when $t \to \infty$:

$$C(p_i) = \frac{R_I}{R_{sf} + R_I} = \frac{1}{1 + \frac{R_{sat}}{ap_i}} \tag{6.23}$$

Which we recognize as saturation behavior with dependence on the ionization laser power p_i, in which the relevant rate and timescale is set by the saturation spin flip rate R_{sat} and ap_i is the ionization rate when the defect is saturated by the resonant laser. In this case, near-unity contrast can be achieved simply by having sufficient ionization laser power. In this simplified model, which does not take into account dynamics in the readout or experimental imperfections, the contrast is the same as the SCC fidelity ($C = F$).

6.8.1 Including the effect of stimulated emission

In our experiment, we hypothesize that the reason that contrast does not approach unity even when the ionization laser power is increased is due to stimulated emission from the excited state induced by the 1151 nm ionization laser. This laser is too low in energy to be absorbed by the defect, but does overlap with the emission sideband. A sufficiently strong pump may stimulate the defect to emit at the ionization laser frequency. The result of this stimulated emission is a reduction in the effective excited state lifetime. This results in two changes to the relevant rates. First, the saturation behavior of the defect is modified. Powers that were previously sufficiently high enough to saturate the defect without stimulated emission may be too weak and will not saturate the defect when the lifetime is effectively shortened. We model this effect by a modification of $p_0 \rightarrow p_0 + \alpha p_i$, which represents a linear increase in the emission rate from the excited state. Second, the spin-flip rate at saturation will be modified due to the reduced excited state lifetime, which is linear in power $R_{sat} \rightarrow R_{sat} + \beta p_i$, where p_i is the ionization laser power. Combined, we have for the spin-flip rate:

$$R_{sf,stim}(p_{res}, p_i) = \frac{R_{sat} + \beta p_i}{1 + (p_0 + \alpha p_i)/p_{res}} \tag{6.24}$$

The second effect is a change of the ionization rate. This is purely due to the modification of the saturation behavior.

$$R_{I,stim}(p_{res}, p_i) = \frac{a p_i}{1 + (p_0 + \alpha p_i)/p_{res}} \tag{6.25}$$

We note that this unexpected saturation is shown in experiment in Fig. 5.4D. The rate equations are the same as described previously, just with the modified power dependence and interplay betweenp_i and p_{res}. The SCC contrast under the effect of stimulated emission has the same solution as before, with modified R_I and R_{sf}. Critically, the time constant on the exponential term is still $-(R_I + R_{sf})$ and the contrast at $t \rightarrow \infty$ is now:

$$C(p_i) = \frac{1}{1 + \frac{R_{sat}}{ap_i} + \frac{\beta}{a}} \tag{6.26}$$

The maximal contrast is still achieved where $p_i \to \infty$ but is non-unity:

$$C_{max} = \frac{1}{1 + \frac{\beta}{a}} \tag{6.27}$$

We see that the maximal contrast C_{max} is limited by the ratio of the stimulated emission-induced spin-flip increase from a lifetime reduction β to the ionization rate from the ionization laser a. We note that the maximal contrast does not depend on the effect of the saturation behavior modification (the factor α). Generally, from the form of $C(p_i)$, the contrast increases with p_i, but saturates to the non-unity value C_{max}. We use this function to fit Fig. 5.5D. We can also calculate the time evolution in the case where we excite both on the E_x and $E_{1,2}$ lines, constituting a spin-independent mechanism to access the excited state with our resonant lasers. In this case, the ionization is spin-agnostic and the rate equations:

$$\frac{dB}{dt} = -R_{I,stim}(p_{res}, p_i)B \tag{6.28}$$

$$\frac{dD}{dt} = +R_{I,stim}(p_{res}, p_i)B \tag{6.29}$$

and therefore, when prepared in the bright state ($B(0) = 1$):

$$B(t) = e^{-R_{I,stim}t} \tag{6.30}$$

6.8.2 Calculating the stimulated emission contribution

In experiment, we can measure the saturated spin flip rate R_{sat} (Fig. 6.1). We can also perform spin agnostic-ionization to measure the rate of decay $R_{I,stim}$. Finally, we can use the decay of the population in the spin dependent SCC experiment which has a rate

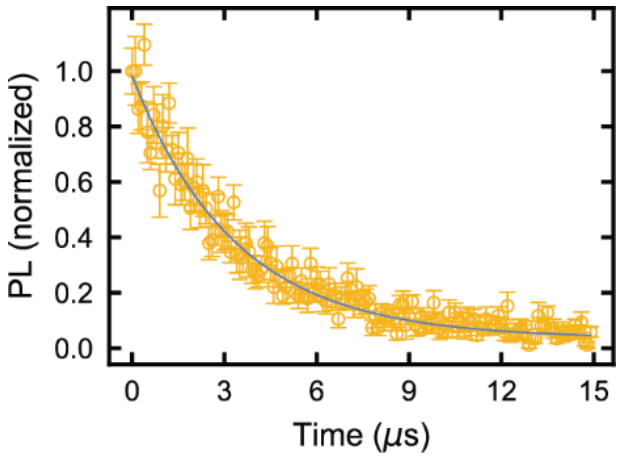

Figure 6.1: Spin flip lifetime. PL decay trace taken using time-tagging while only the E_x optical transition is excited after initializing to $m_S = 0$. We model the decay in the PL signal as $A * exp(-\frac{t}{\tau_{sf}}) + y_0$ (blue line fit), where A is the PL emission rate, y_0 is the laser scatter and background count rate, and τ_{sf} is the spin flip lifetime, which we calculate to be 3.3 $\pm$ 0.1 μs. The spin flip rate R_{sf} is $1/\tau_{sf}$. All data is taken at B=18 G and T=5 K. All reported errors represent 1 SD from the fit and all error bars represent 1 SD of the raw data.

$R_{sf,stim} + R_{I,stim}$. We note that the SCC curve has contributions from both the spin flip rate, the ionization rate, and a modification from the stimulated emission rate. Our goal is to elucidate the contribution solely from stimulated emission. Without considering the contribution from stimulated emission, we can take the results from our three experiments and calculate $R_{stim} = R_{SCC} - R_{spin-agn.} - R_{sat} = (R_I + R_{sf}) - R_I - R_{sat} = R_{sf} - R_{sat}$. In our experiment, we operate where the defect is saturated $p_{res} >> p_0$ and thus $R_{sf} \approx R_{sat}$. Therefore, we expect that in the absence of stimulated emission, $R_{SCC} - R_{spin-agn.} - R_{sat} = 0$. Anything non-zero in our experiment represents the effect of the modifications from stimulated emission. So, we have the expression for the "missing rate", R_{stim}:

$$R_{stim} = R_{sf,stim}(p_{res}, p_i) - R_{sat} \tag{6.31}$$

which we re-write:

$$R_{stim} = \frac{\beta p_i}{1 + (p_0 + \alpha p_i)/p_{res}} + (-1 + \frac{1}{1 + (p_0 + \alpha p_i)/p_{res}})R_{sat} \tag{6.32}$$

If once again we assume $p_{res} >> p_0 + \alpha p_i$, where the saturation reduction effect is minimized then we see:

$$R_{stim} = \beta p_i \tag{6.33}$$

which cancels all terms except the effect of stimulated emission. The assumption $p_{res} >> p_0 + \alpha p_i$ is validated by the non-saturating behavior in Fig. 5.5E, which plots this missing rate. Our calculation then allows us to extract β, the stimulated emission effect on the spin-flip rate per unit power. In experiment we measure ∼13 MHz/W (Fig. 5.5E). In practice, the actual stimulated emission rate is 2β, once again due to the 50% occupation of the excited state at saturation. We can also directly measure a, the spin agnostic ionization rate per unit power as the linear slope of Fig. 5.4D. In experiment, the behavior is slightly saturating, with a fitted value using the low power data for a of ∼35 MHz/W. Fig. 5.4D is fit well to the saturation behavior of $R_{I,stim}(p_{res}, p_i)$, further evidence of the role stimulated emission plays. From these two measurements, the resulting ratio $\frac{\beta}{a}$ is ∼0.37. We note that from our rate equation model, we therefore expect the maximal contrast/fidelity from this basic model to be approximately $C_{max} = \frac{1}{1+\frac{\beta}{a}}$ ∼72%, surprisingly consistent with our results given just the measurements of α, β. The matching of the power dependencies (unexpected saturation), the presence of this "missing rate" and the estimation of our contrast by just measuring two relevant rates establishes that stimulated emission plays a dominant role in the SCC process. From the fits of the data, we can further estimate $\frac{\alpha}{p_{res}}$ ∼9 at with $p_{res} \sim 14\mu W$. Similarly, we can confirm the ratio of $\frac{p_0}{p_{res}}$ which we measure to be ∼0.27 in experiment, consistent with the fit from our modeling which is ∼0.18.

6.9 Density functional theory (DFT) calculations

6.9.1 Theory and methods

Energetics

We computed the energy of the ionization threshold $E^{VBM}_{q+1/q}$ from VV^0 to VV^- using Kohn-Sham density functional theory (DFT):

$$E^{VBM}_{q+1/q} = E^{q}_{tot} - E^{q+1}_{tot} + \Delta V(q) - \Delta V(q+1) - \epsilon(VBM) \tag{6.34}$$

where q= -1 for VV^- and q+1=0 for VV^0 , E_{tot} is the total energy of the supercell containing the defect, ΔV is a correction term to the total energy as derived by Freysoldt et al. in the case of charged defects [85], and $\epsilon(VBM)$ is the position of valence band maximum (VBM) as determined by the highest occupied Kohn-Sham eigenvalue.

Cross sections

The cross section of the stimulated emission as a function of the photon energy $\hbar\omega$ and temperature T is given by [88]:

$$\sigma_{\mathrm{s}}(\hbar\omega, T) = \frac{4\pi^2\alpha}{n}\hbar\omega r_s^2 A_{\mathrm{s}}\left(\hbar\omega - E_{ZPL}, T\right) \tag{6.35}$$

Here α is the fine-structure constant, n is the refractive index, r_s^2 is the square of the optical matrix element for the transition ${}^3E$ to ${}^3A_2$ of VV^0 at a given photon polarization, and E_{ZPL} is the energy of the zero-phonon line (ZPL). $A_{\mathrm{s}}\left(\hbar\omega, T\right)$ is the electron-phonon spectral function for stimulated emission, which is the same as that of the spontaneous emission (photoluminescence) [87, 88]:

$$A_{\mathrm{s}}(\hbar\omega, T) = \sum_a \sum_b P_{e_a}(T) \left|\left\langle \Theta_{e_a} \mid \Theta_{g_b} \right\rangle\right|^2 \delta\left(\hbar\omega - E_{e_a} + E_{g_b}\right) \tag{6.36}$$

Here Θ_{e_a} (Θ_{g_b}) is the a^{th} (b^{th}) nuclear wave function of the system in the excited state ^{3}E (ground state $^3A_2$) with vibrational energy E_{e_a} (E_{g_b}), and $P_{e_a}(T)$ is the distribution function of the vibrational energies at finite temperature in the excited state. We compute the spectral function by using the displaced harmonic oscillator approximation and the generating function approach [87].

Similarly, the ionization cross section is given by:

$$\sigma_{\mathrm{i}}(\hbar\omega, T) = \frac{4\pi^2\alpha}{n}\hbar\omega \sum_j r_{i,j}^2 A_{\mathrm{i}}\left(\hbar\omega - E_{i,j}, T\right) \tag{6.37}$$

Here $r_{i,j}^2$ is the square of the optical matrix element between the initial state (^3E state of VV^0), and all possible final states (^2E state of VV^- with a hole in the valence band) for a given photon polarization direction. The summation over j includes all valence states of the defective system. $E_{i,j}$ is the energy difference between the initial and final states. $A_{\mathrm{i}}(\hbar\omega, T)$ is the electron-phonon spectral function for ionization, which can be computed in the same way as $A_{\mathrm{s}}(\hbar\omega, T)$. We computed the ionization cross section as a convolution [88]:

$$\sigma_{\mathrm{i}}(\hbar\omega, T) = \hbar\omega \int_{-\infty}^{\infty} \frac{1}{\hbar\omega'}\tilde{\sigma}_{\mathrm{i}}\left(\hbar\omega'\right) A_{\mathrm{i}}\left(\hbar\omega - \hbar\omega'\right) d\left(\hbar\omega'\right) \tag{6.38}$$

where

$$\tilde{\sigma}_{\mathrm{i}}(\hbar\omega) = \frac{4\pi^2\alpha}{n}\hbar\omega \sum_j r_{i,j}^2 \delta\left(\hbar\omega - E_{i,j}\right) \tag{6.39}$$

Here, we replace the δ function with a Gaussian function, since in our calculations we utilize a finite number of k-points to sample the supercell Brillouin zone.

Optical matrix elements

Optical matrix elements are key ingredients for the accurate description of both the stimulated-emission and ionization cross sections. Here we compute optical matrix elements assuming

that the wavefunctions of the single-particle orbitals of the defective crystal are the same irrespective of the orbital occupation. Hence, the optical matrix elements between two many-electron wavefunctions can be computed from the matrix elements between single particle orbitals [88]. For example, the optical matrix elements entering the stimulated emission cross section for the $m_s = 1$ sublevel of the ^3E and the $^3A_2$ state of VV^0 are given by:

$$\boldsymbol{r}_s = \left\langle {}^3E_{x/y}, m_s = 1 \left| \sum_e \boldsymbol{r}_e \right| {}^3A_2, m_s = 1 \right\rangle = \left\langle \bar{a}_1 \bar{e}_{x/y} \left| \sum_e \boldsymbol{r}_e \right| \bar{e}_{y/x} \bar{e}_{x/y} \right\rangle = \left\langle \bar{a}_1 | \boldsymbol{r} | \bar{e}_{y/x} \right\rangle \tag{6.40}$$

where we use the hole representation for many-electron wavefunctions. A similar expression is obtained for the $m_s = 0$ and $m_s = -1$ sublevels, where we assume that the spin-up and spin-down orbitals are identical.

The ionization optical matrix elements are calculated in a way similar to those of the stimulated emission. The optical matrix element from the $m_s = 1$ and $m_s = -1$ sublevels of the ^3E state of VV^0 into the $m_s = 1/2$ and $m_s = -1/2$ sublevels of the ^2E state of VV^- with a hole in the valence band are given by:

$$\begin{aligned} \boldsymbol{r}_{i,j} &= \left\langle {}^3E_{x/y}, m_s = 1 \left| \sum_e \boldsymbol{r}_e \right| \left({}^2E_{x/y}, m_s = \frac{1}{2} \right) + \bar{\phi}_j \right\rangle \\ &= \left\langle \bar{a}_1 \bar{e}_{x/y} \left| \sum_e \boldsymbol{r}_e \right| \bar{e}_{x/y} \bar{\phi}_j \right\rangle = \left\langle \bar{a}_1 | \boldsymbol{r} | \bar{\phi}_j \right\rangle \end{aligned} \tag{6.41}$$

$$\begin{aligned} \boldsymbol{r}_{i,j} &= \left\langle {}^3E_{x/y}, m_s = -1 \left| \sum_e \boldsymbol{r}_e \right| \left({}^2E_{x/y}, m_s = -\frac{1}{2} \right) + \phi_j \right\rangle \\ &= \left\langle a_1 e_{x/y} \left| \sum_e \boldsymbol{r}_e \right| e_{x/y} \phi_j \right\rangle = \left\langle a_1 | \boldsymbol{r} | \phi_j \right\rangle \end{aligned} \tag{6.42}$$

In an analogous fashion, the optical matrix element from the $m_s = 0$ sublevel of the ^3E state of VV^0 into the $m_s = 1/2$ and $m_s = -1/2$ sublevels of the ^2E state of VV^- with a hole in the valence band are given by:

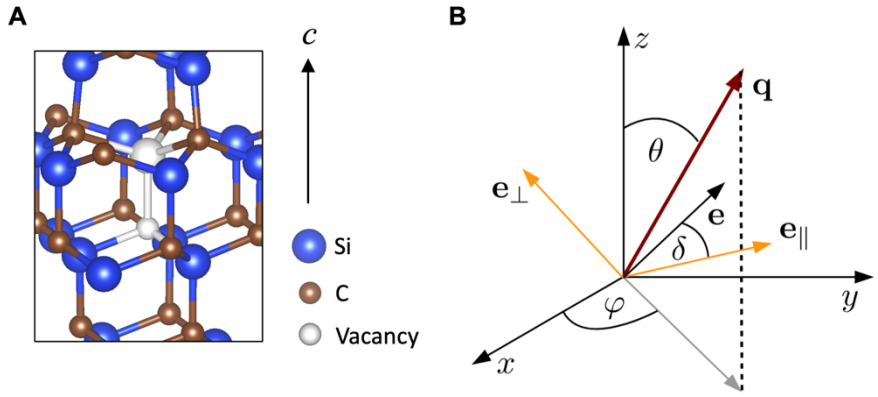

Figure 6.2: Schematic representation of the system. **(A)** Structure of the *hh* divacancy center in 4H-SiC. The 3-fold rotational axis of the divacancy center is parallel to the c -axis as shown in the plot. **(B)** Polarization for a photon with wavevector q, defined by the angles θ and ϕ in polar coordinates. The z-axis is chosen such that it aligns with the c-axis of 4H-SiC. $e_{\parallel}$ is the component of the photon polarization vector that lies in the x-y plane; $e_{\perp}$ is the out-of-plane component of the photon polarization; both $e_{\parallel}$ and $e_{\perp}$ are perpendicular to q. Any polarization direction e can be expressed as a linear combination of $e_{\perp}$ and $e_{\parallel}$.

$$\begin{aligned} \boldsymbol{r}_{i,j} &= \left\langle {}^3E_{x/y}, m_s = 0 \middle| \sum_e \boldsymbol{r}_e \middle| \left({}^2E_{x/y}, m_s = \frac{1}{2} \right) + \phi_j \right\rangle \\ &= \frac{1}{\sqrt{2}} \left\langle a_1 \bar{e}_{x/y} \middle| \sum_e \boldsymbol{r}_e \middle| \bar{e}_{x/y} \phi_j \right\rangle + \frac{1}{\sqrt{2}} \left\langle \bar{a}_1 e_{x/y} \middle| \sum_e \boldsymbol{r}_e \middle| \bar{e}_{x/y} \phi_j \right\rangle = \frac{1}{\sqrt{2}} \langle a_1 | \boldsymbol{r} | \phi_j \rangle \end{aligned} \tag{6.43}$$

$$\begin{aligned} \boldsymbol{r}_{i,j} &= \left\langle {}^3E_{x/y}, m_s = 0 \middle| \sum_e \boldsymbol{r}_e \middle| \left({}^2E_{x/y}, m_s = -\frac{1}{2} \right) + \bar{\phi}_j \right\rangle \\ &= \frac{1}{\sqrt{2}} \left\langle a_1 \bar{e}_{x/y} \middle| \sum_e \boldsymbol{r}_e \middle| e_{x/y} \bar{\phi}_j \right\rangle + \frac{1}{\sqrt{2}} \left\langle \bar{a}_1 e_{x/y} \middle| \sum_e \boldsymbol{r}_e \middle| e_{x/y} \bar{\phi}_j \right\rangle = \frac{1}{\sqrt{2}} \langle \bar{a}_1 | \boldsymbol{r} | \bar{\phi}_j \rangle \end{aligned} \tag{6.44}$$

Hence, the cross section is the same for all three sublevels of the ${}^3E$ state of VV^0.

To investigate the effect of photon polarization, we express the photon wavevector in polar coordinates (Fig. 6.2B) [90] with the z direction parallel to the c axis of 4H-SiC as:

$$\mathbf{q} = (\sin\theta\cos\varphi, \sin\theta\sin\varphi, \cos\theta) \tag{6.45}$$

and two polarization vectors in the x-y plane and the q-z plane as

$$\boldsymbol{e}_{\parallel} = (-\sin\varphi, \cos\varphi, 0) \tag{6.46}$$

$$\boldsymbol{e}_{\perp} = (-\cos\theta\cos\varphi, -\cos\theta\sin\varphi, \sin\theta) \tag{6.47}$$

As a result, any polarization vector can be expressed as a linear combination of $\boldsymbol{e}_{\parallel}$ and $\boldsymbol{e}_{\perp}$:

$$\mathbf{e} = \cos\delta\boldsymbol{e}_{\parallel} + \sin\delta\boldsymbol{e}_{\perp} \tag{6.48}$$

and the square of the optical matrix element r^2 becomes

$$r^2 = |e \cdot r|^2 = \left|\cos\delta\boldsymbol{e}_{\parallel} \cdot \boldsymbol{r} + \sin\delta\boldsymbol{e}_{\perp} \cdot \boldsymbol{r}\right|^2 \tag{6.49}$$

where the angle δ is defined in Fig. 6.2B.

6.9.2 Computational parameters

Energetics of the ionization of VV^0 to VV^-

We carried out DFT calculations with the Quantum Espresso code [83, 91, 92] and a dielectric dependent hybrid (DDH) functional [82], using a fraction of exact exchange equal to 0.15, corresponding to the inverse of the experimental dielectric constant of 4H-SiC in the direction parallel to the c-axis (see Fig.6.2A) [93]. We used supercells with 400 atoms (5*5*2) and sampled the supercell Brillouin zone with the Γ point. We employed SG15 ONCV pseudopotentials [84] and a plane-wave basis with a kinetic energy cut-off of 80 Ry. We used constrained occupations in DFT calculations to evaluate the excited states of the

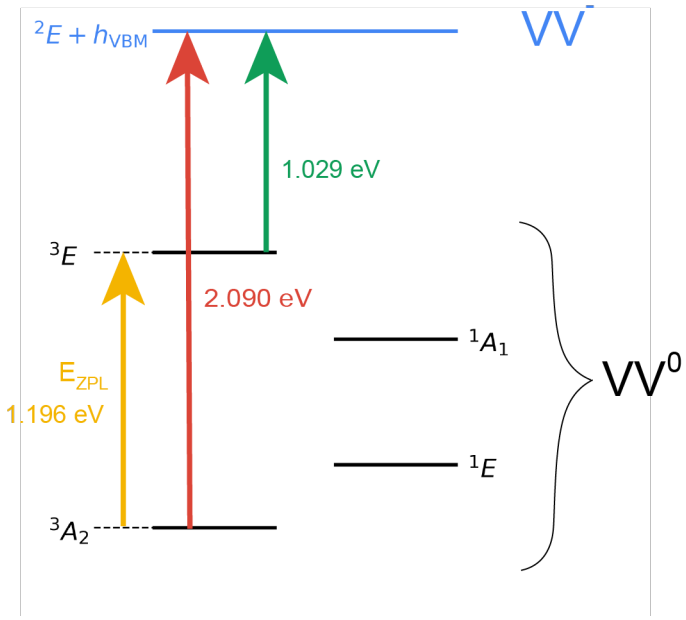

Figure 6.3: Schematic representation of the ionization of VV^0 to VV^-, where the energy of the transitions from many-body states (black lines) are indicated. $^3A_2$ and ^3E are the ground and excited triplet states of VV^0 respectively and ^2E corresponds to the ground state of VV^-; $^1A_1$ and ^1E, the singlet states of VV^0, are also indicated.

VV^0 defect and we computed the Freysoldt correction term (see Section 6.9.1) with the sxdefectalign package [85]. However, larger cell sizes are required to converge the computed values of the ZPL and here we report the values of the ZPL energy extrapolated to the values obtained with a 1024 atom-site supercell (8*8*2) [87].

Cross sections

We used the refractive index n=2.55 of 4H-SiC [94] in our calculation of ionization and stimulated-emission cross sections and in Fig. 6.4 we aligned the computed (1.196 eV) and the experimental (1.096 eV) ZPL energies for the stimulated cross section and the computed (1.029 eV) and the experimental (0.88 eV) onset for the ionization cross section.

We computed spectral functions (Eq. 6.36) using the generating function approach and the displaced harmonic oscillator approximation [87]. We used Gaussian functions with a standard deviation of 5 meV to broaden the δ function entering the expression of the spectral

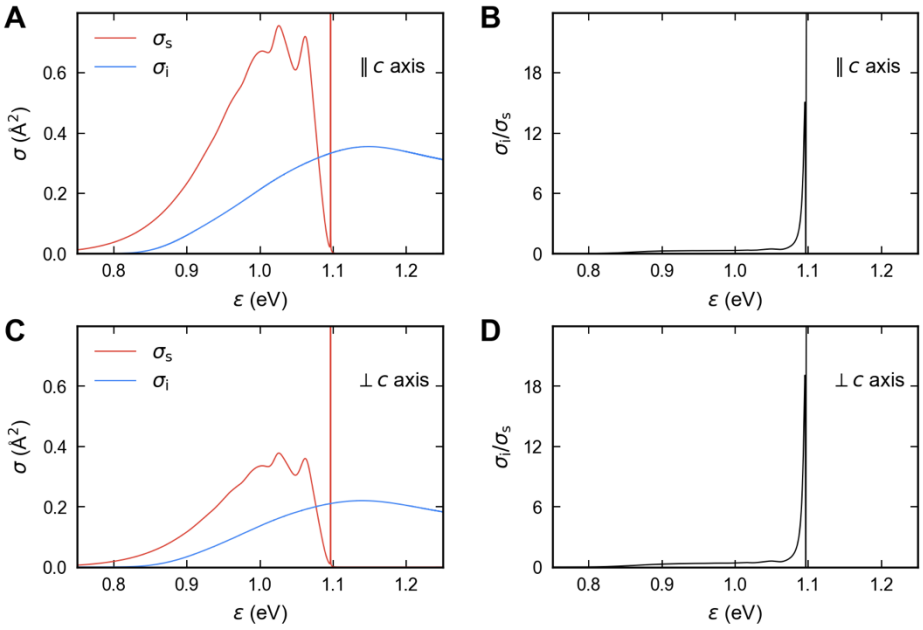

Figure 6.4: Computed stimulated emission (σ_s), ionization (σ_i) cross sections and their ratios. Computed cross sections with the light parallel **(A)** and perpendicular **(C)** to the c axis of 4H-SiC averaged over all possible polarization directions. Ratio of the stimulated emission and ionization cross sections with the light parallel **(B)** and perpendicular **(D)** to the c axis of 4H-SiC averaged over all possible polarization directions.

densities (Eqs. 11 and 12 of Ref. [87]). In the case of the stimulated emission, we broadened the ZPL with λ=0.002 meV (Eq. 8 of Ref. [87]), with the temperature set to 0 K in all calculations. We used Gaussian functions with a standard deviation of 30 meV to broaden the δ function entering Eq. 6.39 (ionization cross section).

We computed the phonon modes of defective solids using the frozen phonon approach and a (5*5*2) supercell, with configurations generated with the PHONOPY package [89] and a displacement of 0.01 Å from equilibrium positions. We extrapolated our results to the (16*16*5) supercell values, as proposed in Ref. [87]. The ground-state phonons of the hh-VV^0 defect (hh-VV$^-$) were used in the calculation of spectral functions of the stimulated emission (ionization). We used equal occupations of the e_x and the e_y orbitals in the phonon calculations for hh-VV$^-$ to maintain the C_{3v} symmetry of the point defect. Optical matrix elements We computed optical matrix elements between Kohn-Sham orbitals for hh-VV^0 in its ground state $^3A_2$ as

$$\langle\psi_a|\boldsymbol{r}|\psi_b\rangle = \frac{\left\langle\psi_a|[\hat{H},\boldsymbol{r}]|\psi_b\right\rangle}{\varepsilon_a - \varepsilon_b} \tag{6.50}$$

Here $\hat{H}$ is the Kohn-Sham Hamiltonian; ϵ_a (ϵ_b) is the energy of the Kohn-Sham orbital with single particle wavefunction ψ_a (ψ_b), and the contribution of the non-local potential to the commutator is explicitly taken into account. Calculations were performed with the WEST code [95] at the PBE level of theory [86]. We checked convergence as a function of the supercell size by carrying out calculations with a (5*5*2) supercell with 400 atomic sites up to a (9*9*2) supercell with 1296 atomic sites (see Fig. 6.6 for details).

6.9.3 Results

Polarization dependence

To determine the dependence of stimulated emission and ionization spectra on the light polarization, we considered the two limiting cases of light propagation along the z-axis,

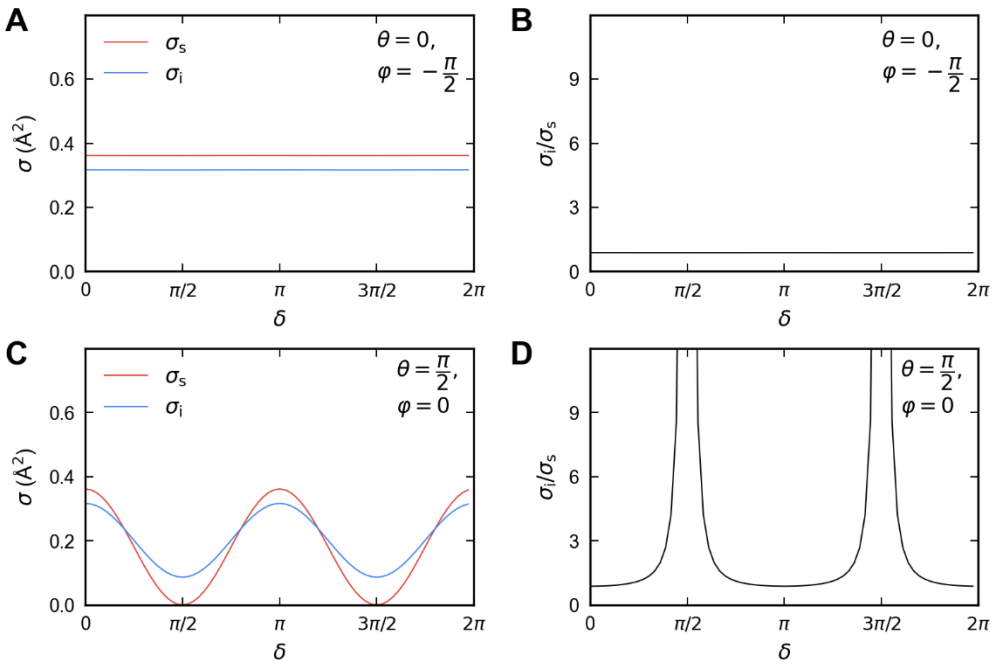

Figure 6.5: Computed stimulated emission (σ_s), ionization (σ_i) cross sections and their ratios at 1151 nm. **(A)** Computed cross sections at $\theta = 0$ and $\phi = \pi/2$ (light parallel to the z axis) **(C)** and at $\theta = \pi/2$ and $\phi = 0$ (light perpendicular to the x axis) as a function of the polarization angle δ. **(B)** Ratio of the stimulated emission cross sections and ionization cross sections at $\theta = 0$ and $\phi = -\pi/2$ (light parallel to the z axis) **(D)** and at $\theta = \pi/2$ and $\phi = 0$ (light perpendicular to the x axis) as a function of the polarization angle δ.

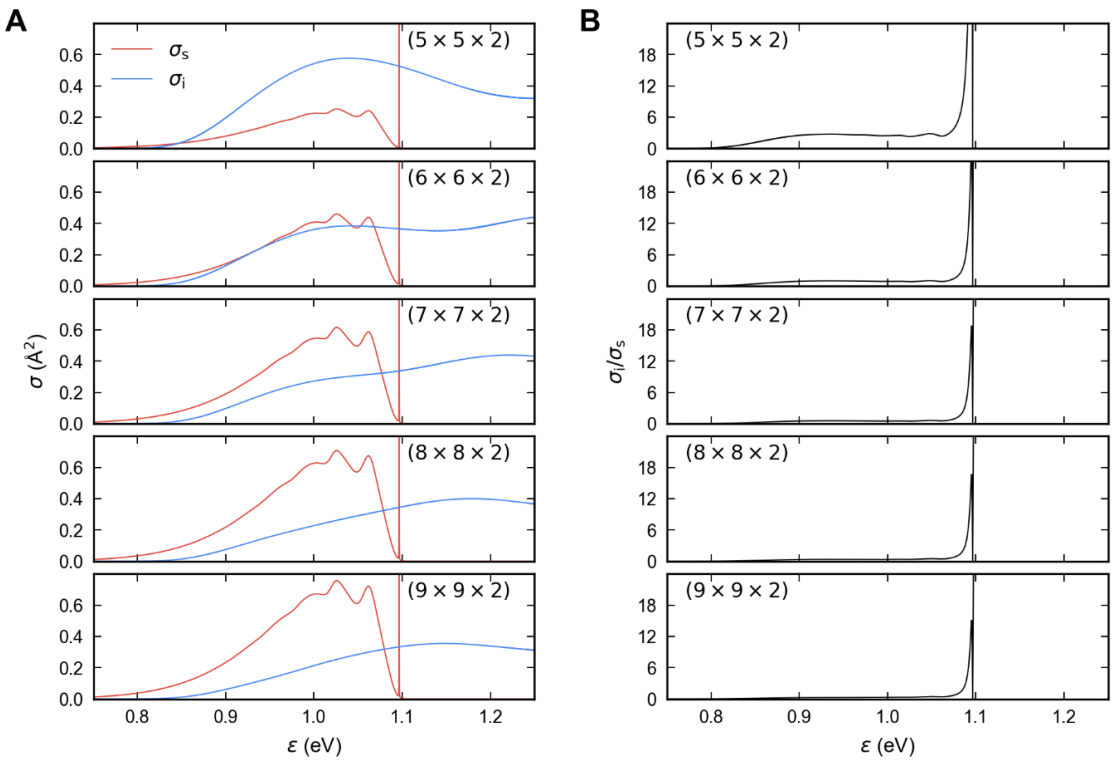

Figure 6.6: Computed stimulated emission (σ_s), ionization (σ_i) cross sections and their ratio as a function of the photon energy for supercells with different sizes. **(A)** Cross sections **(B)** and their ratio reach convergence for the (9*9*2) supercell.

parallel to the 3-fold rotational axis of the defect, which has C_{3v} symmetry, and that of propagation along the x-axis (Fig. 6.2B). In the case of propagation along the z-axis, we did not observe any polarization dependence of either the stimulated emission or the ionization cross sections (Fig. 6.5A), due to the symmetry of the defect orbitals in the x-y plane orthogonal to the defect 3-fold rotational axis. In the case of light propagation within the x-y plane, we observed instead a strong polarization dependence of the cross sections (Fig. 6.5C). For out-of-plane polarization parallel to the defect axis, the stimulated emission vanishes, and the cross-section ratio displays a pronounced pole.

Convergence of calculations

To investigate the finite-size effects on computed optical matrix elements and thus on the cross sections, we performed calculations using supercells with sizes increasing from (5*5*2)

to (9*9*2) (Fig. 6.6). We observed an increase of the stimulated emission cross section and a decrease of the ionization cross section as a function of supercell size and reached convergence for the (9*9*2) supercell.

6.9.4 Comparisons with experiment

We note that the calculated ionization cross sections for VV^0 are almost one order of magnitude greater than for the NV^- in diamond [88]. Our ionization wavelength in this work lies within the cross-section ratio peak corresponding to the scenario in Fig. 6.4B. Choosing an ionization laser closer to the ZPL would likely result in a higher ratio and a reduced effect of stimulated emission. In our experiments, no polarization dependence of the ionization laser is seen with light incident along the c-axis, as reproduced in Fig. 6.5A. Direct comparisons of the calculated and experimental ionization cross sections can be inferred from the reported rates of two-photon ionization and stimulated emission and assuming a 1 μm spot size. To calculate the cross-section, we use the relation $R = \frac{P\sigma}{A\hbar\omega}$ where R is the measured rate, P is the optical power, A is the optical spot size area, and $\hbar\omega$ is the energy of a single photon. However, our estimated cross-sections are almost one order of magnitude lower than the calculated values. This has many possible explanations. First, the defect's quantum efficiency (QE) is non-unity, where a reduction in radiative pathways reduces the measured stimulated emission rate and competes with photoionization processes. Second, the creation of VV^- plus a hole at the VBM doesn't always result in the defect being permanently ionized. Immediate hole recapture by the VV^-, reconverting to VV^0 may happen frequently, reducing the effective "ionization" rate. The defect only becomes dark if the hole becomes trapped at a different defect or recombines elsewhere.

Some of these factors are accounted for in the ratio of cross sections, which also eliminates actual laser power and spot size from our comparisons. We report a ratio $\alpha/\beta \sim 2.7$ which determines the SCC fidelity. In computation, we calculate that σ_i/σ_s is between 2.6 and 0.9 from 1140 nm to 1150 nm. As a result, the computation is very sensitive to small errors

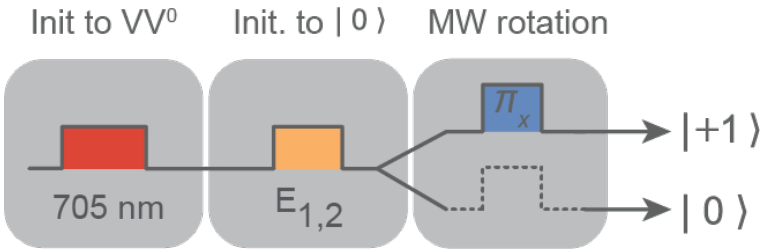

Figure 6.7: Protocol for preparation into different spin states. Both cases begin with preparation into VV^0 with the application of a 10 millisecond 705 nm charge reset pulse. Pumping of the $E_{1,2}$ lines initializes the spin to $m_s = 0$. Further manipulation with a microwave π pulse rotates the spin to initialize into $m_s = +1$. From there, other processes such as spin-dependent ionization via SCC, or charge readout can be performed.

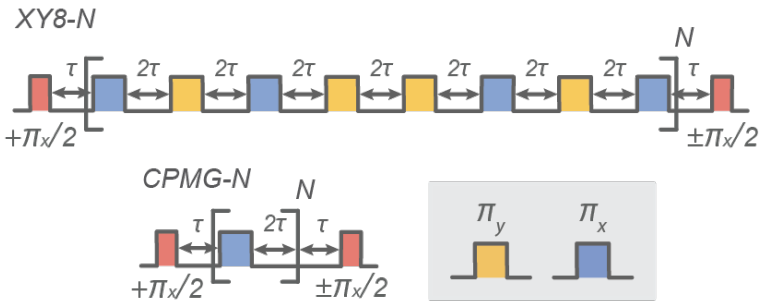

Figure 6.8: Dynamical decoupling sequences. XY8-N and CPMG-N sequences used for the coherence preservation demonstrated in the main text (Fig. 5.6). The final projective $\pi_x/2$ pulse employed in both sequences can have positive or negative phase to project onto $m_s = +1$ or $m_s = 0.$, respectively.

in terms of this ratio. A direct comparison between α/β and σ_i/σ_s is difficult, although they represent similar physics. While a directly relates to the photoionization cross section, it may not relate to the actual rate of ionization as mentioned above. On the other hand, β is the modification of the spin flip rate, which is proportional to the stimulated emission cross section, but is likely also dependent on the branching ratios and intrinsic lifetime of the excited state. This makes direct comparisons to Fig. 5.5E difficult as mentioned above. That being said, the metric σ_i/σ_s is directly proportional to α/β, meaning that from a computational perspective one can still optimize the performance of SCC by optimizing and understanding σ_i/σ_s. Further studies may be able to definitively link these two factors.

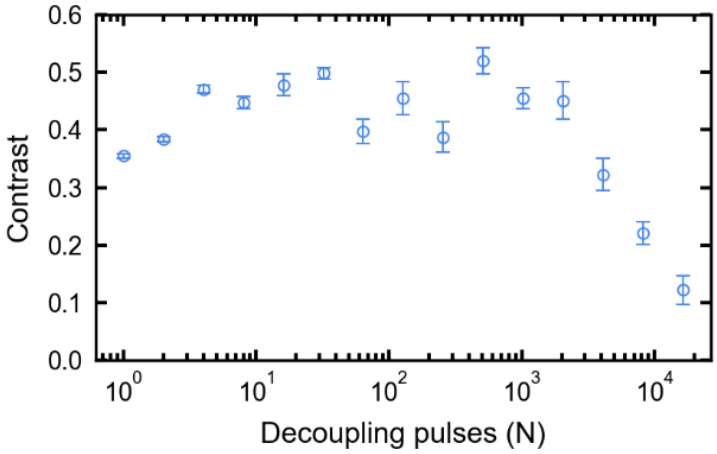

Figure 6.9: Maximum contrast with increasing pulse number. At high pulse number, the maximum contrast (at $\tau \sim 0$) deteriorates due to control infidelity. All error bars represent 1 SD of the raw data.

References

[1] Christopher P. Anderson, **Elena O. Glen**, Cyrus Zeledon, Alexandre Bourassa, Yu Jin, Yizhi Zhu, Christian Vorwerk, Alexander L. Crook, Hiroshi Abe, Jawad Ul-Hassan, Takeshi Ohshima, Nguyen T. Son, Giulia Galli, and David D. Awschalom. Five-second coherence of a single spin with single-shot readout in silicon carbide. *Science Advances*, 8, 2 2022.

[2] Joel Davidsson, Viktor Ivády, Rickard Armiento, N T Son, Ádám Gali, and Igor A Abrikosov. First principles predictions of magneto-optical data for semiconductor point defect identification: the case of divacancy defects in 4H–SiC. *New Journal of Physics*, 20:023035, 2 2018.

[3] M W Doherty, N B Manson, P Delaney, and L C L Hollenberg. The negatively charged nitrogen-vacancy centre in diamond: the electronic solution. *New Journal of Physics*, 13:025019, 2 2011.

[4] Elizabeth M. Y. Lee, Alvin Yu, Juan J. de Pablo, and Giulia Galli. Stability and molecular pathways to the formation of spin defects in silicon carbide. *Nature Communications*, 12:6325, 12 2021.

[5] Alexandre Bourassa. *Control of Spin Qubits in a Classical Electronics Material*. PhD thesis, University of Chicago Pritzker School of Molecular Engineering, 2021.

[6] J R Maze, Á Gali, E Togan, Y Chu, A Trifonov, E Kaxiras, and M D Lukin. Properties

of nitrogen-vacancy centers in diamond: the group theoretic approach. *New Journal of Physics*, 13:025025, 2 2011.

[7] M. L. Goldman, M. W. Doherty, A. Sipahigil, N. Y. Yao, S. D. Bennett, N. B. Manson, A. Kubanek, and M. D. Lukin. State-selective intersystem crossing in nitrogen-vacancy centers. *Physical Review B*, 91:165201, 4 2015.

[8] David J. Christle, Abram L. Falk, Paolo Andrich, Paul V. Klimov, Jawad Ul-Hassan, Nguyen T. Son, Erik Janzén, Takeshi Ohshima, and David D. Awschalom. Isolated electron spins in silicon carbide with millisecond coherence times. *Nature Materials*, 14:160–163, 2015.

[9] Lee C. Bassett, Audrius Alkauskas, Annemarie L. Exarhos, and Kai-Mei C. Fu. Quantum defects by design. *Nanophotonics*, 8(11):1867–1888, 2019.

[10] David J. Christle, Paul V. Klimov, Charles F. de las Casas, Krisztián Szász, Viktor Ivády, Valdas Jokubavicius, Jawad Ul-Hassan, Mikael Syväjärvi, William F. Koehl, Takeshi Ohshima, Nguyen T. Son, Erik Janzén, Ádám Gali, and David D. Awschalom. Isolated spin qubits in sic with a high-fidelity infrared spin-to-photon interface. *Physical Review X*, 7:1–12, 2017.

[11] Audrius Alkauskas, Bob B Buckley, David D Awschalom, and Chris G Van de Walle. First-principles theory of the luminescence lineshape for the triplet transition in diamond NV centres. *New Journal of Physics*, 16:073026, 7 2014.

[12] H. Bernien, B. Hensen, W. Pfaff, G. Koolstra, M. S. Blok, L. Robledo, T. H. Taminiau, M. Markham, D. J. Twitchen, L. Childress, and R. Hanson. Heralded entanglement between solid-state qubits separated by three metres. *Nature*, 497:86–90, 2013.

[13] Paul E. Barclay, Kai-Mei C. Fu, Charles Santori, Andrei Faraon, and Raymond G. Beausoleil. Hybrid nanocavity resonant enhancement of color center emission in diamond. *Phys. Rev. X*, 1:011007, 2011.

[14] Alexander L Crook, Christopher P Anderson, Kevin C Miao, Alexandre Bourassa, Hope Lee, Sam L Bayliss, David O Bracher, Xingyu Zhang, Hiroshi Abe, Takeshi Ohshima, Evelyn L Hu, and David D Awschalom. Purcell enhancement of a single silicon carbide color center with coherent spin control. *Nano Letters*, 20:3427–3434, 5 2020. doi: 10.1021/acs.nanolett.0c00339.

[15] Mouktik Raha, Songtao Chen, Christopher M Phenicie, Salim Ourari, Alan M Dibos, and Jeff D Thompson. Optical quantum nondemolition measurement of a single rare earth ion qubit. *Nature Communications*, 11:1605, 2020.

[16] William F. Koehl, Bob B. Buckley, F. Joseph Heremans, Greg Calusine, and David D. Awschalom. Room temperature coherent control of defect spin qubits in silicon carbide. *Nature*, 479:84–87, 11 2011.

[17] Christopher P Anderson, Alexandre Bourassa, Kevin C Miao, Gary Wolfowicz, Peter J Mintun, Alexander L Crook, Hiroshi Abe, Jawad Ul-Hassan, Nguyen T Son, Takeshi Ohshima, and David D Awschalom. Electrical and optical control of single spins integrated in scalable semiconductor devices. *Science*, 366:1225–1230, 2019.

[18] Kevin C Miao, Alexandre Bourassa, Christopher P Anderson, Samuel J Whiteley, Alexander L Crook, Sam L Bayliss, Gary Wolfowicz, Gergő Thiering, Péter Udvarhelyi, Viktor Ivády, Hiroshi Abe, Takeshi Ohshima, Ádám Gali, and David D Awschalom. Electrically driven optical interferometry with spins in silicon carbide. *Science Advances*, 5, 2019.

[19] Kevin C. Miao, Joseph P. Blanton, Christopher P. Anderson, Alexandre Bourassa, Alexander L. Crook, Gary Wolfowicz, Hiroshi Abe, Takeshi Ohshima, and David D. Awschalom. Universal coherence protection in a solid-state spin qubit. *Science*, 369:1493–1497, 2020.

[20] Abram L. Falk, Paul V. Klimov, Bob B. Buckley, Viktor Ivády, Igor A. Abrikosov, Greg

Calusine, William F. Koehl, Ádám Gali, and David D. Awschalom. Electrically and mechanically tunable electron spins in silicon carbide color centers. *Phys. Rev. Lett.*, 112:187601, 2014.

[21] P. V. Klimov, A. L. Falk, B. B. Buckley, and D. D. Awschalom. Electrically driven spin resonance in silicon carbide color centers. *Phys. Rev. Lett.*, 112:087601, 2014.

[22] Samuel J. Whiteley, Gary Wolfowicz, Christopher P. Anderson, Alexandre Bourassa, He Ma, Meng Ye, Gerwin Koolstra, Kevin J. Satzinger, Martin V. Holt, F. Joseph Heremans, Andrew N. Cleland, David I. Schuster, Giulia Galli, and David D. Awschalom. Spin–phonon interactions in silicon carbide addressed by gaussian acoustics. *Nature Physics*, 15:490–495, 2019.

[23] Alexandre Bourassa, Christopher P Anderson, Kevin C Miao, Mykyta Onizhuk, He Ma, Alexander L Crook, Hiroshi Abe, Jawad Ul-Hassan, Takeshi Ohshima, Nguyen T Son, Giulia Galli, and David D Awschalom. Entanglement and control of single nuclear spins in isotopically engineered silicon carbide. *Nature Materials*, 19:1319–1325, 2020.

[24] Hosung Seo, Abram L Falk, Paul V Klimov, Kevin C Miao, Giulia Galli, and David D Awschalom. Quantum decoherence dynamics of divacancy spins in silicon carbide. *Nature Communications*, 7:12935, 2016.

[25] J. R. Weber, W. F. Koehl, J. B. Varley, A. Janotti, B. B. Buckley, C. G. Van de Walle, and D. D. Awschalom. Quantum computing with defects. *Proceedings of the National Academy of Sciences*, 107(19):8513–8518, 2010.

[26] L. Gordon, A. Janotti, and C. G. Van De Walle. Defects as qubits in 3c- and 4h-sic. *Physical Review B - Condensed Matter and Materials Physics*, 92:1–5, 2015.

[27] Björn Magnusson, Nguyen Tien Son, András Csóré, Andreas Gällström, Takeshi Ohshima, Ádám Gali, and Ivan G Ivanov. Excitation properties of the divacancy in 4*h*-sic. *Phys. Rev. B*, 98:195202, 11 2018.

[28] L. Gordon, A. Janotti, and C. G. Van de Walle. Defects as qubits in 3C- and 4H-SiC. *Phys. Rev. B*, 92:045208, Jul 2015.

[29] G. D. Fuchs, V. V. Dobrovitski, D. M. Toyli, F. J. Heremans, and D. D. Awschalom. Gigahertz dynamics of a strongly driven single quantum spin. *Science*, 326:1520–1522, 12 2009.

[30] Susanne Richer and David DiVincenzo. Circuit design implementing longitudinal coupling: A scalable scheme for superconducting qubits. *Phys. Rev. B*, 93:134501, 2016.

[31] J. Gugler, T. Astner, A. Angerer, J. Schmiedmayer, J. Majer, and P. Mohn. Ab initio calculation of the spin lattice relaxation time T_1 for nitrogen-vacancy centers in diamond. *Phys. Rev. B*, 98:214442, Dec 2018.

[32] T. Astner, J. Gugler, A. Angerer, S. Wald, S. Putz, N. J. Mauser, M. Trupke, H. Sumiya, S. Onoda, J. Isoya, J. Schmiedmayer, P. Mohn, and J. Majer. Solid-state electron spin lifetime limited by phononic vacuum modes. *Nature Materials*, 17:313–317, 4 2018.

[33] A. Jarmola, V. M. Acosta, K. Jensen, S. Chemerisov, and D. Budker. Temperature- and magnetic-field-dependent longitudinal spin relaxation in nitrogen-vacancy ensembles in diamond. *Phys. Rev. Lett.*, 108:197601, 2012.

[34] Gopalakrishnan Balasubramanian, Philipp Neumann, Daniel Twitchen, Matthew Markham, Roman Kolesov, Norikazu Mizuochi, Junichi Isoya, Jocelyn Achard, Johannes Beck, Julia Tissler, Vincent Jacques, Philip R. Hemmer, Fedor Jelezko, and Jörg Wrachtrup. Ultralong spin coherence time in isotopically engineered diamond. *Nature Materials*, 8:383–387, 5 2009.

[35] Erik Bauch, Swati Singh, Junghyun Lee, Connor A. Hart, Jennifer M. Schloss, Matthew J. Turner, John F. Barry, Linh M. Pham, Nir Bar-Gill, Susanne F. Yelin, and Ronald L. Walsworth. Decoherence of ensembles of nitrogen-vacancy centers in diamond. *Phys. Rev. B*, 102:134210, 2020.

[36] M. Kim, H. J. Mamin, M. H. Sherwood, K. Ohno, D. D. Awschalom, and D. Rugar. Decoherence of near-surface nitrogen-vacancy centers due to electric field noise. *Phys. Rev. Lett.*, 115:087602, 2015.

[37] B. K. Ofori-Okai, S. Pezzagna, K. Chang, M. Loretz, R. Schirhagl, Y. Tao, B. A. Moores, K. Groot-Berning, J. Meijer, and C. L. Degen. Spin properties of very shallow nitrogen vacancy defects in diamond. *Phys. Rev. B*, 86:081406, 2012.

[38] J R Maze, A Dréau, V Waselowski, H Duarte, J-F Roch, and V Jacques. Free induction decay of single spins in diamond. *New Journal of Physics*, 14:103041, 10 2012.

[39] John Preskill. Lecture notes for Ph219/CS219: Quantum information, Chapter 3, 2018.

[40] Sean D. Barrett and Pieter Kok. Efficient high-fidelity quantum computation using matter qubits and linear optics. *Phys. Rev. A*, 71:060310, 2005.

[41] A.D. Córcoles, Easwar Magesan, Srikanth J. Srinivasan, Andrew W. Cross, M. Steffen, Jay M. Gambetta, and Jerry M. Chow. Demonstration of a quantum error detection code using a square lattice of four superconducting qubits. *Nature Communications*, 6:6979, 11 2015.

[42] Philipp Neumann, Johannes Beck, Matthias Steiner, Florian Rempp, Helmut Fedder, Philip R. Hemmer, Jörg Wrachtrup, and Fedor Jelezko. Single-shot readout of a single nuclear spin. *Science*, 329:542–544, 7 2010.

[43] G. Waldherr, Y. Wang, S. Zaiser, M. Jamali, T. Schulte-Herbrüggen, H. Abe, T. Ohshima, J. Isoya, J. F. Du, P. Neumann, and J. Wrachtrup. Quantum error correction in a solid-state hybrid spin register. *Nature*, 506:204–207, 2 2014.

[44] J. M. Elzerman, R. Hanson, L. H. Willems van Beveren, B. Witkamp, L. M. K. Vandersypen, and L. P. Kouwenhoven. Single-shot read-out of an individual electron spin in a quantum dot. *Nature*, 430:431–435, 7 2004.

[45] François Mallet, Florian R. Ong, Agustin Palacios-Laloy, François Nguyen, Patrice Bertet, Denis Vion, and Daniel Esteve. Single-shot qubit readout in circuit quantum electrodynamics. *Nature Physics*, 5:791–795, 11 2009.

[46] Shun Kanai, F. Joseph Heremans, Hosung Seo, Gary Wolfowicz, Christopher P. Anderson, Sean E. Sullivan, Giulia Galli, David D. Awschalom, and Hideo Ohno. Generalized scaling of spin qubit coherence in over 12,000 host materials. 2 2021.

[47] Gary Wolfowicz, F Joseph Heremans, Christopher P Anderson, Shun Kanai, Hosung Seo, Ádám Gali, Giulia Galli, and David D Awschalom. Quantum guidelines for solid-state spin defects. *Nature Reviews Materials*, 2021.

[48] Daniil M. Lukin, Constantin Dory, Melissa A. Guidry, Ki Youl Yang, Sattwik Deb Mishra, Rahul Trivedi, Marina Radulaski, Shuo Sun, Dries Vercruysse, Geun Ho Ahn, and Jelena Vu**c**ković. 4H-silicon-carbide-on-insulator for integrated quantum and nonlinear photonics. *Nature Photonics*, 14:330–334, 2020.

[49] S. J. Whiteley, F. J. Heremans, G. Wolfowicz, D. D. Awschalom, and M. V. Holt. Correlating dynamic strain and photoluminescence of solid-state defects with stroboscopic x-ray diffraction microscopy. *Nature Communications*, 10:5–10, 2019.

[50] Lucio Robledo, Lilian Childress, Hannes Bernien, Bas Hensen, Paul F.A. Alkemade, and Ronald Hanson. High-fidelity projective read-out of a solid-state spin quantum register. *Nature*, 477:574–578, 2011.

[51] Nguyen T. Son, Christopher P. Anderson, Alexandre Bourassa, Kevin C. Miao, Charles Babin, Matthias Widmann, Matthias Niethammer, Jawad Ul-Hassan, Naoya Morioka, Ivan G. Ivanov, Florian Kaiser, Joerg Wrachtrup, and David D. Awschalom. Developing silicon carbide for quantum spintronics. *Applied Physics Letters*, 116:190501, 2020.

[52] J. Cramer, N. Kalb, M. A. Rol, B. Hensen, M. S. Blok, M. Markham, D. J. Twitchen,

R. Hanson, and T. H. Taminiau. Repeated quantum error correction on a continuously encoded qubit by real-time feedback. *Nature Communications*, 7:1–7, 2016.

[53] Dominik M. Irber, Francesco Poggiali, Fei Kong, Michael Kieschnick, Tobias Lühmann, Damian Kwiatkowski, Jan Meijer, Jiangfeng Du, Fazhan Shi, and Friedemann Reinhard. Robust all-optical single-shot readout of nitrogen-vacancy centers in diamond. *Nature Communications*, 12, 2021.

[54] Qi Zhang, Yuhang Guo, Wentao Ji, Mengqi Wang, Jun Yin, Fei Kong, Yiheng Lin, Chunming Yin, Fazhan Shi, Ya Wang, and Jiangfeng Du. High-fidelity single-shot readout of single electron spin in diamond with spin-to-charge conversion. *Nature Communications*, 12:1–6, 2021.

[55] J. R. Maze, P. L. Stanwix, J. S. Hodges, S. Hong, J. M. Taylor, P. Cappellaro, L. Jiang, M. V.Gurudev Dutt, E. Togan, A. S. Zibrov, A. Yacoby, R. L. Walsworth, and M. D. Lukin. Nanoscale magnetic sensing with an individual electronic spin in diamond. *Nature*, 455:644–647, 2008.

[56] J. M. Taylor, P. Cappellaro, L. Childress, L. Jiang, D. Budker, P. R. Hemmer, A. Yacoby, R. Walsworth, and M. D. Lukin. High-sensitivity diamond magnetometer with nanoscale resolution. *Nature Physics*, 4:810–816, 2008.

[57] C. L. Degen, F. Reinhard, and P. Cappellaro. Quantum sensing. *Reviews of Modern Physics*, 89:1–39, 2017.

[58] Terry Gullion, David B Baker, and Mark S Conradi. New, compensated carr-purcell sequences. *Journal of Magnetic Resonance (1969)*, 89:479–484, 1990.

[59] H Y Carr and E M Purcell. Effects of diffusion on free precession in nuclear magnetic resonance experiments. *Phys. Rev.*, 94:630–638, 5 1954.

[60] Juha T. Muhonen, Juan P. Dehollain, Arne Laucht, Fay E. Hudson, Rachpon Kalra, Takeharu Sekiguchi, Kohei M. Itoh, David N. Jamieson, Jeffrey C. McCallum, Andrew S. Dzurak, and Andrea Morello. Storing quantum information for 30 seconds in a nanoelectronic device. *Nature Nanotechnology*, 9:986–991, 2014.

[61] Alexei M Tyryshkin, Shinichi Tojo, John J L Morton, Helge Riemann, Nikolai V Abrosimov, Peter Becker, Hans-Joachim Pohl, Thomas Schenkel, Michael L W Thewalt, Kohei M Itoh, and S A Lyon. Electron spin coherence exceeding seconds in high-purity silicon. *Nature Materials*, 11:143–147, 2012.

[62] M. H. Abobeih, J. Cramer, M. A. Bakker, N. Kalb, M. Markham, D. J. Twitchen, and T. H. Taminiau. One-second coherence for a single electron spin coupled to a multi-qubit nuclear-spin environment. *Nature Communications*, 9:1–8, 2018.

[63] N. Bar-Gill, L. M. Pham, A. Jarmola, D. Budker, and R. L. Walsworth. Solid-state electronic spin coherence time approaching one second. *Nature Communications*, 4, 2013.

[64] D. Simin, H. Kraus, A. Sperlich, T. Ohshima, G. V. Astakhov, and V. Dyakonov. Locking of electron spin coherence above 20 ms in natural silicon carbide. *Physical Review B*, 95:161201, 4 2017.

[65] N. T. Son, P. Carlsson, J. Ul Hassan, E. Janzén, T. Umeda, J. Isoya, Á. Gali, M. Bockstedte, N. Morishita, T. Ohshima, and H. Itoh. Divacancy in 4H-SiC. *Physical Review Letters*, 96:055501, 2 2006.

[66] Ph Tamarat, N. B. Manson, J. P. Harrison, R. L. McMurtrie, A. Nizovtsev, C. Santori, R. G. Beausoleil, P. Neumann, T. Gaebel, F. Jelezko, P. Hemmer, and J. Wrachtrup. Spin-flip and spin-conserving optical transitions of the nitrogen-vacancy centre in diamond. *New Journal of Physics*, 10, 2008.

[67] N. B. Manson, J. P. Harrison, and M. J. Sellars. Nitrogen-vacancy center in diamond: Model of the electronic structure and associated dynamics. *Physical Review B - Condensed Matter and Materials Physics*, 74:1–11, 2006.

[68] Gary Wolfowicz, Christopher P Anderson, Andrew L Yeats, Samuel J Whiteley, Jens Niklas, Oleg G Poluektov, F Joseph Heremans, and David D Awschalom. Optical charge state control of spin defects in 4H-SiC. *Nature Communications*, 8:1876, 2017.

[69] D. A. Golter and C. W. Lai. Optical switching of defect charge states in 4H-SiC. *Scientific Reports*, 7:1–5, 2017.

[70] Michel Bockstedte, Felix Schütz, Thomas Garratt, Viktor Ivády, and Ádám Gali. Ab initio description of highly correlated states in defects for realizing quantum bits. *npj Quantum Materials*, 3:31, 2018.

[71] David A Hopper, Henry J Shulevitz, and Lee C Bassett. Spin readout techniques of the nitrogen-vacancy center in diamond. *Micromachines*, 9, 2018.

[72] Lukas Razinkovas, Marek Maciaszek, Friedemann Reinhard, Marcus W. Doherty, and Audrius Alkauskas. Photoionization of negatively charged NV centers in diamond: theory and ab initio calculations. *http://arxiv.org/abs/2104.09144*, 2021.

[73] Michael J. Biercuk and Hendrik Bluhm. Phenomenological study of decoherence in solid-state spin qubits due to nuclear spin diffusion. *Physical Review B*, 83:235316, 6 2011.

[74] J. Medford, Ł. Cywiński, C. Barthel, C. M. Marcus, M. P. Hanson, and A. C. Gossard. Scaling of dynamical decoupling for spin qubits. *Physical Review Letters*, 108:086802, 2 2012.

[75] Gary Wolfowicz, Christopher P Anderson, Berk Diler, Oleg G Poluektov, F Joseph

Heremans, and David D Awschalom. Vanadium spin qubits as telecom quantum emitters in silicon carbide. *Science Advances*, 6:eaaz1192, 2020.

[76] Berk Diler, Samuel J Whiteley, Christopher P Anderson, Gary Wolfowicz, Marie E Wesson, Edward S Bielejec, F Joseph Heremans, and David D Awschalom. Coherent control and high-fidelity readout of chromium ions in commercial silicon carbide. *npj Quantum Information*, 6:11, 2020.

[77] Roland Nagy, Matthias Niethammer, Matthias Widmann, Yu-Chen Chen, Péter Udvarhelyi, Cristian Bonato, Jawad Ul-Hassan, Robin Karhu, Ivan G Ivanov, Nguyen Tien Son, Jeronimo R Maze, Takeshi Ohshima, Öney O Soykal, Ádám Gali, Sang-Yun Lee, Florian Kaiser, and Jörg Wrachtrup. High-fidelity spin and optical control of single silicon-vacancy centres in silicon carbide. *Nature Communications*, 10:1954, 2019.

[78] Jan Jeske, Desmond W M Lau, Xavier Vidal, Liam P McGuinness, Philipp Reineck, Brett C Johnson, Marcus W Doherty, Jeffrey C McCallum, Shinobu Onoda, Fedor Jelezko, Takeshi Ohshima, Thomas Volz, Jared H Cole, Brant C Gibson, and Andrew D Greentree. Stimulated emission from nitrogen-vacancy centres in diamond. *Nature Communications*, 8:14000, 2017.

[79] Gary Wolfowicz, Christopher P. Anderson, Samuel J. Whiteley, and David D. Awschalom. Heterodyne detection of radio-frequency electric fields using point defects in silicon carbide. *Applied Physics Letters*, 115, 2019.

[80] Denis R. Candido and Michael E. Flatté. Suppression of the optical linewidth and spin decoherence of a quantum spin center in a $p{-}n$ diode. *PRX Quantum*, 8 2020.

[81] Krishnendu Ghosh, He Ma, Mykyta Onizhuk, Vikram Gavini, and Giulia Galli. Spin–spin interactions in defects in solids from mixed all-electron and pseudopotential first-principles calculations. *npj Computational Materials*, 7:123, 2021.

[82] Jonathan H. Skone, Marco Govoni, and Giulia Galli. Self-consistent hybrid functional for condensed systems. *Physical Review B*, 89:195112, 5 2014.

[83] Paolo Giannozzi, Stefano Baroni, Nicola Bonini, Matteo Calandra, Roberto Car, Carlo Cavazzoni, Davide Ceresoli, Guido L Chiarotti, Matteo Cococcioni, Ismaila Dabo, Andrea Dal Corso, Stefano de Gironcoli, Stefano Fabris, Guido Fratesi, Ralph Gebauer, Uwe Gerstmann, Christos Gougoussis, Anton Kokalj, Michele Lazzeri, Layla Martin-Samos, Nicola Marzari, Francesco Mauri, Riccardo Mazzarello, Stefano Paolini, Alfredo Pasquarello, Lorenzo Paulatto, Carlo Sbraccia, Sandro Scandolo, Gabriele Sclauzero, Ari P Seitsonen, Alexander Smogunov, Paolo Umari, and Renata M Wentzcovitch. Quantum espresso: a modular and open-source software project for quantum simulations of materials. *Journal of Physics: Condensed Matter*, 21:395502, 9 2009.

[84] Martin Schlipf and François Gygi. Optimization algorithm for the generation of oncv pseudopotentials. *Computer Physics Communications*, 196:36–44, 2015.

[85] Christoph Freysoldt, Jörg Neugebauer, and Chris G. Van de Walle. Fully ¡i¿ab initio¡/i¿ finite-size corrections for charged-defect supercell calculations. *Physical Review Letters*, 102:016402, 1 2009.

[86] John P. Perdew, Kieron Burke, and Matthias Ernzerhof. Generalized gradient approximation made simple. *Physical Review Letters*, 77:3865–3868, 10 1996.

[87] Yu Jin, Marco Govoni, Gary Wolfowicz, Sean E. Sullivan, F. Joseph Heremans, David D. Awschalom, and Giulia Galli. Photoluminescence spectra of point defects in semiconductors: Validation of first-principles calculations. *Physical Review Materials*, 5:084603, 8 2021.

[88] Lukas Razinkovas, Marcus W Doherty, Neil B Manson, Chris G de Walle, and Audrius Alkauskas. Vibrational and vibronic structure of isolated point defects: The nitrogen-vacancy center in diamond. *Phys. Rev. B*, 104:45303, 7 2021.

[89] Atsushi Togo and Isao Tanaka. First principles phonon calculations in materials science. *Scripta Materialia*, 108:1–5, 2015.

[90] Hsiao-Yi Chen, Maurizia Palummo, Davide Sangalli, and Marco Bernardi. Theory and ab initio computation of the anisotropic light emission in monolayer transition metal dichalcogenides. *Nano letters*, 18:3839–3843, 6 2018.

[91] P Giannozzi, O Andreussi, T Brumme, O Bunau, M Buongiorno Nardelli, M Calandra, R Car, C Cavazzoni, D Ceresoli, M Cococcioni, N Colonna, I Carnimeo, A Dal Corso, S de Gironcoli, P Delugas, R A DiStasio, A Ferretti, A Floris, G Fratesi, G Fugallo, R Gebauer, U Gerstmann, F Giustino, T Gorni, J Jia, M Kawamura, H-Y Ko, A Kokalj, E Küçükbenli, M Lazzeri, M Marsili, N Marzari, F Mauri, N L Nguyen, H-V Nguyen, A Otero de-la Roza, L Paulatto, S Poncé, D Rocca, R Sabatini, B Santra, M Schlipf, A P Seitsonen, A Smogunov, I Timrov, T Thonhauser, P Umari, N Vast, X Wu, and S Baroni. Advanced capabilities for materials modelling with quantum espresso. *Journal of Physics: Condensed Matter*, 29:465901, 11 2017.

[92] Paolo Giannozzi, Oscar Baseggio, Pietro Bonfà, Davide Brunato, Roberto Car, Ivan Carnimeo, Carlo Cavazzoni, Stefano de Gironcoli, Pietro Delugas, Fabrizio Ferrari Ruffino, Andrea Ferretti, Nicola Marzari, Iurii Timrov, Andrea Urru, and Stefano Baroni. Quantum espresso toward the exascale. *The Journal of Chemical Physics*, 152:154105, 2020.

[93] Lyle Patrick and W J Choyke. Static dielectric constant of SiC. *Phys. Rev. B*, 2:2255–2256, 9 1970.

[94] Michael E Levinshtein, Sergey L Rumyantsev, and Michael S Shur. *Properties of Advanced Semiconductor Materials: GaN, AIN, InN, BN, SiC, SiGe*. John Wiley & Sons, 2001.

[95] Marco Govoni and Giulia Galli. Large scale gw calculations. *Journal of Chemical Theory and Computation*, 11:2680–2696, 2015. PMID: 26575564.